Resonantly Interacting Fermi Gases: Coherence, Collective Dynamics, and Polarons

Dissertation by

Christoph Kohstall

Submitted to
the Faculty of Mathematics, Computer
Science and Physics of the University of Innsbruck

In Partial Fulfillment of the Requirements
for the Degree of Doctor of Science

Advisor:
Univ.Prof. Dr. Rudolf Grimm,
Institute of Experimental Physics, University of Innsbruck,
Institute for Quantum Optics and Quantum Information
of the Austrian Academy of Sciences

Innsbruck, January 2012

SUMMARY

Some of the most intriguing phenomena in physics arise in strongly interacting many-body quantum systems. Those systems, however, e.g. solid state devices or astronomical objects, are hard to access experimentally and their theoretical understanding poses great challenges, as most theories are exact only in the regime of weak interactions. Now, ultracold gases serve as a highly controllable quantum system that allows to continuously explore all the range from weak to strong interactions by means of Feshbach resonances. Hence, ultracold gases are employed to test advanced many-body theories and to push our understanding of strongly interacting quantum matter. The present thesis is devoted to pursue this fundamental approach and discusses experiments on superfluidity in a homonuclear Fermi mixture and on the behavior of an impurity with a novel heteronuclear Fermi-Fermi mixture.

We study the rotational dynamics and coherence of a superfluid mixture of ^{6}Li atoms in two different Zeeman states. To prove superfluidity of the gas directly in the regime of strong interaction, we measure the moment of inertia of the gas. We find the moment of inertia to stay below the value of a rigid body, as a consequence of the irrotationality of the superfluid. A further property of a superfluid is the coherence among the particles, as a macroscopic fraction of the particles occupies the ground state. We probe this coherence by letting two independently created samples interfere. We observe interference for moderate repulsive interactions, where the Fermi mixture forms a Bose-Einstein condensate of weakly bound molecules. In the regime of strong interaction, however, the high scattering rate hinders the overlap of the two clouds and they collide hydrodynamically.

The heteronuclear Fermi-Fermi mixture is realized with ^{40}K and ^{6}Li atoms. First, we characterize the elastic and inelastic scattering properties at one of the interspecies Feshbach resonances. Then we demonstrate strong interactions by observing hydrodynamic expansion. The signatures are an inversion of the cloud aspect ratio and collective flow of ^{40}K and ^{6}Li atoms. In the regime of strong interactions, we investigate the behavior of few ^{40}K atoms in a Fermi sea of ^{6}Li atoms. Following Fermi liquid theory of L. Landau, impurity plus excitations are described as a quasiparticle, which is coined the "repulsive polaron" in our case. We show the existence of these repulsive many-body states in the regime of strong interaction by radio-frequency spectroscopy and measure their quasiparticle properties: interaction energy, residue, and lifetime. The remarkably long lifetime, at the specific Feshbach resonance we employ, may open up new possibilities to investigate novel quantum phases in strongly repulsively interacting Fermi gases.

ZUSAMMENFASSUNG

Vor einem Jahrhundert wurde die Theorie zur Bose-Einstein Kondensation aufgestellt und die Suprafluidität in Experimenten entdeckt. Einerseits die Theorie für Systeme mit vernachlässigbarer Wechselwirkung zwischen den Teilchen und andererseits das Experiment an einem System mit stark wechselwirkenden Teilchen wurden Jahrzehnte später miteinander in Verbindung gebracht. Eine makroskopisch besetzte Wellenfunktion wie von N. Bose und A. Einstein beschrieben ist die Grundlage für Suprafluidität, jedoch bleibt die theoretische Beschreibung stark wechselwirkender Systeme eine Herausforderung. Derzeit eröffnen ultrakalte Quantengase die Möglichkeit, den gesamten Bereich von schwach zu stark wechselwirkend im Experiment zu untersuchen, und tragen dadurch maßgeblich zum Verständnis der Vielteilchenphysik bei. Ein besonderes Interesse gilt dabei den fermionischen Quantengasen, da sie der gleichen Statistik wie z.B. Elektronen unterliegen, deren Vielteilchenverhalten eine der großen Herausforderungen an die Physik darstellt.

Die vorliegende Arbeit diskutiert Experimente an ultrakalten, fermionischen Quantengasen, wobei wir insbesondere die Einstellbarkeit der Wechselwirkung nutzen, um Verständnis für den stark wechselwirkenden Bereich ausgehend vom schwach wechselwirkenden Bereich zu erlangen.

Wir untersuchen die Suprafluidität und Kohärenz einer unpolarisierten Zweikomponentenmischung von ^{6}Li Atomen in zwei verschiedenen Zeemanzuständen. Anders als im Bereich schwacher Wechselwirkung, wo die Mischung ausschließlich in der superfluiden Phase hydrodynamisches Verhalten zeigt, verhält sich die Mischung im Bereich starker Wechselwirkung auch bei höheren Temperaturen in der normalen Phase, auf Grund der hohen Stoßrate, noch hydrodynamisch. Um nun direkt im Bereich starker Wechselwirkung zwischen dem klassischen Verhalten und der Superfluidität zu unterscheiden, nutzen wir die Eigenschaft, dass das Suprafluid nicht in Rotation versetzt werden kann, solange keine Singularitäten (Vortices) angeregt werden. Wir messen das Trägheitsmoment der Wolke und stellen fest, dass dieses bei sehr niedrigen Temperaturen in der Tat kleiner ist als das eines klassischen Gases. Eine Messung des Trägheitsmoments als Funktion der Temperatur erlaubt es uns, die kritische Temperatur für Suprafluidität zu messen. Eine weitere Eigenschaft eines Suprafluids ist, dass eine makroskopische Anzahl von Teilchen die Grundzustandswellenfunktion besetzt und damit zueinander kohärent ist. Dies zeigen wir eindrucksvoll durch die Interferenz zweier unabhängig erzeugter Suprafluide und realisieren damit erstmals Interferenz von molekularen Kondensaten.

Des Weiteren dringen wir erstmals auch mit einer heteronuklearen Fermi-Fermi Mischung

von ^{40}K und ^{6}Li Atomen in den Bereich starker Wechselwirkung vor. Wir zeigen dies durch die Beobachtung von Effekten hydrodynamischer Expansion in der normalen Phase. Das Mischen von Fermionen unterschiedlicher Masse bereichert das Studium fermionischer Mischungen um einen zusäzlichen Freiheitsgrad, was neuartige Tests von Vielteilchentheorien oder auch neue Quantenphasen ermöglichen wird. Wir untersuchen das Verhalten von wenigen ^{40}K Atomen in einem Fermisee von ^{6}Li Atomen. Erstmals gelingt es uns, in einem fermionischen Quantengas einen wohldefinierten Vielteilchenzustand bei stark repulsiver Wechselwirkung zu realisieren. ^{40}K Atome regen den ^{6}Li Fermisee derart an, dass sich ein Bereich geringerer ^{6}Li Dichte um das ^{40}K Atom ausbildet. Nach L. Landaus Theorie wird nun das System ^{40}K Atom plus Anregungen des Fermisees zu einem Quasiteilchen zusammengefasst, welches in unserem Fall "repulsives Polaron" genannt wird. Wir messen eine beachtliche Lebenszeit dieses repulsiven Polarons in der ^{40}K ^{6}Li Mischung, was Möglichkeiten eröffnet, neuartige Quantenphasen in stark repulsiv wechselwirkenden Fermi Gasen zu realisieren.

THANKS

What a feeling when you cross the finish line. You have cycled a marathon. You could achieve this, so you can achieve so much more. And you remember what it took to achieve this.
It feels great to write the present thesis. I want to thank all of those who helped me to achieve this.

It is a big task to organize such a race.
My supervisor Rudi Grimm provides all the basis for great scientific research. Thank you for creating this environment and for teaching me your expertise.

It is much more fun to race in a team, to push the others and, in turn, to be carried along by the others in the wind shadow.
I want to thank all my colleagues, in particular the Li-team and the $FeLiKx$-team, for all the great discussions. The interplay of getting explanations, challenging the own insights, and developing thoughts together—this is what got me into the flow of understanding physics.

They may pass you but still it is great to compete with the best cyclists.
I want to thank all those in the community who I met at conferences and at other occasions for inspiring and challenging the research presented in this thesis.

Who actually made you to get a bike and motivated you to keep on going?
I want to thank all those who gave me valuable feedback, which motivated me to keep on going in physics. Just to mention a few, my physics teacher at school Wolfgang Herkt, the jurors at the competition "Jugend forscht", and my spervisor in Boulder Carl Wieman.

There is no way to cycle a marathon without refreshments.
There was nothing better than recreation with my friends. Thanks for giving me the right perspective and balance between physics, sports, and other fun stuff.

Riding the bike,
or doing research,
my family and Stefanie are a part of it.

CONTENTS

CHAPTER 1

INTRODUCTION

1.1 From the classical to the quantum world simply by cooling

The present thesis reports on experimental studies of ultracold gases of fermionic atoms with tunable interparticle interactions. The investigation of such systems pushes the understanding of problems in modern quantum physics and gives benchmarks to sophisticated theoretical models. Such insights into quantum physics become possible because simply by cooling, the de Broglie wavelength of the particles increases and we pass from the classical into the quantum world; the behavior of the gas can no longer be described by classical physics but asks for the fundamental principles of quantum mechanics.

A classical gas at room temperature, like the air around you, is well described in terms of the following three concepts: the particles (I) are point-like, (II) are distinguishable, and (III) rarely collide, i.e. the mean free path is larger than the interparticle spacing. Solely by cooling the gas, all those concepts are turned upside down. At ultralow temperatures, (I) the particles are so slow that they can no longer be treated as being point-like, but they are described by wave packets with a characteristic de Broglie wavelength, satisfying the Heisenberg uncertainty principle. Such quantum particles can directly show wave phenomena like interference [Est30, Mil05]. (II) The preparation of a gas of identical atoms, i.e. of a certain isotope in a certain quantum state, yields a gas of indistinguishable particles and the quantum statistics become crucial. Bosons favor to gather in one motional quantum state. This can lead to the macroscopic occupation of the ground state, called Bose-Einstein condensation (BEC), as reported on in Refs. [And95, Dav95, Bra95]. Fermions experience the Pauli exclusion principle, filling the motional energy levels up to the Fermi energy, which results in a so-called Fermi sea [DeM99]. (III) Wave nature and quantum statistics also enter the collisional physics [Wei99]. The collision cross section can be tuned by interferences of the relative wavefunction in the interatomic potential, in particular by means of Feshbach resonances [Ino98], very much like the light enhancement inside an optical resonator. The enhancement of the cross section opens up the interesting regime of strong interactions where the mean free path is comparable to the interparticle spacing. In this regime, the dynamic behavior of the ultracold gas resembles that of a classical fluid [O'H02]. Turning the three concepts upside down, by passing from the classical to the quantum world, triggers the huge scientific interest in ultracold gases. The first two, the wave nature of particles and the quantum statistics, are two of the corner stones of quantum mechanics: Standard quantum theory can well describe the observed phenomena like matter wave interference [Cro09] and Bose-Einstein condensation [Ket96, Pet02]. A still rewarding challenge is the understanding of the third concept, the regime of strong interactions: Here, the theoretical models are highly involved and experimental benchmarks are needed [Blo08a, Gio08, Rad10, Che10]. We enter this regime of strong interactions with a highly controllable model system of an ultracold mixture of fermionic atoms. One general goal is to provide those benchmarks, thereby pushing forward the understanding of strongly interacting quantum matter, which is the basis of a variety of systems like neutron stars, high-temperature superconductors, or a quark-gluon plasma and this understanding may facilitate new technological applications.

Thesis overview

The intention of this first chapter is to guide the reader to the scientific work presented in the body of this thesis. In Sec. 1.2, we introduce the field and sketch how the research on ultracold Fermi gases gives rich contributions to various fields in physics. Then we lay out some aspects of the research presented in the present thesis. We introduce the experiments that are done with a homonuclear mixture of fermionic ^{6}Li atoms in Sec. 1.3 and the experiments that are performed on a heteronuclear ^{40}K ^{6}Li Fermi-Fermi mixture in Sec. 1.4. The goal is to communicate the basic ideas, thus we refer to the cited literature for rigorous treatments. Section 1.5 drafts ongoing and future research that builds on the results presented in this thesis. The main results can be viewed at a glance in Sec. 1.6 and are presented in Chaps. 2-7.

To come back to the three concepts from above, let us relate the most striking manifestations of those concepts to three respective chapters of the present thesis: (I) The interference of two molecular BECs directly shows the wave nature, see Chap. 4. (II) The quenched moment of inertia is a direct consequence of the macroscopically occupied wavefunction, see Chap. 3. (III) The Fermi polaron is a many-body state, an impurity particle strongly interacting with other particles of a medium, see Chap. 7.

1.2 Myriads of control parameters lead to myriads of research possibilities

1.2.1 Control parameters

Ultracold Fermi gases represent, for an experimental physicist, a quantum system with an unprecedented degree of control over many system parameters. The majority of experiments is carried out with a mixture of two components, denoted by the indices 1 and 2. The components can either be two different states of one atomic species or two different atomic species. Here we bypass the underlying technical complexity, which are discussed in detail in other works [Joc04, Wil09]. In essence, our control panel could look like as shown in Fig. 1.1.

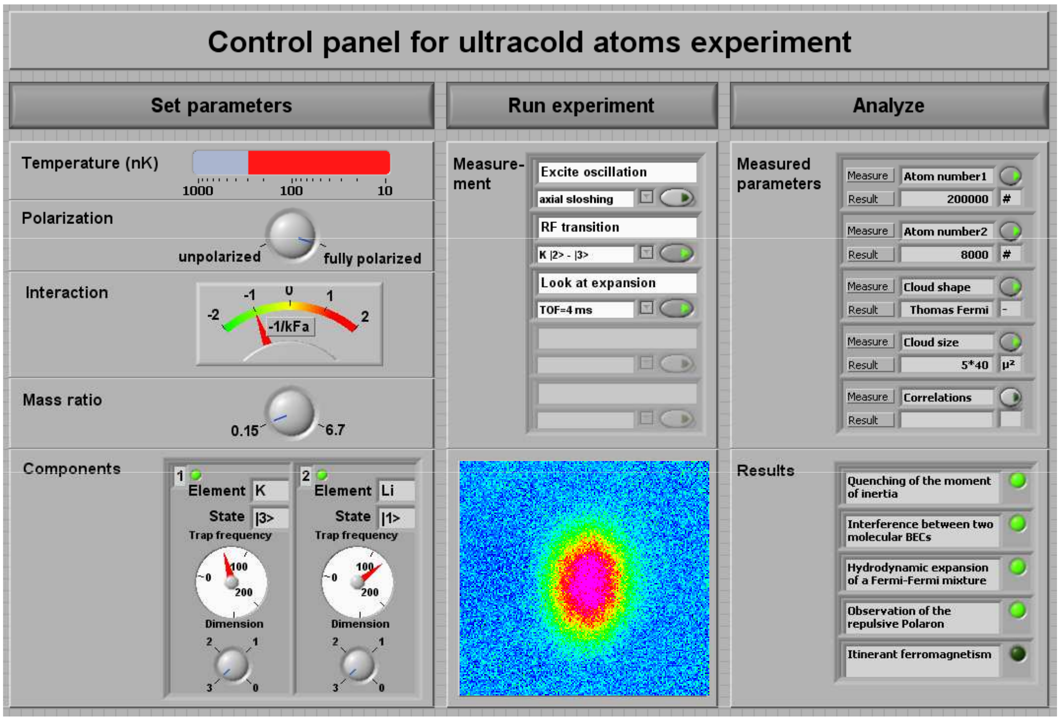

Figure 1.1: **Stylistic control panel for running an experiment with ultracold atoms.** The parameters of the gas, see text, are set (left column), a certain measurement type is performed and absorption images are taken (center column), the data are analyzed, and main results are derived (right column). The number of controllable parameters in all these steps directly reflect the many possibilities for research with ultracold atoms.

We have direct control to set various parameters of the two components such as

- T the temperature,
- $P = \frac{N_2 - N_1}{N_2 + N_1}$ the polarization, where N_i $(i = 1, 2)$ are the populations of the components,
- $1/(k_F a)$ parameterizing the interatomic interaction strength, as discussed later,
- m_1/m_2 the mass ratio, where m_i is the respective atomic mass,
- *component* the elements and the states of components 1 and 2,
- $\omega_{\mathrm{trap\,i}}$ the trap frequency parameterizing the confinement, and
- d_i the dimensionalities.

All those parameters can be varied from one experimental cycle to another, while turning one of the control dials implies to apply certain sequences and patterns of laser light or external magnetic field. This high degree of controllability makes it possible to map out and explore full phase diagrams and to study the transitions among various phases or states. Furthermore, we have exceptionally many measurement types for probing the gas, e.g. exciting collective oscillations, probing transitions between different Zeeman states with radio-frequency (rf), or letting the gas expand from the trap in time of flight (TOF). All measures are obtained from absorption images of each component. The atom numbers as well as information about the atom distribution in real space and momentum space can be deduced. The three steps together - setting parameters, probing, and analyzing - constitute one run of the experiment. One or a whole series of such runs are performed to obtain one of the data points presented in the figures of this thesis.

1.2.2 Research possibilities

The many possibilities to prepare, probe, and analyze ultracold Fermi gases allow the experimentalists to address many challenges of modern physics. In Fig. 1.2, we illustrate how different experimental methods (left column), carried out by different groups worldwide (center column), lead to observations that connect to deeper insights into different branches of physics (right column). Let us guide you through this figure on the basis of a few examples, the first rows of Fig. 1.2 (dash dotted lines): The cooling methods, as developed for bosonic atoms to reach BEC, were adapted to fermionic atoms to reach quantum degeneracy. At ultralow temperatures, the released energy and the momentum distribution of a degenerate Fermi gas, as measured in Ref. [DeM99], show a strong deviation from the classical gas behavior, unveiling the Fermi-Dirac distribution of the fermions over the trap states. Another corner stone for the progress of the field is the ability to tune the interactions between atoms by means of Feshbach resonances. Those resonances, where the scattering state resonantly couples to a bound state, were first studied in bosonic systems [Ino98]. While bosonic atoms suffer strong three-body relaxation close to the resonance, fermionic atoms turned out to be much more stable close to the center of the resonance [Pet04b]. Hence, Bose-Einstein condensation of weakly bound Feshbach molecules could be observed [Joc03b, Gre03, Zwi03a]. When tuning the interactions from repulsive across the resonance center to attractive interactions, the gas was still observed to show properties consistent with superfluidity [Reg04, Zwi04, Bar04b]. With this, ultracold fermions qualified to be a unique test bed for investigating the crossover from BEC to a Bardeen-Cooper-Schriefer (BCS) type superfluid, where the pairing mechanism in the limit of weak attractive interactions is not molecule formation but Cooper pairing [Bar57]. Resonantly interacting ultracold Fermi gases show an astonishingly high critical temperature relative to the Fermi temperature $T_c/T_F \approx 0.2$: This is why they are believed to hold the key for understanding high-T_c superconductivity and future experiments including lattices and/or higher partial wave scattering resonances may directly mimic the physics underlying high-T_c superconductivity [Che05b]. The list in Fig. 1.2 goes on with many more examples, but shows only a small selection of works. The intention is not to cover all and not even to cover the most important, but to show exemplarily how experimental techniques lead to new physical insights and to show how different works are interconnected and devoted to the same goal; see e.g. that the pairing between fermions was addressed by many different groups with different experimental techniques (dashed lines). The main intention, however, is to inspire readers independent of their background. Readers who are not in the field may see what a versatile tool ultracold

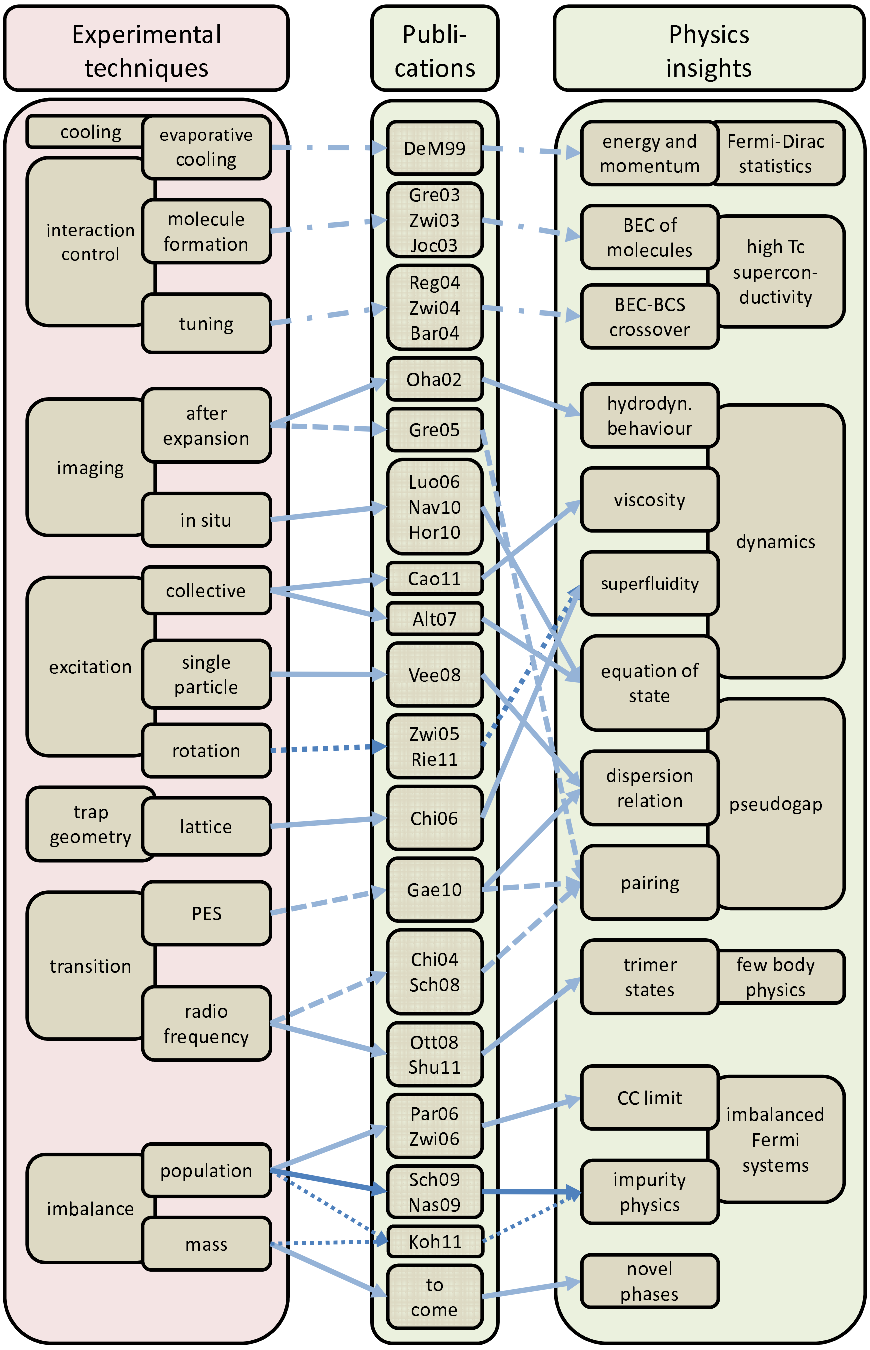

Figure 1.2: **Exploring physics with ultracold fermions.** The bubbles on the very left side are the central experimental techniques, which subdivide into more specific techniques. Those were applied by different groups in various publications. The publications address specific properties, which converge to insights into physics, the bubbles on the very right. In the text we refer to the different line styles. Listed publications are the Refs. [DeM99, Gre03, Zwi03a, Joc03b, Reg04, Zwi04, Bar04b, O'H02, Gre05, Luo07, Nav10, Hor10, Cao11, Alt07a, Vee08, Zwi05a, Rie11, Chi06, Gae10, Chi04, Sch08, Ott08, Nak11, Par06, Zwi06b, Sch09b, Nas09a, Koh11]. We use abbreviations for photo emission spectroscopy (PES) and for Chandrasekhar Clogston (CC), where the CC limit gives an upper limit to the polarization of the gas beyond that superfluidity is suppressed.

Fermi gases are. Note the divergence of different experimental techniques to many publications and the subsequent convergence to central physical problems. Readers who are in the field are invited to arrange their own work in this network and to find crosslinks and also to add experimental methods which may then lead to new discoveries. To give an example, Fig. 1.2 contains two of our publications (dotted lines). In Ref. [Rie11] (Chap. 3), we excite a rotation of the gas and from the irrotationality of the gas we can infer superfluid behavior. In Ref. [Koh11] (Chap. 7), we investigate the behavior of few ^{40}K atoms in a cloud of ^{6}Li atoms and find a new many-body state based on repulsive interactions.

The two latter examples bring us from the wide overview of the research on ultracold Fermi gases to our contributions. The measurement on the irrotationality was performed with an unpolarized spin mixture of ^{6}Li; as the polarization is 0 and the mass ratio is one, we refer to it in the following as *balanced*. The measurements on this balanced mixture are introduced in Sec. 1.3. The measurement on the impurity problem is one of the investigations performed in a Fermi-Fermi mixture of ^{6}Li and ^{40}K, where the spin mixture is polarized and the mass ratio is unequal to one, as introduced in Sec. 1.4.

1.3 Experiments on a balanced Fermi mixture

In this section we introduce the system employed for the experiments described in Chap. 2-4 and some earlier publications, see Chap. 8. The system is an unpolarized Fermi mixture of two different Zeeman states of ^{6}Li. For such a balanced mixture, we now introduce step by step the phase diagram as a function of temperature and of interaction strength. The diagram gives a comprehensive frame, within which we then arrange and introduce our contributions to the exploration of this quantum many-body system.

Let us classify the various properties of the mixture in three ways: whether it shows *collisionless* or *hydrodynamic* behavior, whether the components are *unpaired* or *paired*, and whether the gas is in a *normal* or *superfluid* phase. These properties are connected, as illustrated schematically in Fig. 1.3(a). A superfluid implies pairing because its basis is a condensate of bosonic pairs, composed of fermionic atoms. It also implies hydrodynamic behavior because the dynamics of a superfluid obey the irrotational hydrodynamic equations. In the normal phase, i.e. non-superfluid phase, pairs can form and high collision rates can lead to collisional hydrodynamics. The boundary between normal and superfluid phase is a sharp phase transition. Within the normal phase, the transitions paired-unpaired and collisionless-hydrodynamics are smooth crossovers.

Now, we map the schematic classification from Fig. 1.3(a) onto the actual phase diagram spanned by the axes interaction parameter and temperature, shown in Fig. 1.3(b), see Refs. [Gio08, Ing08b] for details. First, let us consider one species of identical fermionic atoms in a certain Zeeman state at ultralow temperatures. The atoms are noninteracting because s-wave scattering is prohibited by the wavefunction symmetry and, because of the centrifugal barrier, higher partial waves are frozen out at such low temperatures. The atoms fill up the lowest energy states up to the Fermi energy $E_F = \hbar^2 k_F^2/(2m_{\mathrm{Li}})$, where k_F is the Fermi momentum and $\hbar$ is the Planck constant h divided by 2π. Then, we add atoms of the same species but in a different Zeeman state. The atoms in different Zeeman states now

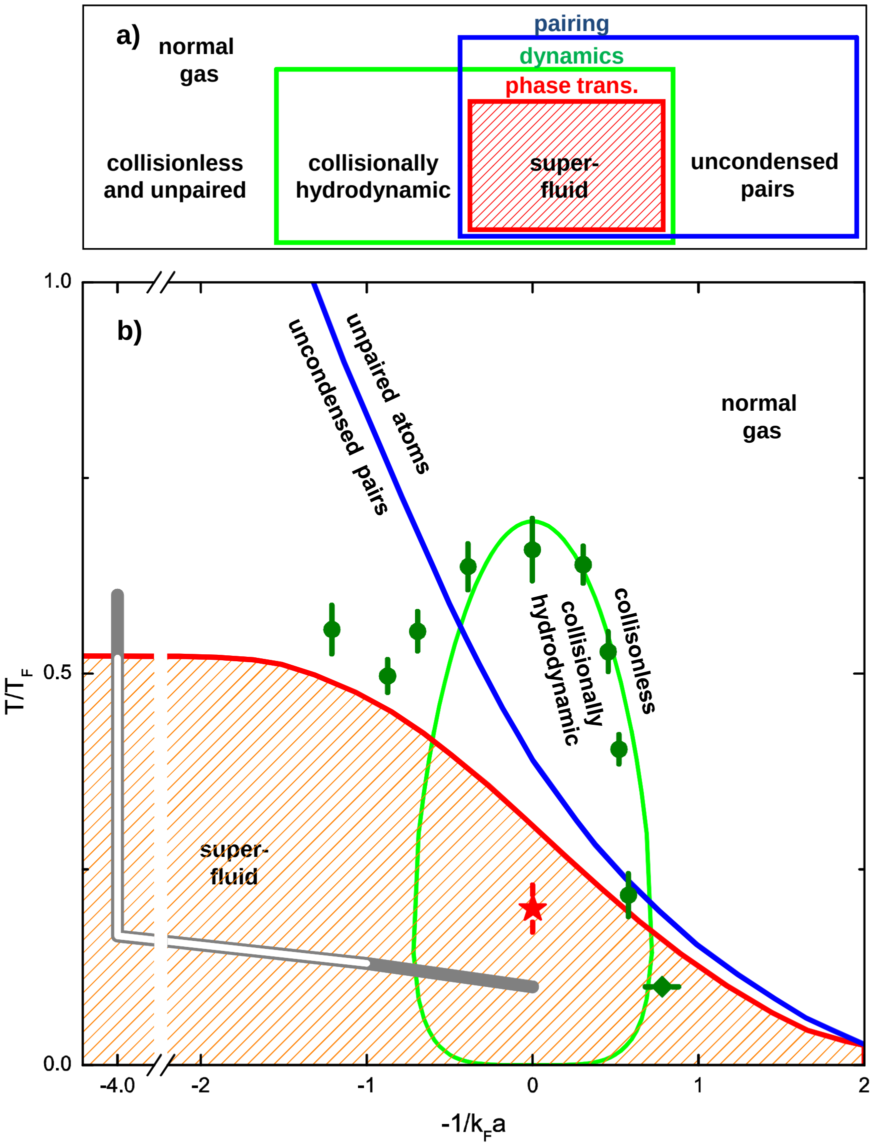

Figure 1.3: **Properties and phases of an unpolarized Fermi gas.** (a) The gas can be in a normal phase (white area) or in a superfluid phase (red shaded area). The superfluid phase implies pairing and hydrodynamics. The normal phase can contain pairs and can also show hydrodynamic behavior. (b) The same properties and phases are mapped onto a phase diagram versus the interaction parameter $1/(k_F a)$ and the temperature T/T_F for the case of a harmonic trap. The curves for T_c (▬), separating the normal and the superfluid phase, and T^* (▬), marking the crossover from unpaired to paired, are reproduced from Ref. [Per04]. From a simple calculation, see text, we derive a constant collision rate (▬), marking the crossover from collisionless to hydrodynamic behavior, which has no meaning in the superfluid phase. The respective value of the collision rate is chosen such that the line coincides with the measurements of the maximum damping of the scissors mode oscillation (●) [Wri07] and of the quadrupole oscillation (♦) [Alt07b]. The critical temperature on resonance is derived from the measurement of the quenching of the moment of inertia (★), see Chap. 3. The measured T_c is below the theoretical prediction presented here [Per04] but is in good agreement with more recent calculations [Gio08, Hau08]. Interference was probed along the grey line and nonvanishing fringe contrast was observed along the white-marked part of the grey line, see Chap. 4.

interact via s-wave scattering. The interaction is parameterized by the scattering length a, which can be tuned by means of a Feshbach resonance. The interaction strength is parameterized by the interaction parameter $-1/(k_F a)$. At $-1/(k_F a) = 0$, a molecular state opens up below threshold and for $-1/(k_F a) \ll -1$ the binding energy of this molecular state gives a characteristic temperature for molecule formation. In the many-body system, pairing persists throughout the resonance and the characteristic temperature for pairing is T^* [Per04], marked by the blue line in Fig. 1.3(b). The molecules are bosonic and, for weak repulsive interactions, they form a BEC below a critical temperature T_c, marked by the red line in Fig. 1.3(b). Also for weak attractive interaction, $-1/(k_F a) \gg 1$, the superfluid consists of pairs, but in this case the building blocks are Cooper pairs which form at the same temperature as they condense, i.e. $T_c = T^*$. The connection of these two types of a superfluid phase throughout the resonance is called the BEC-BCS crossover. The phase diagram is now divided into the superfluid and the normal phase. The paired sector comprises the superfluid part and extends to much higher temperatures for decreasing $-1/(k_F a)$. To get a qualitative intuition on the dynamic behavior of the gas, we also plot a line of constant scattering rate, green line in Fig. 1.3(b), derived from a semiclassical model. Therefor, we simply take the scattering rate to be proportional to the average relative velocity and the unitarity limited cross section [Gio08]. The gas is collisionally hydrodynamic in the center of the diagram, enclosed by the green lines in Fig. 1.3(b). Finally, we have mapped the possible properties of the quantum gas from Fig. 1.3(a) onto the phase diagram in Fig. 1.3(b).

The understanding of the phase diagram result from the synergetic work of many experimental and theoretical groups worldwide. Some works are mentioned in Sec. 1.2.2 and review articles provide further references [Ket08, Ing08b, Rad10, Che10]. For us, the phase diagram provides an appropriate frame to mark where the research presented in this thesis contributes to the experimental investigation of the properties and phases of the balanced mixture [Gri08].

Collective oscillation modes are sensitive to the dynamics of the gas. For example, the radial quadrupole mode (see Fig. 1.8) or the scissors mode (oscillation of the tilting angle of an elliptic cloud in an elliptic trap) have different eigenfrequencies in the collisionless and in the hydrodynamic cases and are strongly damped in the transition region [Dal99]. The study of the radial quadrupole mode as a function of the interaction strength at the lowest attainable temperature reveals the transition from hydrodynamic to collisionless behavior [Alt07b], see diamond in Fig. 1.3(b). The study of the scissors mode as a function of the temperature for different values of the interaction strength fully maps out the hydrodynamic regime [Wri07], see solid circles in Fig. 1.3(b). The general trend agrees well with our simple model. A further study of those two modes plus the compression mode at the center of the Feshbach resonance as a function of temperature investigates the dynamics in more detail. The data are compared to theoretical calculations of the collisional behavior [Rie08]. The calculations take into account Fermi blocking and pairing effects. Fermi blocking reduces the scattering rate towards lower temperatures whereas pairing increases it because the bosonic character of the pairs counteracts such Fermi blocking. It turns out that the two effects combined lead to a scattering rate close to the semiclassical one, explaining why the simple model used for the green line in Fig. 1.3(b) is in good agreement with the data.

The collective modes mentioned above probe whether the gas is hydrodynamic but do not distinguish between collisional and irrotational hydrodynamics. This distinction is needed to discriminate the normal phase from the superfluid phase in the strongly interacting regime. To prove superfluidity, one possibility is to detect irrotationality. Unlike a normal gas, which can accept an arbitrary number of angular momentum quanta, a superfluid can take angular momentum only in discrete steps, one angular momentum quantum times the number of particles. This leads either to the formation of vortices or to a reduced moment of inertia, the so-called quenching of the moment of inertia. Before addressing the proof of superfluidity, we investigate the rotation dynamics and damping of the rotation in the strongly interacting regime, see Chap. 2. The observed long lifetime of the angular momentum on resonance underlines the deeply hydrodynamic behavior even in the normal phase. In a subsequent, more detailed study of the process of setting the gas into rotation, we find that the angular momentum saturates below the rigid body value for low temperatures, see Chap. 3. This results from the quenching of the moment of inertia through the superfluid fraction and allows us to determine T_c on resonance, see the star in Fig. 1.3(b).

The quenching of the moment of inertia is a manifestation of the continuous phase of the macroscopic condensate wavefunction. This phase cannot be observed directly but the relative one with respect to a reference object is detectable. We observe this relative phase in the interference between two molecular Bose-Einstein condensates, see Chap. 4. Therefore we prepare two condensates at moderate positive scattering length and let them overlap. For increasing scattering length the interference pattern vanishes because elastic collisions during the overlap remove particles from the condensate wavefunction and those particles do no more contribute to the overall interference pattern. This study is also performed as a function of temperature. The parameter range where we search for an interference pattern is marked in grey and the white line on top marks where we indeed observe interference, see Fig. 1.3(b).

1.4 Experiments on a polarized mixture of Fermions with unequal masses

The extensive investigations on the balanced (homonuclear and unpolarized) Fermi mixtures deepen our understanding of Fermi systems in general. Only a few years ago, a new chapter was opened: The study of polarized Fermi gases [Zwi06b, Par06], which corresponds to turning the spin population control dial on the control panel in Fig. 1.1. Remarkable results are the observation of the Chandrasekhar-Clogston limit [Zwi06b] and, in the highly polarized case, the Fermi polaron [Sch09b]. At about the same time, the possibility to turn the dial controlling the mass ratio was considered. However, to an experimentalist, this still implies to build an entirely new apparatus designed to control two different elements. The natural choice is to combine the two, easily controlable, fermionic alkali isotopes ^{40}K and ^{6}Li, with the mass ratio $m_{\mathrm{K}}/m_{\mathrm{Li}} = 40/6$. Meanwhile, five groups [Tag08, Tie10, Rid11, Wu11, Spi10a] have control over such a ^{40}K ^{6}Li mixture.

The first experiments on the ^{40}K ^{6}Li Fermi-Fermi mixture were primarily devoted to investigate the collisional properties. Feshbach spectroscopy was performed [Wil08], molecule formation was demonstrated [Voi09], the stability of a three-spin mixture was shown [Spi09], cross dimensional relaxation was studied [Cos10], and interspecies thermalization was investigated [Tie10], just to mention a few achievements. For a short summary on the early experiments with this Fermi-Fermi mixture see Ref. [Tre11a].

We start the investigation of the ^{40}K ^{6}Li mixture with a careful characterization of the interspecies collisional properties, see Chap. 5. According to theoretical calculations, which are well approved by experimental results, all interspecies Feshbach resonances are (I) not very broad, (II) have a considerable closed channel contribution and (III) two- and three-body loss mechanisms are not negligible, see Ref. [Chi10] for detailed explanations on those characteristics of Feshbach resonances. Our goal is to investigate strongly correlated many-body physics in a ^{40}K ^{6}Li mixture. Therefor, we need to tune the interactions up to the strongly interacting regime. To achieve this the three properties, mentioned above imply (I) that we need precise control over the magnetic field, (II) that the interaction is dependent on the specific interatomic potential (it is not universal) and (III) that the lifetime of the sample is rather short. Considering all these issues, the Feshbach resonance between ^{40}K in its third-to-lowest Zeeman state with ^{6}Li in its lowest Zeeman state at a magnetic field of about 155 G appears to be the most promising candidate for investigations in the strongly interacting regime. A precise experimental characterization of the elastic and inelastic scattering properties at these resonances is presented in Chap. 5. Close to the center of this resonance we observe the effects of collisional hydrodynamics on the expansion of the ^{40}K ^{6}Li mixture, demonstrating that the regime of strong interactions can be accessed experimentally, see Chap. 6. We thus have a Fermi-Fermi mixture with tunable interaction up to the strongly interacting regime. This opens the door to a variety of possibilities to investigate strongly correlated many-body physics and few-body physics [Liu03, Isk07, Nis10, Lev09, Nis08]. We start with studying ^{40}K impurities in a ^{6}Li Fermi sea. Such a system can be well described by means of quasiparticles coined Fermi polarons, of which the underlying concepts are introduced in the following. The characterization of a novel quasiparticle, the *repulsive* Fermi polaron, is the main achievement of this thesis, see Chap. 7.

1.4.1 Introducing the concept of a quasiparticle

The impurity problem of few ^{40}K atoms in a ^{6}Li Fermi sea is well described by Fermi liquid theory, as introduced by L. Landau [Lan57]. Let us review the introduction of the quasiparticle (QP), the building block of a Fermi liquid, given in Ref. [Lan80]: "Any weakly excited state of a macroscopic body may be regarded, in quantum mechanics, as an assembly of separate *elementary excitations*. These behave like *quasiparticles* moving in the volume occupied by the body and possessing definite energies E_{QP} and momenta p_{QP}. The form of the function $E_{\mathrm{QP}}(p_{\mathrm{QP}})$, the *dispersion relation* for the elementary excitations arises as a means of quantum-mechanical description of the collective motion of the atoms in a body, and the quasiparticles cannot be identified with the individual atoms and molecules."

Because of the fundamental role in various systems, e.g. liquid ^{3}He or electrons in dielectric materials, the quasiparticle deserves to be explained from scratch. Let us consider the collective behavior of only *two* individual particles, elaborated in Fig. 1.4. This toy quasiparticle highlights three basic concepts: (I) The dispersion relation changes. (II) The QP cannot be identified with one individual particle. (III) QPs like phonons or polarons imply a

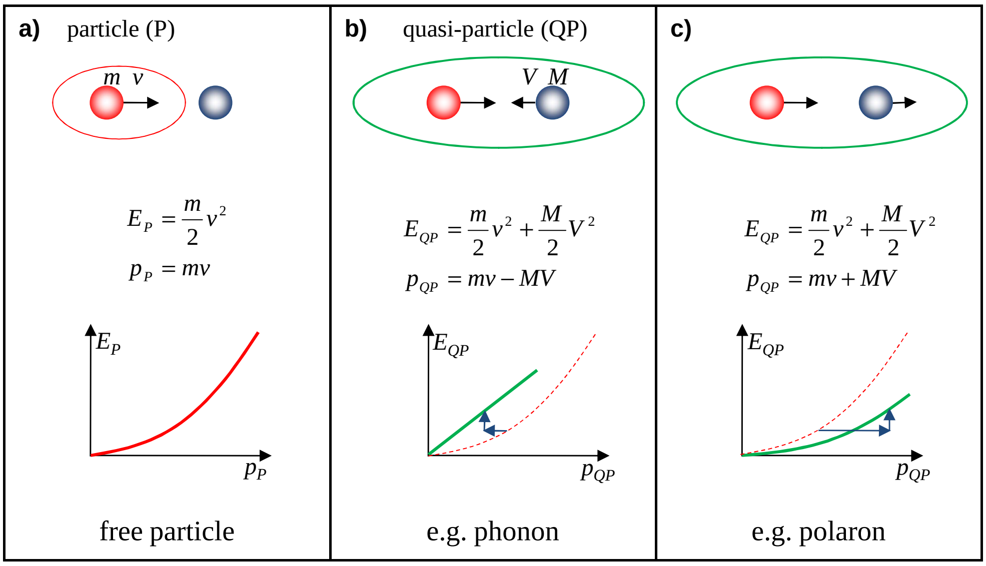

Figure 1.4: **Toy quasiparticle constructed from only two particles.** (a) A particle of mass m and velocity v has the standard free particle dispersion relation $E_p = p_p^2/(2m)$, which describes the elementary excitations in a noninteracting system. (b,c) In the interacting case, excitations are the collective motion of more particles in the medium. This collective excitation is treated as a quasiparticle. The toy quasiparticle here comprises only one additional particle with mass M and velocity V. (b) Given that the additional particle moves in opposite direction, the total energy of both particles, which constitute the quasiparticle, rises while the total momentum decreases. This simple argument explains for example the steep rise (but not yet the linearity) of the dispersion relation of phonons, as the motion in opposite direction is typical for such waves. (c) Considering a motion in the same direction, energy and momentum rise such that the dispersion relation flattens. In case the dispersion is still quadratic, the quasiparticle is described as a free particle but with an effective mass. This scenario should serve us as a rudimentary picture of a polaron, where a particle moves with its dressing cloud.

collective motion of particles. In general, a QP is characterized by its interaction energy, its effective mass, its QP residue, and its lifetime. The effective mass becomes already clear in our toy model in Fig. 1.4(c), the interaction energy and the residue are discussed in the following. For a more complete treatment of QPs we refer to Ref. [Mat92] and to the standard literature [Lan80].

1.4.2 Simple model for the energy of an impurity in a Fermi sea

Here, we discuss a simple model to comprehend the trend of the interaction energy of an impurity in a Fermi sea throughout the Feshbach resonance, following Ref. [Pri04]. Say we have an impurity atom (red in Fig. 1.5(a)) fixed at the center and let it interact with one atom of the Fermi sea (blue). The Pauli blocking of the Fermi sea is modeled by restricting

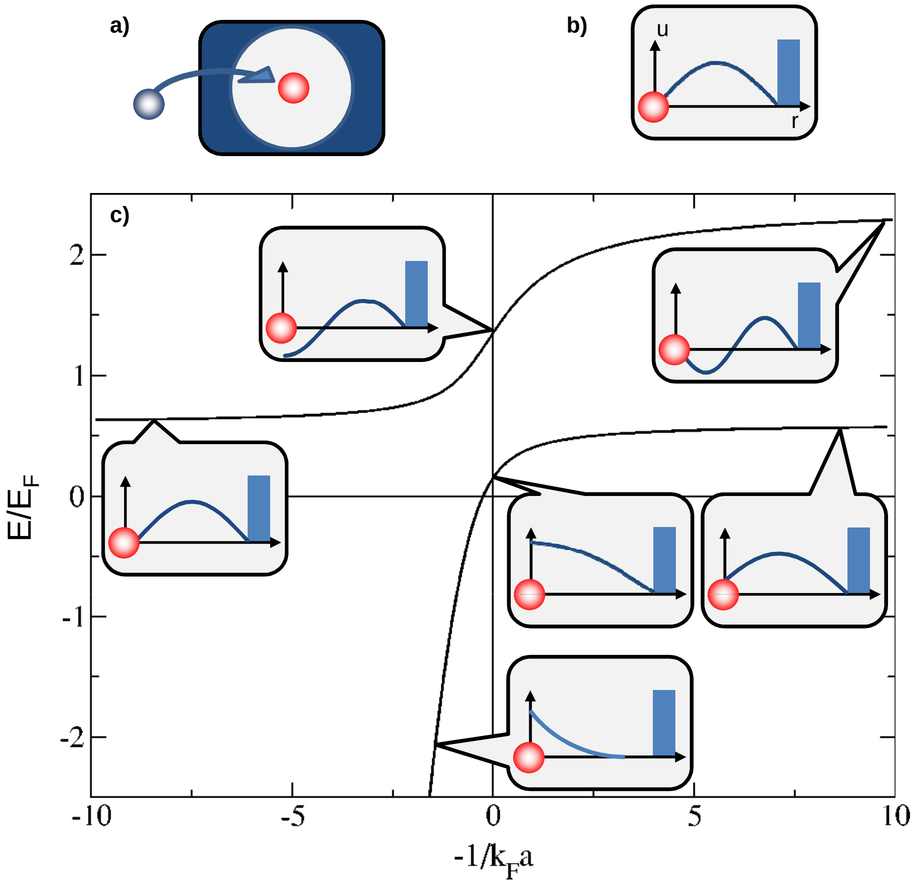

Figure 1.5: **Model for a strongly interacting Fermi gas.** (a) We consider the interaction of an impurity (red) with only one fermion (blue) of the Fermi sea. The Pauli exclusion principle is modeled as leaving only a sphere of space, with a hard wall around it. (b) The radial wavefunction $u(r) = \Phi(r) \cdot r$ is plotted for no interactions present. (c) The curves are calculations of the interaction energy relative to the Fermi energy versus interaction parameter, reproduced from Ref. [Pri04]. The exponentially decaying wavefunction represents the bound state.

the available space for this atom to a sphere with hard walls. The size of this sphere is chosen such that the ground state energy of the atom equals the mean energy per particle in the Fermi sea. One simplification in this model is that the impurity is fixed, which corresponds to taking an infinitely heavy impurity, however, a mass different from infinity is taken into account by taking the reduced mass for the atom out of the Fermi sea. Another simplification is that the impurity interacts with only one atom. In Fig. 1.5(b), we plot the radial part of the wavefunction of the atom for no interactions present. The wavefunction satisfies the boundary condition to be zero at the edge of the sphere. In Fig. 1.5(c) we sketch the behavior of the wavefunction for different values of the scattering length to illustrate the evolution of the weakly interacting states throughout the Feshbach resonance. For weak interactions, the energy corresponds to the well-known mean field result $E = gn_{\mathrm{Li}}$, where n_{Li} is the density of the Li Fermi sea and the interaction parameter g is proportional to the scattering length a. The interatomic interaction shifts the zero crossing of the wavefunction by a. The interaction energy E can be inferred from the change in kinetic energy. For positive (negative) a the curvature of the wavefunction is increased (decreased), leading to a positive (negative) E. For larger a, the shift of the wavefunction must be derived from the scattering phase shift ϕ. The exact calculation for any value of the interaction strength is given in Ref. [Pri04] and the result is displayed in Fig. 1.5(c). One important result is that the states do not connect on resonance, but the repulsive state evolves to an excited state and the attractive state connects to the bound state. Both states coexist in the regime of strong interaction with the distinction being one node in the wavefunction. The simple model already captures all the essential states: repulsive state and attractive state connected to the molecular state. A more quantitative treatment must take into account the interactions with all the Fermi sea and not only one majority atom.

1.4.3 Many-body approach to obtain the polaron properties

Above, we have introduced two basic concepts of the polaron. First, that the collective behavior of particles is conveniently described in terms of quasiparticles with specific properties. Second, we have derived the interaction energy of the system impurity in a Fermi sea throughout a Feshbach resonance, where the impurity interacts with only one majority atom being subject to the Pauli exclusion principle. Now, for a quantitative treatment of the impurity problem, those two concepts are combined by the ansatz as employed in Ref. [Che06]. The ansatz is solved for different mass ratios [Mas11], including the case of a ^{40}K impurity in a ^{6}Li Fermi sea, and we extend it to account for finite range effects in the two-body interaction, see Chap. 7. Note that this approach uses two different wavefunctions to either treat the unbound impurity or to describe the molecule. This is in contrast to the simple model in the previous section, where the weakly attractive state directly connects to the molecular state. The interaction energies of the unbound impurity and of the molecule versus the interaction parameter are plotted in Fig. 1.6(a). The exact values are specific for the mass ratio of the ^{40}K ^{6}Li system, our experimental parameters and the employed Feshbach resonance. The attractive polaron branch (green line) and the molecule branch (dashed line) were experimentally investigated before in the homonuclear case with ^{6}Li [Sch09b]. The main result of the present thesis is the characterization of the repulsive polaron, the energy

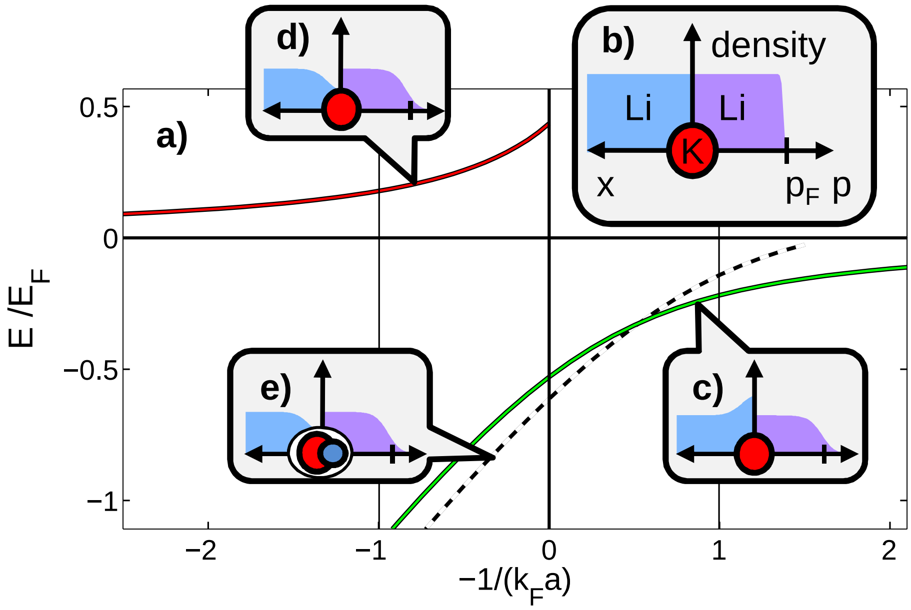

Figure 1.6: **Energetics and illustrations of the polaron and molecule states versus the interaction parameter at $T = 0$.** (a) The interaction energies of the attractive polaron (▬), the repulsive polaron (▬) and the dressed molecule (▬ ▬) are plotted in units of E_F as a function of the interaction strength. (b) In the noninteracting case, the density in real space, where x denotes the distance from the impurity, is constant and the occupation of momentum states drops sharply at $p = p_F$. (c,d) The attractive (repulsive) polaron attracts (repels) its environment and the Fermi edge is softened. (e) Also the molecule interacts repulsively.

of which is given by the red line, see Chap. 7.

It is interesting to picture the influence of the ^{40}K impurity on the ^{6}Li Fermi sea in momentum and in real space. The ansatz from Ref. [Che06] for the polaron wavefunction $|P\rangle$ consists of the impurity at rest $|0\rangle_{\mathrm{K}}$ in the unperturbed Fermi sea $|\mathrm{FS}\rangle_{\mathrm{Li}}$ plus a sum over all possible scattering events of the impurity with one of the ^{6}Li atoms out of the Fermi sea leaving a hole behind, where $\mathbf{q} - \mathbf{p}$ is the momentum change and the particle and the hole are created by $b^{\dagger}_{\mathbf{p}}$ and $b_{\mathbf{q}}$, respectively.

$$|P\rangle = \sqrt{Z}|0\rangle_{\mathrm{K}}|\mathrm{FS}\rangle_{\mathrm{Li}} + \sum_{p<\hbar k_F<q} f_{\mathbf{qp}}|\mathbf{q}-\mathbf{p}\rangle_{\mathrm{K}}\, b^{\dagger}_{\mathbf{p}}\, b_{\mathbf{q}}|\mathrm{FS}\rangle_{\mathrm{Li}} \tag{1.1}$$

The superposition of the free impurity plus the terms capturing the collisions with majority atoms gives immediate meaning to various features of the polaron. The weight of the free impurity $\sqrt{Z}$ gives the wavefunction overlap with the free particle and Z is the QP residue. The excitations in the second term with weights $f_{\mathbf{qp}}$ make up the so-called dressing of the impurity. From this ansatz we can directly infer that the dressing of the impurity gives a softening of the Fermi surface in momentum space. Whereas the momentum state occupation drops sharply at p_F in the noninteracting case, see Fig. 1.6(b), the edge softens in the regime of strong interaction, see Fig. 1.6 (c-e). As the particle-hole excitations have a specific phase relation, they translate into a density distortion of the Fermi sea, which is very intuitive. For attractive (repulsive) interaction, the ^{6}Li density is increased (decreased) around the ^{40}K impurity, see Fig. 1.6(c) (Fig. 1.6(d)). Also the molecule shows this repulsion of the ^{6}Li atoms, see Fig. 1.6(e).

1.5 Future research topics

1.5.1 Itinerant ferromagnetism

The research on ultracold Fermi gases has mainly focused on the ground state properties, with the most prominent example being the BEC-BCS crossover connecting from repulsively interacting molecules to attractively interacting atoms. But also a system of repulsively interacting atoms promises to be an interesting candidate to investigate novel quantum phases. This route was opened in Refs. [Jo09, Zwe09] by searching for the signatures of itinerant ferromagnetism, as predicted by the Stoner model. This model is based on a mean field calculation and was developed to explain ferromagnetism in solid state physics. Translated to ultracold Fermi gases, the interaction energy in the mixed state is compared to the energy of the two components being separated in domains. Above a critical interaction strength, the components are predicted to energetically favor being separated in fully polarized domains, analogous to ferromagnetic domains. However, since this critical interaction strength is high, the applicability of the mean field calculation becomes questionable and more elaborate calculations are needed [Pil10, Cha11], asking for experimental benchmarks. Experimental findings in the ultracold Fermi mixture suggested that the ferromagnetic phase is reached [Jo09] but further studies revealed that the findings result from the instability of the system rather than from the phase transition [San11]. The strong repulsive interactions required to enter the ferromagnetic phase are realized in ultracold Fermi systems by means of a Feshbach resonance, where the energy of the scattering partners gets close to the energy of a bound state in the attractive interatomic potential. For repulsive interactions, this bound state represents an energetically lower state, to which the repulsively interacting atoms may decay. A many-body treatment reveals that this decay towards pairing extends throughout resonance towards the BCS-side. This instability is studied in Ref. [Pek11a] with the result that the pairing instability dominates over the formation of the ferromagnetic phase. However, the authors present in another work [Pek11b] that the pairing instability is reduced at Feshbach resonances with a finite effective range. In fact, we employ a resonance with a considerable effective range comparable to the interparticle spacing, see Methods in Chap. 7. With this effective range we introduce another parameter for the short-range physics. Hence, we leave the terrain of universality and embark on the exploration of new states with a more peculiar system. Such a system already allowed us to investigate a novel quasiparticle, the repulsive polaron, as we prepared few ^{40}K atoms in a Fermi sea of ^{6}Li atoms close to a narrow interspecies resonance, see Chap. 7. Also in this polarized situation, theoretical calculations showed a superior stability of the repulsive state, the repulsive polaron, at a narrow resonance compared to at a wide resonance. With the predicted and experimentally verified increase of stability of the repulsive states, ultracold atoms are back in the game for investigating new quantum phases based on repulsive interactions.

At the time of writing this thesis, we investigate the possible realization of itinerant ferromagnetism in a ^{40}K ^{6}Li mixture at a narrow Feshbach resonance. Therefor, we prepare the mixture similar to when investigating the repulsive polaron (Chap. 7) but with more ^{40}K atoms, leading to comparable densities of the two species in the center of the trap. It is important to note, as a difference to the previously employed homonuclear mixture, that our two species feel a different potential depth. In case of separation, the lowest energy is achieved when one of the two species occupies the center of the trap and is surrounded by the other. This is in contrast to a homonuclear mixture, where the two components see the same trapping potential and may minimize the energy by forming rather small domains. For this reason we expect to observe a macroscopic separation of the two components. Preliminary results indeed show indications of full separation of the two components but the interpretation is still open. We prepare the ^{40}K ^{6}Li mixture far on the BEC side of the resonance at $-1/(\kappa_F a) = -10$ without molecules being formed and then ramp to a variable final magnetic field close to the resonance in about 0.2 ms. In the measurements we explicitly discriminate the free atoms of ^{40}K and ^{6}Li from the atoms bound to ^{40}K -^{6}Li molecules. At about $-1/(\kappa_F a) = -0.25$ we find that the remaining ^{40}K atoms reside in the trap center and the cloud size is reduced while the density of the ^{6}Li atoms drops dramatically in the center and shows an overall increase of the cloud size. Another result is the decay rate of the ^{40}K atoms, which is expected to increase with higher interaction strength. However, we find the decay rate to saturate above a certain value of the interaction strength, which is at the same value of the interaction strength at which the ^{40}K cloud size stops decreasing. These observations are consistent with the separation of the clouds due to the transition to a ferromagnetic state. However, the decay to the lower lying molecular state enriches this scenario and challenges the interpretation of the separation in terms of the transition to a ferromagnet. Simple mean field repulsion already leads to a slight compression of the ^{40}K cloud and a pushing of the ^{6}Li cloud away from the trap center. Now, if all the ^{40}K atoms decay to molecules where the ^{6}Li atom density predominates and vice versa, the resulting atom distributions might suit to our observations and also the decay of ^{40}K atoms might level off as observed. The challenge for upcoming measurements is to get a more quantitative understanding of the involved effects pairing instability and ferromagnetic transition.

1.5.2 Species-selective control

A Fermi-Fermi mixture of two different atomic species opens up a whole new world of possibilities to study new quantum phases [Liu03, Isk07, Nis10] and to explore novel few-body states [Lev09, Nis08]. Some of those proposals require to trap the two species such that their densities are equal throughout the trap. This is not as straightforward as it is for a homonuclear mixture because the two species experience in general different trapping potentials and cannot be levitated simultaneously with a magnetic field gradient. However, other proposals take advantage of the possibility that the two species experience different trapping potentials. In the following we want to present our approach to species selective control by means of a bichromatic optical dipole trap, which will allow for creating identical traps as well as explicitly selective traps for both species. Optical dipole traps and optical lattices are

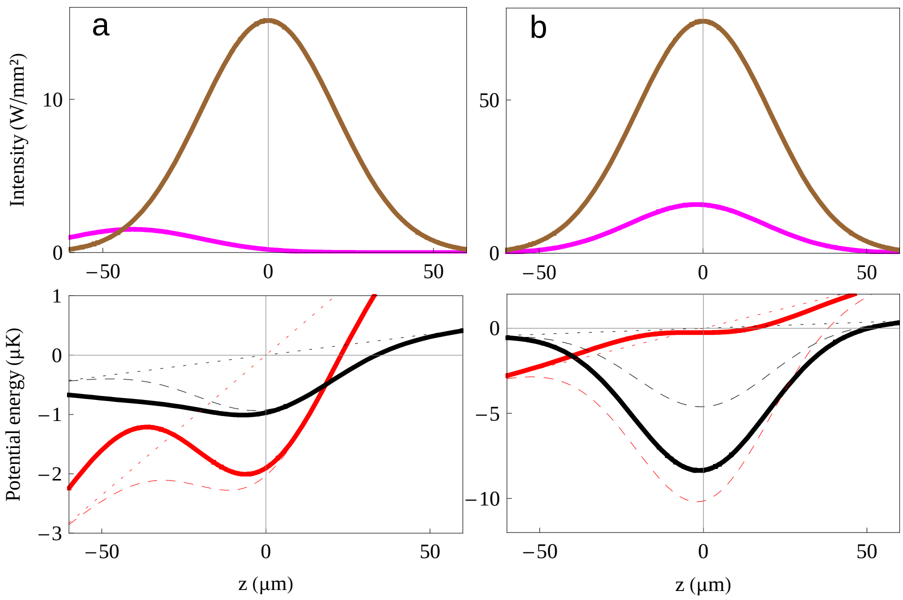

Figure 1.7: **Laser configurations and potentials for two applications of the bichromatic trap.** The upper panels give the intensities of the IR beam (brown) and the 730 nm beam (magenta) as a function of the vertical direction z. The lower panels show the potential energy through gravity (dotted) plus the IR beam (dashed) and plus the 730 nm beam (solid) for ^{40}K (red) and ^{6}Li (black). (a) For a shallow IR beam potential plus gravitational potential, the trap minima of the two species are shifted with respect to each other. This gravitational sag can be compensated through the 730 nm beam, when shifted with respect to the IR beam. (b) The 730 nm beam may be used to compensate for the trapping potential of the IR beam.

usually implemented with far-detuned light to avoid spontaneous scattering [Gri00]. Thus the two states in homonuclear mixtures usually experience nearly identical light shifts. The different optical transitions of ^{6}Li (≈671 nm) and ^{40}K (≈767 nm), however, let us control the two species selectively [Ono04, Ler11].

One application is to adjust the trap frequencies of the ^{6}Li and ^{40}K atoms selectively. Our present optical dipole trap is realized using light with a wavelength of 1064 nm, creating an attractive potential for both species, which is about 2 times deeper for ^{40}K atoms than for ^{6}Li atoms. To implement the bichromatic trap, we provide a light source with tunable wavelength from 720 nm to 800 nm. Let us assume we superimpose the beam at 730 nm to the present optical dipole trap beam at 1064 nm. The trap depth and trap frequencies increase for the ^{6}Li atoms but decrease for the ^{40}K atoms. In the following we mention three possible applications. (1) One is to optimize the conditions for Cooper-type pairing and superfluidity to occur. This requires a matching of the Fermi surfaces and of the densities of the two species, which implies equal Fermi momenta and equal Thomas-Fermi radii. Both requirements can only be fulfilled when the atom numbers are equal and the trap frequencies have the inverse ratio of the masses, i.e. $\omega_{\mathrm{Li}}/\omega_{\mathrm{K}} = m_{\mathrm{K}}/m_{\mathrm{Li}}$. We can achieve this condition in the two radial directions by shining in the 730 nm beam with 19 % of the power of the 1064 nm beam, provided that both beams have the same waist. To match the densities in the axial direction we plan to use a box with hard walls derived from a 532 nm light source, which equally confines both species. (2) A second application is to compensate for the different gravitational sag of the ^{6}Li and ^{40}K atoms, which leads to a relative displacement of the two species in the optical dipole trap, see Fig. 1.7(a). Commonly, a magnetic gradient field can be used to compensate for the gravitational force. However, as the ^{6}Li and ^{40}K atoms have different masses but similar magnetic moment, we cannot levitate both at the same time. The additional degree of freedom to compensate for the different gravitational sag is the vertical displacement of the 730 nm beam relative to the 1064 nm beam. Placing the 730 nm beam below the 1064 nm beam pulls the ^{6}Li atoms down and pushes the ^{40}K atoms up, as needed to compensate for the larger sag of the heavy ^{40}K atoms. (3) A third application is to realize a *pure atom* trap, meaning that the ^{40}K atoms are purely trapped through the interactions with the ^{6}Li cloud. We can achieve this by shining in the 730 nm with 21 % of the power of the 1064 nm beam, provided that both beams have the same waist, see Fig. 1.7(b). This toy experiment may take us to more elaborate systems. Imagine one species interacting with another species that is confined in a lattice and can feature phonons or that is confined in a random potential and can lead to Anderson localization of the first species [Bil08, Roa08].

Another possibility is to implement a species-selective lattice. Let us assume we set up a lattice with light at 730 nm. In terms of recoil energy, the lattice depth is about 18 times deeper for ^{40}K atoms than for ^{6}Li atoms and the factor can be even larger for a wavelength closer to 767 nm. With such a lattice in n dimensions we can reduce the dimensionality of the ^{40}K atoms to $3 - n$, while not affecting the dimensionality of the ^{6}Li atoms. This dramatically affects the two-body interaction leading to confinement induced resonances [Ols98, Ber03, Mor05, Lam10, Hal10]. Interesting few-body effects can also be addressed, e.g. a p-wave resonance between ^{40}K -^{6}Li dimers and ^{40}K atoms tuneable by the lattice depth [Lev09] or the Efimov-effect in mixed dimensions [Nis09b]. In terms of many-body physics, new quantum phases may be studied, e.g. ^{6}Li can mediate interactions between ^{40}K atoms in different layers, which may lead to interlayer superfluidity [Nis10].

1.6 Topics at a glance

The present thesis covers six topics, presented in the following six chapters. Here, we survey the topics at a glance.

Chapter 2, *Lifetime of angular momentum in a rotating strongly interacting Fermi gas*: We set a strongly interacting Fermi gas in rotation and study the lifetime of the angular momentum as a function of interaction strength and trap ellipticity. The rotation is measured by tracing the precession of the radial quadrupole mode oscillation, see Fig. 1.8. We find that the deeply hydrodynamic behavior in the normal phase leads to a very long lifetime.

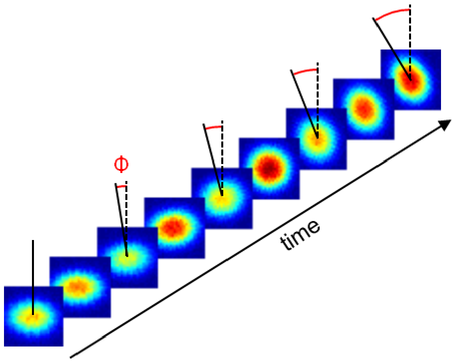

Figure 1.8: **Time series of a precessing quadrupole mode oscillation.** The main axes of the excitation, one of which is shown by the solid line, precesses by the angle Φ. From this precession we can extract the angular momentum of the gas.

Chapter 3, *Quenching of the moment of inertia in a strongly interacting Fermi gas*: We report on the observation of a reduced moment of inertia of the strongly interacting, ultracold gas as compared to a classical gas. This is a striking consequence of superfluidity. The basic idea of the measurement is sketched in Fig. 1.9. Investigating the moment of inertia as a function of temperature reveals the critical temperature for the transition to the superfluid phase.

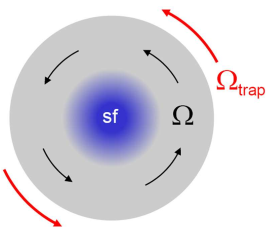

Figure 1.9: **Illustration of a strongly interacting Fermi gas in a trap, slowly rotating with Ω_{trap}.** The classical part in the outer trap region rotates with a frequency Ω. The superfluid core cannot rotate, unless vortices are excited, and does not contribute to the moment of inertia.

Chapter 4, *Observation of interference between two molecular Bose-Einstein condensates*: We observe the interference between two independent Bose-Einstein condensates of weakly bound Feshbach molecules, see Fig. 1.10. The fringe spacing is determined by the de Broglie wavelength of the molecules. We study the penetration of the two condensates towards the regime of strong interaction and find that collisions reduce the fringe contrast and that they eventually collide hydrodynamically.

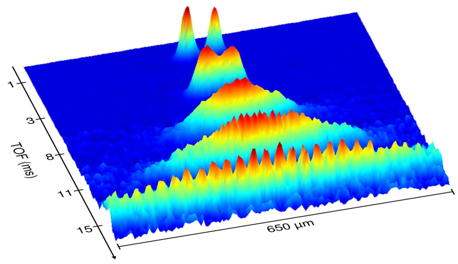

Figure 1.10: **Interference of two molecular Bose-Einstein condensates.** The two clouds expand and overlap in time of flight (TOF) and an interference pattern emerges.

Chapter 5, *Feshbach resonances in the ^{40}K ^{6}Li Fermi-Fermi mixture: Elastic versus inelastic interactions*: This is a detailed study of the Feshbach resonances between fermionic ^{6}Li and ^{40}K atoms, see Fig. 1.11. Experimentally, we study the elastic and inelastic scattering properties at the resonance located at about 155 G. The results fully agree with the theoretical calculations based on a coupled channels calculation. We also present a survey of resonances in the system.

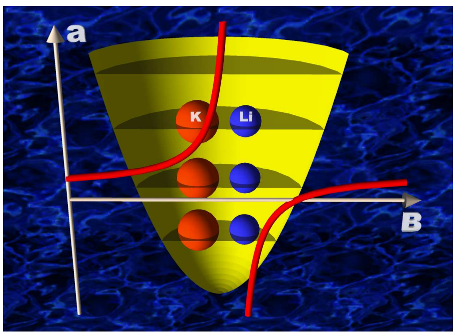

Figure 1.11: **Controlling the scattering length between fermionic ^{6}Li and ^{40}K atoms** The occupation of the low-energy levels in the harmonic trap illustrates the degeneracy of the sample. The interspecies elastic scattering, parameterized by the scattering length a, is tuned by the magnetic field B

Chapter 6, *Hydrodynamic Expansion of a Strongly Interacting Fermi-Fermi Mixture*: We show that the strongly interacting regime can be reached in the ^{40}K ^{6}Li Fermi-Fermi mixture, by observing hydrodynamic expansion. The hydrodynamic behavior leads to two observables: The inversion of the aspect ratio and the drag between the two species, both sketched in Fig. 1.12.

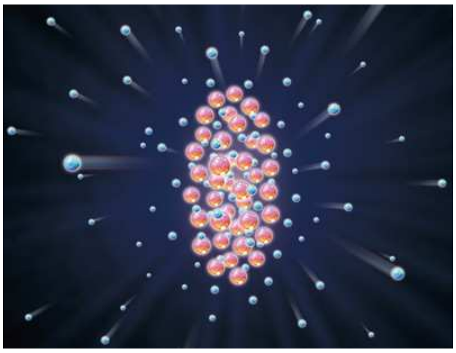

Figure 1.12: **Hydrodynamic expansion of a strongly interacting mixture of ^{40}K (red) and ^{6}Li (blue).** In general the light ^{6}Li atoms expand much faster. However, where the two species overlap they drag each other and expand collectively. Also the elliptic shape of the core indicates the nonballistic, hydrodynamic expansion. (Credit: Ritsch)

Chapter 7, *Metastability and coherence of repulsive polarons in a strongly interacting Fermi mixture*: We study the excitation spectrum of ^{40}K impurities in a Fermi sea of ^{6}Li by means of radio-frequency spectroscopy. We identify a novel quasiparticle state, the repulsive polaron, being a ^{40}K atom dressed by excitations of the Fermi sea of ^{6}Li, see Fig. 1.13. We measure the quasiparticle properties like its interaction energy, its lifetime and its quasiparticle residue.

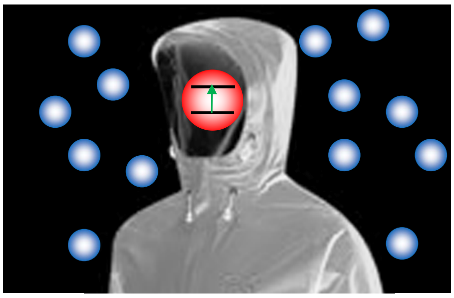

Figure 1.13: **A dressed ^{40}K impurity.** The impurity (^{40}K atom in red) affects the medium (^{6}Li atoms in blue) and it becomes dressed by excitations of the medium. The key concept of Fermi liquid theory by L. Landau is to describe the impurity plus the dressing as a quasiparticle. We probe the quasiparticle properties by driving radio-frequency spectroscopy, depicted by the transition in the two-level system.

CHAPTER 2

PUBLICATION

Lifetime of angular momentum in a rotating strongly interacting Fermi gas [1]

Phys. Rev. A 79, 053628 (2009)

S. Riedl,[1,2] E. R. Sánchez Guajardo,[1,2] C. Kohstall,[1,2] J. Hecker Denschlag,[1] and R. Grimm[1,2]

[1] *Institut für Experimentalphysik und Zentrum für Quantenphysik, Universität Innsbruck, 6020 Innsbruck, Austria*

[2] *Institut für Quantenoptik und Quanteninformation, Österreichische Akademie der Wissenschaften, 6020 Innsbruck, Austria*

We investigate the lifetime of angular momentum in an ultracold strongly interacting Fermi gas, confined in a trap with controllable ellipticity. To determine the angular momentum we measure the precession of the radial quadrupole mode. We find that in the vicinity of a Feshbach resonance, the deeply hydrodynamic behavior in the normal phase leads to a very long lifetime of the angular momentum. Furthermore, we examine the dependence of the decay rate of the angular momentum on the ellipticity of the trapping potential and the interaction strength. The results are in general agreement with the theoretically expected behavior for a Boltzmann gas.

2.1 Introduction

The dynamics of an ultracold quantum gas is an important source of information on the physical nature of the system. A particularly interesting situation is an atomic Fermi gas

[1] The primary contribution of the author of the present thesis to this publication is the setup of a deflection system for the trapping laser beam [Koh07] to be able to create the special time-averaged optical dipole potentials. He also contributed to data acquisition.

in the vicinity of a Feshbach resonance [Ing08a, Gio08]. The Feshbach resonance allows us to tune the two-body interaction and thus to control the coupling between the atoms. It connects a molecular Bose-Einstein condensate (BEC) with a Bardeen-Cooper-Schrieffer (BCS) superfluid. In the crossover region between these two limiting cases, the center of the Feshbach resonance is of special interest. Here the unitarity-limited interactions lead to universal behavior of the Fermi gas.

The strong two-body interactions close to the Feshbach resonance lead to very low viscosity and hydrodynamic behavior in the normal phase, similar to the properties of a superfluid [Cla07, Wri07]. The coexistence of normal and superfluid hydrodynamic behavior is a special property of the strongly interacting Fermi gas, which stands in contrast to ultracold Bose gases, where deep hydrodynamic behavior is usually restricted to the superfluid condensate fraction. The low-viscosity hydrodynamic behavior leads to a long lifetime of collective motion in the system. Using collective modes the dynamics has been investigated in a broad range of temperatures and interaction strengths in the crossover region [Cla07, Wri07, Bar04a, Kin04a, Kin04b, Kin05a, Alt07a, Alt07b, Rie08], including the hydrodynamic regime in the normal phase. Another important collective motion is the rotation of the gas, which is of particular interest in relation to superfluidity [Zwi05b].

In this Article, we study the lifetime of the angular momentum of a rotating strongly interacting Fermi gas. We determine the angular momentum using the precession of the radial quadrupole mode. This method is well established to study the angular momentum in experiments with BEC [Che00, Hal01a, Lea02]. We observe that the unique hydrodynamic behavior of the strongly interacting Fermi gas leads to particularly long lifetimes of the angular momentum. We perform a quantitative analysis of the dissipation of the angular momentum caused by the trap anisotropy for a gas in the unitarity limit. The measurements show general agreement with the expected behavior for a Boltzmann gas [GO00]. As shown in a previous study comparing experiment and theory [Rie08], a Boltzmann gas describes the behavior of a gas in the normal state with unitarity-limited interactions reasonably well. Finally we study the dependence of the lifetime on the interaction strength of the gas in the crossover region between the BEC and BCS regime.

2.2 Experimental procedure

To realize an ultracold strongly interacting Fermi gas we trap and cool an equal mixture of ^{6}Li atoms in the lowest two atomic states as described in our previous work [Joc03b, Alt07b]. We control the interparticle interaction by changing the external magnetic field in the vicinity of a broad Feshbach resonance centered at 834 G [Bar05]. The atoms are held by an optical dipole trap using a red-detuned single focused laser beam and an additional magnetic trap along the beam; this magnetic confinement dominates over the optical confinement along the beam under the conditions of the present experiments. The resulting trap provides weak confinement along the beam (z axis) and stronger transverse confinement (x-y plane), leading to a cigar-shaped cloud. The trap is well approximated by a harmonic potential with trap frequencies $\omega_x \approx \omega_y \approx 2\pi \times 800\,\mathrm{Hz}$ and $\omega_z = 2\pi \times 25\,\mathrm{Hz}$. The trap, in general, also has a small transverse ellipticity, which can be controlled during the experiments. We define an

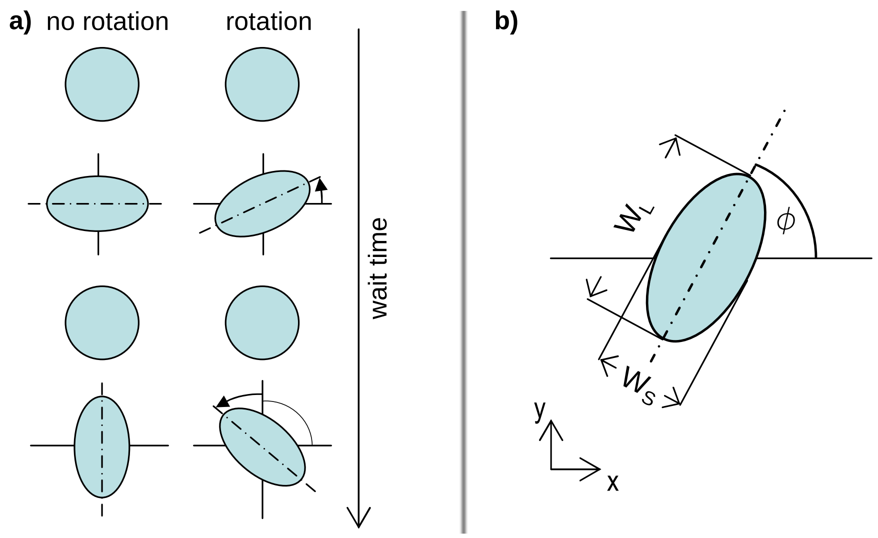

Figure 2.1: Oscillation of the cloud after excitation of the radial quadrupole mode. For a rotating hydrodynamic gas the principal axes of the quadrupole mode oscillation precess with a frequency determined by the angular momentum of the gas. To follow the precession we measure the angle of the long axis of the cloud. Note that every half oscillation period this angle changes by $\pi/2$ because of the mode oscillation; see also Fig. 2.2. The oscillation of the cloud shape is determined by measuring the widths along the short (W_S) and the long axis (W_L) of the cloud.

average transverse trap frequency as $\omega_r = \sqrt{\omega_x \omega_y}$. The Fermi energy of the noninteracting gas is given by $E_F = \hbar(3N\omega_x\omega_y\omega_z)^{1/3} = \hbar^2 k_F^2/2M$ where $N = 5 \times 10^5$ is the total atom number, M is the atomic mass, and k_F is the Fermi wave number. The corresponding Fermi temperature is $T_F = E_F/k = 1.3\,\mu$K, with k as the Boltzmann constant. The interaction strength is characterized by the dimensionless parameter $1/k_F a$, where a is the atomic s-wave scattering length.

To dynamically control the shape of the trapping potential in the transverse plane, we use a rapid spatial modulation of the trapping laser beam by two acousto-optical deflectors, which allows us to create time-averaged trapping potentials [Alt07b]. The control over the potential shape has two different applications for the measurements. As a first application we use it to adjust the static ellipticity $\epsilon = (\omega_x^2 - \omega_y^2)/(\omega_x^2 + \omega_y^2)$ of the trap in the x-y plane. This allows us to compensate for residual ellipticity of the trapping potential, i.e., of the trapping laser beam, and also to induce a well defined ellipticity. The second application is the creation of a rotating elliptic potential with a constant ellipticity ϵ' [2]. This is needed to spin up the gas. Both the static ellipticity in the x-y plane and the rotating elliptic potential can be controlled independently. To determine the ellipticity we measure the frequency of the sloshing mode along the two principal axes of the elliptic potential. This allows controlling the ellipticity with an accuracy down to typically 0.005.

[2] $\epsilon' = (\omega_x'^2 - \omega_y'^2)/(\omega_x'^2 + \omega_y'^2)$, where ω_x' and ω_y' are the trap frequencies in the frame of the rotating potential.

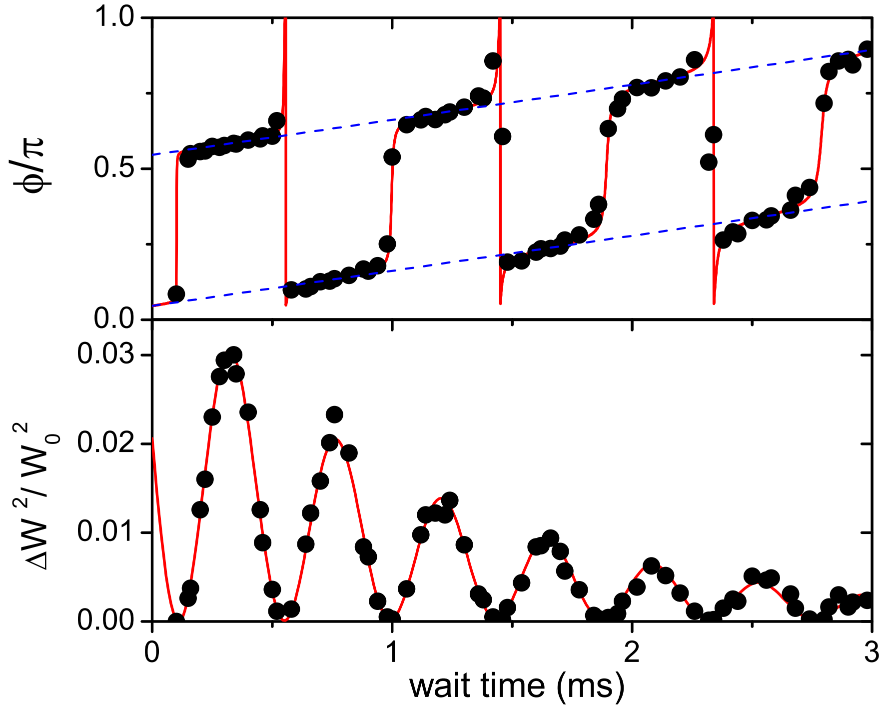

Figure 2.2: Evolution of the quadrupole mode in a rotating Fermi gas in the unitarity limit. The upper panel shows the precession of the principal axes of the mode. The experimental data are shown by the dots. The solid line represents a fit according to Eq. 2.2. The dashed lines correspond to the idealized precession of the angle when there is no damping present in the mode. Whenever the oscillation of the difference in widths $\Delta W^2/W_0^2$ (lower panel) has a local maximum the observed precession angle coincides with the idealized precession. The parameter W_0 is the average width of the cloud. The finite value of ϕ at zero wait time results from the precession of the cloud during expansion. Here $L_z = 1.7\hbar$ and $T/T_F \approx 0.2$.

To measure the angular momentum of the cloud, we exploit the fact that collective excitation modes are sensitive to the rotation of the cloud. Here we use the precession of the radial quadrupole mode to determine the angular momentum of the rotating cloud; see Fig. 2.1. This method works under the general condition that the gas behaves hydrodynamically [Che03]. In our case of a strongly interacting Fermi gas, this method probes both the superfluid and the classically hydrodynamic part and does not distinguish between these two components. For the case of atomic BEC, the precession has been well studied in theory [Sin97, Dod97, Svi98, Zam98] and used in experiments to determine the angular momentum of the BEC [Che00, Hal01a, Lea02]. For an atomic BEC the non-condensed part is usually collisionless and does not contribute to the mode precession.

The radial quadrupole mode consists of two collective excitations with angular quantum numbers $m = +2$ and $m = -2$ and frequencies ω_+ and ω_-, respectively. These two excitations correspond to an elliptic deformation of the cloud rotating in opposite directions. The superposition of the excitations results in the radial quadrupole mode. For a gas at rest the two excitations are degenerate, while for a gas carrying angular momentum the frequencies are different, which causes a precession of the mode, see Fig. 2.1. The mode precesses with a frequency $\Omega_\phi = (\omega_+ - \omega_-)/4$. The angular momentum itself can be calculated from the precession frequency [Zam98] using

$$\Omega_\phi = L_z/(2Mr_{\mathrm{rms}}^2). \tag{2.1}$$

Here L_z is the average angular momentum per atom and r_{rms}^2 is the mean value of $x^2 + y^2$ of the density distribution[3].

To excite the quadrupole mode we switch on an elliptic potential for $50\,\mu$s; this short elliptic deformation does not affect the angular momentum of the gas. For the excitation we make sure that ω_r does not change. This ensures that no compression mode is excited and only an equal superposition of the $m = \pm 2$ modes is created [Alt07b].

To follow the quadrupole oscillation we determine the angle of the long axis, ϕ, and the difference of the widths along the principle axes of the cloud, $\Delta W = W_L - W_S$, after a variable wait time in the trap; see Fig. 2.1. Therefore we fit a zero-temperature two-dimensional Thomas-Fermi profile to absorption images[4]. We also keep the angle of the long axis a free fit parameter. The width of the cloud is defined as twice the Thomas-Fermi radius.

To resolve the density distribution in the x-y plane, we let the cloud expand for 0.8 ms before taking the image. The expansion does not only increase the width of the cloud but also leads to an increase in the precession angle as a consequence of the angular momentum. A quantitative analysis of the small contribution to the total precession angle that results from the expansion is given in Appendix B.

Figure 2.2 shows the evolution of the precessing quadrupole mode. The upper part shows the precession angle. The finite value of ϕ at zero wait time results from the expansion. The periodic jumps of the precession angle reflect the alternation between the long and the short axis while the quadrupole mode evolves. As the precession proceeds, these jumps become more and more smooth. This is caused by stronger damping of the $m = -2$ excitation compared to the $m = +2$ excitation. Similar behavior has been observed in Ref. [Bre03] for the case of a BEC. There the authors discussed two possible mechanisms where the difference in damping is due to either a rotating thermal cloud [Wil02] or Kelvin mode excitations [Che03]. From our measurements we cannot discriminate between these two mechanisms.

To fit the observed precession of the quadrupole mode, we use the function given in Appendix A. We find very good agreement between the data and the expected behavior. For the data set shown in Fig. 2.2 the angular momentum is $1.7\hbar$. The average damping rate is $(\Gamma_- + \Gamma_+)/2 = (460 \pm 30)\,\mathrm{s}^{-1}$, while the difference in the damping rate of the $m = -2$ compared to the $m = +2$ excitation is $\Gamma_- - \Gamma_+ = (80 \pm 40)\,\mathrm{s}^{-1}$.

We find that a simplified procedure can be used to determine the angular momentum from a single measurement, instead of fitting the whole precession curve. If the measurement

[3] We determine r_{rms} at unitarity from the trap parameters using $E_F = 2M\omega_r^2 r_{\mathrm{rms}}^2\sqrt{1+\beta}$ where we used the universal scaling parameter $\beta = -0.56$ [Gio08]. Note that this underestimates r_{rms} by a few percent because it does not take into account the finite temperature and the rotation of the gas. This does not effect the measurement of the lifetime of rotation as this depends on the relative change of L_z.

[4] For the parameters used in the experiment a zero temperature Thomas-Fermi profile fits the density distribution reasonably well.

is taken at a time when ΔW^2 has a local maximum, the precession angle ϕ is independent of the distortion caused by the difference in the damping rates between the two excitations; see Fig. 2.2. This allows us to determine the difference $\omega_+ - \omega_- = 4\,\phi/\Delta t$ and therefore to determine L_z with a single measurement. The duration Δt is the sum of the wait time in the trap and an effective precession time t_e, which accounts for the precession of the quadrupole mode during expansion as discussed in Appendix B. Depending on the damping of the mode oscillation, we measure the precession angle at the first or second maximum[5] of ΔW^2.

To determine the temperature of the gas in the unitarity limit, we first adiabatically change the magnetic field to 1132 G [6], where $1/k_F a \approx -1$, to reduce the effect of interactions on the density distribution [Luo07]. Under this condition, for $T > 0.2T_F$, the interaction effect on the density distribution is sufficiently weak to treat the gas as a noninteracting one and to determine the temperature from time-of-flight images. We fit the density distribution after 2 ms release from the trap to a finite-temperature Thomas-Fermi profile. The temperature measured at 1132 G is converted to the temperature in the unitarity limit under the assumption that the conversion takes place isentropically, following the approach of Ref. [Che05a].

2.3 Spinning up the gas

To spin up the gas we introduce a rotating anisotropy into the initially round trap in the x-y plane. More specifically, we suddenly switch to a rotating elliptic trap potential with a rotation frequency Ω_t and ellipticity $\epsilon' = 0.03$, rotate for a time t_{rot} on the order of 100 ms, and then ramp down the ellipticity in 50 ms while the trap is still rotating.

In the case of hydrodynamic behavior of the gas this spinning up method is resonantly enhanced in a certain range of rotation frequencies; see Fig. 2.3. The reason for this behavior is the resonant excitation of quadrupolar flow which leads to a dynamic instability when Ω_t is close to half the oscillation frequency of the radial quadrupole mode $\omega_q/2 = 0.71\omega_r$. This effect was used to nucleate vortices in a BEC [Mad00b] and was further studied in Refs. [Mad01, Hod02]. A signature of the resonant excitation is a strong elliptic deformation of the cloud shape which exceeds the ellipticity of the trap ϵ' during the spin-up process. We clearly see this effect when we spin up the gas. We also find that the rotation frequency where L_z starts to increase strongly depends on ϵ' and t_{rot} in a similar way as it was observed in Refs. [Mad01, Hod02]. Note that we cannot draw any conclusion concerning superfluidity from the resonant behavior of L_z in Fig. 2.3 because it is only a consequence of hydrodynamic behavior and the strongly interacting gas is hydrodynamic both below and above T_c. In fact, for temperatures clearly above T_c we a find similar behavior for L_z as a function of Ω_t.

For an atomic BEC, L_z was found to first increase abruptly from 0 to $1\hbar$ with Ω_t, caused by the appearance of a centered vortex [Che00]. As the formation of pairs is necessary for superfluidity in the BEC-BCS crossover regime, the angular momentum per atom of a

[5] Note that the frequency of quadrupole mode oscillation ω_q depends on the rotation frequency of the gas via $\omega_q^2 = 2\omega_r^2 - \Omega^2$. This leads to a tiny shift of the maxima of ΔW^2 but does not affect our measurement of L_z within our experimental uncertainty.

[6] This is the largest magnetic field where absorption images can be taken with our current experimental setup.

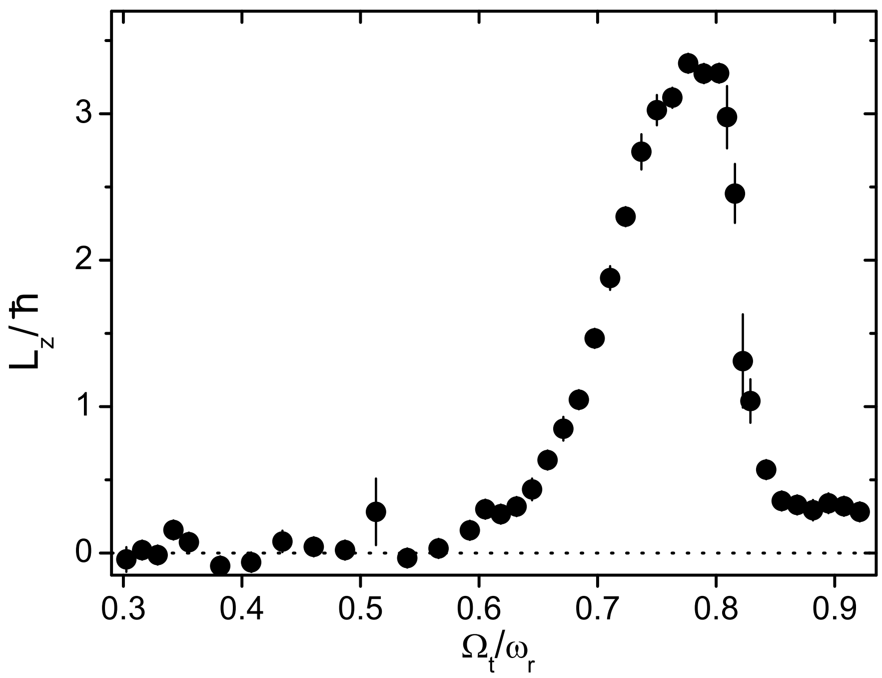

Figure 2.3: The angular momentum L_z as a function of the rotation frequency Ω_t of the elliptic trap. Here we spin up the gas for $t_{\mathrm{rot}} = 60\,\mathrm{ms}$. The temperature is $T/T_F \approx 0.2$. The gas is in the unitarity limit.

single vortex in the center of the cloud amounts to $L_z = \hbar/2$. We do not observe such an abrupt increase in L_z. Nevertheless this does not exclude that vortices are created during our spin-up process; the abrupt change in L_z is not a necessary consequence of the creation of vortices as the angular momentum of a vortex depends on its position in an inhomogeneous gas [Che00]. Furthermore our measurement of L_z cannot distinguish between the angular momentum carried by the superfluid and the normal part of the cloud. Also, we cannot directly observe vortices in our absorption images; we believe that the reason is the very elongated cloud which strongly decreases the contrast of the vortex core in the absorption images.

During our spin-up process we observe a significant heating of the gas depending on the rotation frequency and the rotation time. We keep these two parameters as small as possible. We find that a rotation frequency of $\Omega_t/\omega_r = 0.6$ and $t_{\mathrm{rot}} = 200\,\mathrm{ms}$ lead to an angular momentum of about $L_z = 2\hbar$. This is sufficient to perform the measurements, and at the same time does only moderately increase the temperature.

We determine the temperature of the gas after the spin-up process. To avoid complications in the temperature measurement, we wait until the rotation has completely decayed. To keep this wait time short, on the order of 100 ms, we speed up the decay by increasing the ellipticity of the trap; see discussion below. Note that the low initial angular momentum used in the experiments, always staying below $3\hbar$, does not lead to a significant increase in

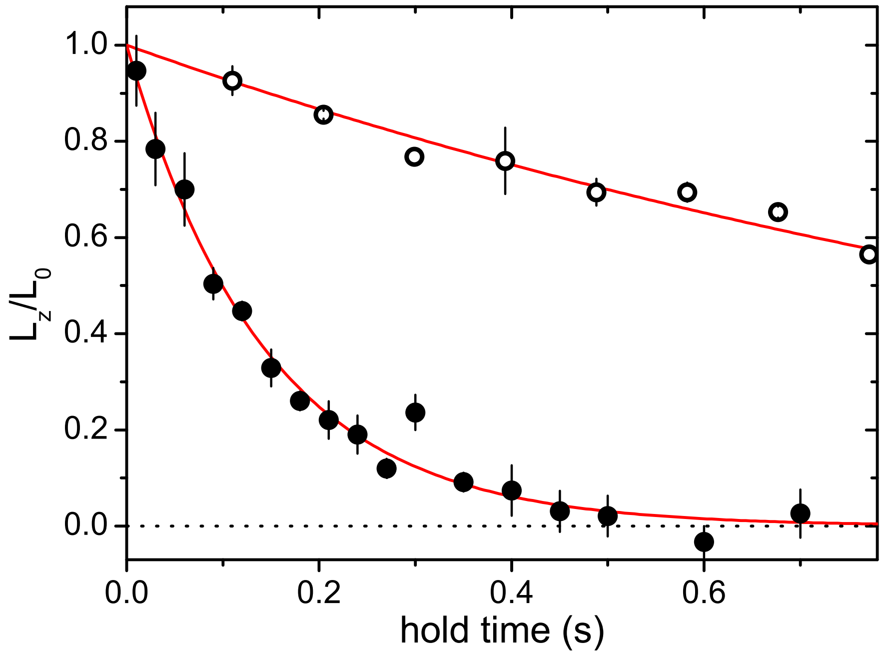

Figure 2.4: Decay of the angular momentum L_z for a gas in the unitarity limit. The temperature is $T/T_F = 0.22(3)$. We fit an exponential decay behavior (solid lines) to the experimental data points. For low ellipticity $\epsilon = 0.009$ (open dots) the lifetime is 1.4 s, while at higher ellipticity $\epsilon = 0.1$ (filled dots) the lifetime is only 0.14 s. To better see the difference of the lifetime for the two ellipticities we normalized L_z by its initial value L_0. For the lower ellipticity $L_0 = 2.2\hbar$ and for the higher ellipticity $1.6\hbar$.

the temperature when the rotation energy is completely converted into heat[7].

2.4 Lifetime of the angular momentum

In an elliptic trap the angular momentum is not a conserved quantity and hence can decay. The dissipation of L_z is due to the friction of the gas caused by the trap anisotropy. Here we investigate the dependence of the decay of L_z on the static ellipticity for the case of unitarity-limited interactions. We compare our experimental results to the predicted behavior for a rotating Boltzmann gas [GO00]. Finally we study the dependence of the decay rate on the interaction strength in the BEC-BCS crossover regime.

The fact that the gas consists of two different components, the normal and the superfluid part, leads in general to a complex behavior for the decay of L_z. For example, in the case of a BEC an exponential decay is related to the corotation of the thermal cloud with the condensate [Zhu01, AS02]. When the thermal cloud is not rotating, theoretical [Zhu01] and

[7]To estimate the increase of the temperature through the decay of the rotation we assume that the rotation energy is completely converted into heat. In the experiments L_z is well below $3\hbar$ which leads to a relative temperature increase of $\Delta T/T < 0.02$ in the relevant temperature range. This is clearly below the uncertainty of our temperature measurement.

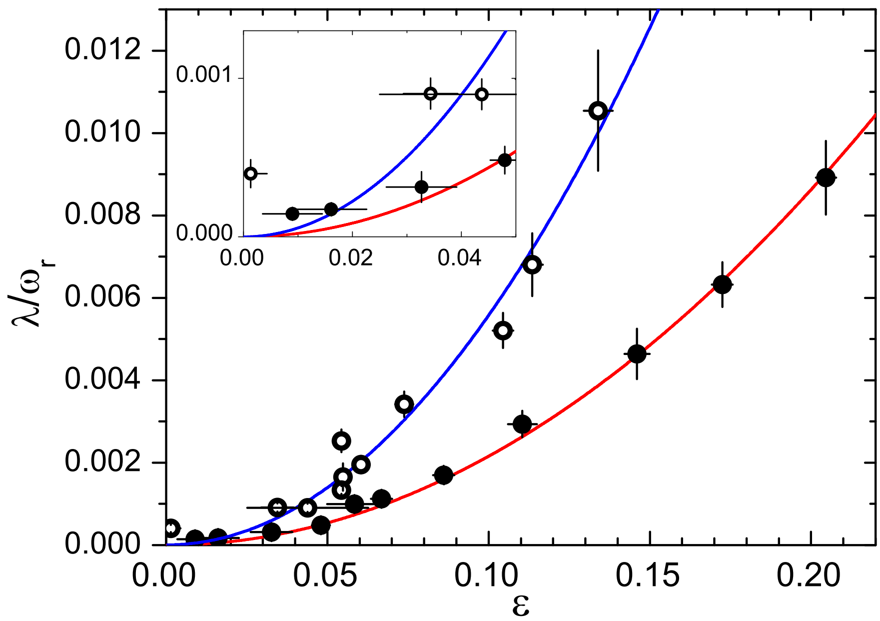

Figure 2.5: Normalized decay rate of the angular momentum as a function of the ellipticity for a gas in the unitarity limit. The temperatures are $T/T_F = 0.22(3)$ (filled dots) and 0.35(2) (open dots). The solid lines are fits based on the expected behavior for a Boltzmann gas [GO00]. The inset shows the low ellipticity region.

experimental [Mad00b] studies show nonexponetial behavior. For a gas completely in the hydrodynamic regime it is expected that the decrease in L_z has an exponential form [GO00].

To measure the decay rate of the angular momentum, we use the following procedure. After spinning up the gas as discussed in Sec. 2.3, we slowly increase the static ellipticity within 10 ms, wait for a certain hold time to let the angular momentum partially decay, and then we remove the ellipticity again within 10 ms. Finally we excite the radial quadrupole mode and observe the precession to determine L_z using the simplified procedure discussed earlier.

In Fig. 2.4 we show two examples for the decay of L_z. We find that the decay of the angular momentum perfectly fits an exponential behavior for all the static ellipticities, temperatures, and interaction strengths we used. For the lowest temperatures obtained, the lifetime for a gas in the unitarity limit goes up to 1.4 s, presumably limited by a residual anisotropy of the trap. This lifetime is by more than a factor of thousand larger than the radial trap oscillation period. Furthermore the lifetime of the angular momentum is much larger than the lifetime of collective excitation modes. For example, the lifetime of the radial quadrupole mode under the same conditions is only 2 ms. A larger ellipticity of the trap significantly decreases the lifetime of L_z.

In the following we investigate quantitatively the dependence of the decay rate of the angular momentum, λ, on ellipticity and temperature. The experimental results are shown in Fig. 2.5 for two different temperatures. The full circles display the data for a temperature of $T/T_F = 0.22(3)$ and the open circles correspond to a temperature of $T/T_F = 0.35(2)$. For better comparison with theory, we plot the normalized decay rate λ/ω_r. A strong increase in the decay rate with increasing ellipticity shows the important role of the trap anisotropy on the lifetime of the angular momentum. For both temperatures the qualitative behavior of the decay rate is the same.

Next we compare the behavior of the decay rate with a theoretical prediction for a Boltzmann gas [GO00]. As we showed recently in Ref. [Rie08], a Boltzmann gas describes the behavior of a unitarity-limited gas in the normal state reasonably well. The predicted behavior of the decay rate is given by $\lambda/\omega_r = 2\epsilon^2\omega_r\tau$ under the assumption that $\epsilon \ll 1/(4\omega_r\tau)$[8], where τ is the relaxation time or effective collision time [Rie08, Vic00, Hua87]. This condition is well fulfilled in our system because the gas is in the hydrodynamic regime where $\omega_r\tau \ll 1$. We compare this theoretical prediction, with τ as a free parameter, to our measurements. We find $\omega_r\tau = 0.108(5)$ for the lower temperature and $\omega_r\tau = 0.28(1)$ for the higher temperature data.

Note that at very low ellipticity, $\epsilon < 0.02$, the observed decay rate for both temperatures lies significantly above the expected behavior; see inset of Fig. 2.5. We attribute this to an additional anisotropy of the trap beyond simple ellipticity. This weak anisotropy becomes relevant only at very low ϵ. Furthermore the finite linear heating rate of the trapped gas of $0.05T_F\,\mathrm{s}^{-1}$ becomes important when the decay rate is very low, which means that the lifetime of L_z is on the order of seconds. In this case the temperature cannot be assumed to be constant during the decay of L_z.

A recent calculation of the relaxation time τ for a Fermi gas in the unitarity limit [Rie08] allows us to compare the experimental values for $\omega_r\tau$ to theory. For $T/T_F = 0.35$ the obtained relaxation time of $\omega_r\tau = 0.28$ is clearly larger than the calculated value of $\omega_r\tau = 0.13$. This means that the theory predicts that the gas is somewhat deeper in the hydrodynamic regime compared to the experimental findings. Similar deviations showed up when the theory was compared to the temperature dependence of collective oscillations [Rie08]. For the lower temperature the obtained value for $\omega_r\tau$ cannot be compared to the calculation of Ref. [Rie08] as the theory is restricted to higher temperatures.

Finally we study the decay of the angular momentum in the crossover region between the BEC and BCS regimes. We measure the decay rate for different interaction parameters $1/k_Fa$. The experimental sequence is the same as for the decay rate in the unitarity limit beside ramping the magnetic field to the desired value in 100 ms before increasing the ellipticity and ramping back the magnetic field in 100 ms before exciting the quadrupole mode. Here the magnetic field is changed slowly such that the gas is not collectively excited. The ellipticity for all magnetic fields is set to be $\epsilon = 0.09$. This sizeable value of ϵ ensures that a small anisotropy beyond ellipticity does not affect the decay rate and makes the measurement less sensitive to heating while the angular momentum damps out as discussed above.

Figure 2.6 shows the decay rate of the angular momentum as a function of the interaction strength. The lifetime is largest where the interaction is strongest and accordingly the relaxation time is short. In addition to the two-body interaction strength, pairing effects play an important role for the relaxation time [Rie08]. This might explain the higher decay rates for $1/k_Fa < 0$, where the pairing is weak, compared to the decay rates for $1/k_Fa > 0$,

[8] For the temperatures used in the measurements $1/(4\omega_r\tau) > 0.9$ for a gas in the unitarity limit.

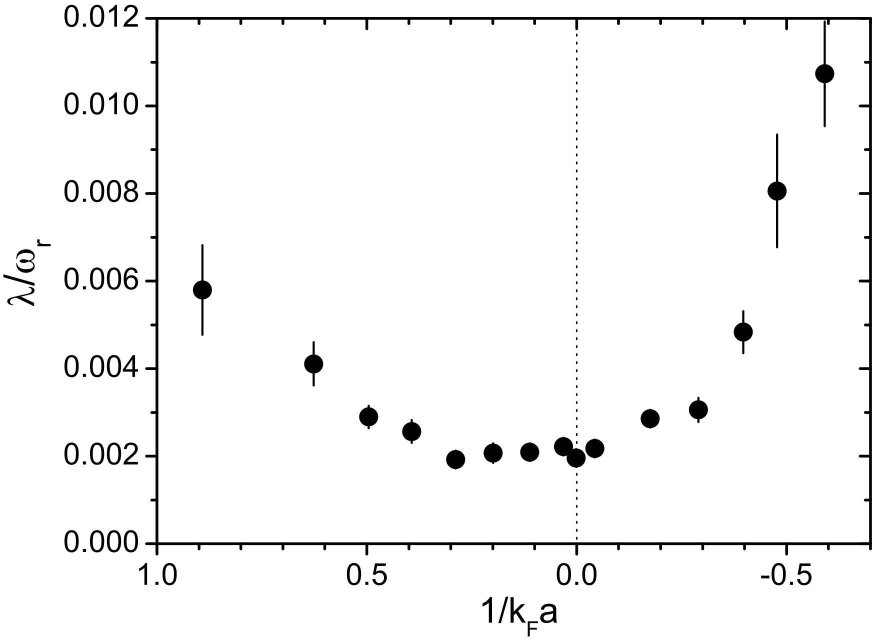

Figure 2.6: Lifetime of the angular momentum versus interaction parameter $1/k_F a$ for $\epsilon = 0.09$. The temperature for $1/k_F a = 0$ is $T/T_F = 0.22(3)$.

where the atoms are bound to molecules. Similar behavior has been seen in [Zwi05b] for the lifetime of a vortex lattice. Note that Ref. [Zwi05b] also reported a decrease in the lifetime in a narrow region around $1/k_F a = 0$, which we do not observe for our trap parameters.

In summary the hydrodynamic behavior in the crossover region leads to a very long lifetime of L_z.

2.5 Conclusion

In this work we have presented measurements on a strongly interacting Fermi gas carrying angular momentum. The angular momentum of the gas exhibits long lifetimes due to the deeply hydrodynamic behavior of the normal state in such a system. We investigated the decay rate of the angular momentum depending on the ellipticity of the trapping potential for two different temperatures. We find that the experimental results are in good agreement with the expected behavior for a simple Boltzmann gas. The dependence of the decay rate of the angular momentum on the interaction strength in the BEC-BCS crossover region confirms that the collective motion is very stable as long as the interaction strength is sufficiently large.

The long lifetime of the angular momentum in a rotating strongly interacting Fermi gas allows us to further investigate rotational properties both in the superfluid and normal phase in detail and with high precision. Currently we investigate the moment of inertia of the gas for different temperatures; see Chapter 3.

Acknowledgments
We acknowledge support by the Austrian Science Fund (FWF) within SFB 15 (project part 21) and SFB 40 (project part 4).

2.6 Appendices

Appendix A

To calculate the precession angle and the oscillation of the width we assume that the frequency and damping rate for the $m = \pm 2$ excitations are independent. For the damping of each excitation we assume an exponential behavior. A superposition of the two excitations results in the fit function for the precession angle [Bre03]

$$\tan\left(2(\phi-\phi_e)\right) = \frac{e^{-(\Gamma_+-\Gamma_-)t}\sin\left(\omega_+ t+2\phi_0\right)-\sin\left(\omega_- t+2\phi_0\right)}{e^{-(\Gamma_+-\Gamma_-)t}\cos\left(\omega_+ t+2\phi_0\right)+\cos\left(\omega_- t+2\phi_0\right)} \tag{2.2}$$

Here $\omega_\pm$ are the frequencies, $\Gamma_\pm$ are the damping rates, ϕ_0 is the initial angle for the two excitations and ϕ_e is the precession angle resulting from the expansion of the cloud. For the oscillation of the width difference ΔW we get

$$\begin{aligned}\Delta W^2 &= 4Ae^{-(\Gamma_++\Gamma_-)t}\cos^2\left(\frac{(\omega_+ + \omega_-)}{2}t+2\phi_0\right)\\ &+ A(e^{-\Gamma_+ t}-e^{-\Gamma_- t})^2,\end{aligned} \tag{2.3}$$

where A is the amplitude of the oscillation.

Appendix B

Here we calculate the effect of the expansion of the cloud on the precession angle. Assuming conservation of angular momentum during the expansion, the rotation frequency Ω of the gas decreases as the size of the cloud is increasing. We introduce an effective precession time t_e which accounts for the changing precession angle ϕ during expansion. The total change in the precession angle resulting from the expansion is given by

$$\phi_e = \int_0^{t_{\mathrm{TOF}}} \dot\phi(t)dt = \dot\phi(0)t_e, \tag{2.4}$$

where $\dot\phi(0)$ is the precession frequency when the gas is still trapped and t_{TOF} is the expansion time. Assuming that also during the expansion $\dot\phi(t) = L_z/(2Mr^2_{\mathrm{rms}}(t))$ is still valid and inserting this into Eq. 2.4 we get

$$t_e = \int_0^{t_{\mathrm{TOF}}} r^2_{\mathrm{rms}}(0)/r^2_{\mathrm{rms}}(t)dt. \tag{2.5}$$

To calculate the relative increase of the cloud size during expansion, $r^2_{\mathrm{rms}}(t)/r^2_{\mathrm{rms}}(0)$, we use the scaling approach; see e.g. [Alt07b]. For our experimental parameters, $\omega_r = 800\,\mathrm{Hz}$ and $t_{\mathrm{TOF}} = 0.8\,\mathrm{ms}$, we get an effective precession time of $t_e = 0.26\,\mathrm{ms}$. This is shorter than the typical precession time in the trap of $0.75\,\mathrm{ms}$.

CHAPTER 3

PUBLICATION

Quenching of the moment of inertia in a strongly interacting Fermi gas [1]

New J. Phys. **13**, 035003 (2011).

S. Riedl,[1,2] E. R. Sánchez Guajardo,[1,2] C. Kohstall,[1,2] J. Hecker Denschlag,[1] and R. Grimm[1,2]

[1] *Institut für Experimentalphysik und Zentrum für Quantenphysik, Universität Innsbruck, 6020 Innsbruck, Austria*

[2] *Institut für Quantenoptik und Quanteninformation, Österreichische Akademie der Wissenschaften, 6020 Innsbruck, Austria*

We report on the observation of a quenched moment of inertia as resulting from superfluidity in a strongly interacting Fermi gas. Our method is based on setting the hydrodynamic gas in slow rotation and determining its angular momentum by detecting the precession of a radial quadrupole excitation. The measurements distinguish between the superfluid and collisional origins of hydrodynamic behavior, and show the phase transition.

3.1 Introduction

Superfluidity is a striking property of quantum fluids at very low temperatures. For bosonic systems, important examples are liquids and clusters of ^{4}He and atomic Bose-Einstein condensates. In fermionic systems, superfluidity is a more intricate phenomenon as it requires pairing of particles. Fermionic superfluidity is known to occur in atomic nuclei and ^{3}He liquids and it is also at the heart of superconductivity, thus being of great technological importance. Recent advances with ultracold Fermi gases have opened up unprecedented possi-

[1] The author of the present thesis acquired the data together with S.R. and contributed to the analysis and interpretation of the results.

bilities to study the properties of strongly interacting fermionic superfluids [Gio08, Ing08a]. Early experiments on ultracold Fermi gases with resonant interparticle interactions compiled increasing evidence for superfluidity [O'H02, Reg04, Kin04a, Bar04a, Chi04, Kin05b] until the phenomenon was firmly established by the observation of vortex lattices [Zwi05b].

Here we report on the manifestation of superfluidity in a quenched moment of inertia (MOI) in a strongly interacting Fermi gas that undergoes slow rotation. The basic idea of a quenched MOI as a signature of superfluidity dates back to more than 50 years ago in nuclear physics, where MOIs below the classical, rigid-body value were attributed to superfluidity [Rin80]. The quenching of the MOI was also shown in liquid ^{4}He [Hes67] and has, more recently, served for the discovery of a possible supersolid phase [Kim04]. Here we introduce the observation of the quenched MOI as a new method to study superfluidity in ultracold Fermi gases.

3.2 Basic idea of the measurement

The basic situation that underlies our experiments is illustrated in Fig. 3.1. At a finite temperature below the critical temperature T_c, the harmonically trapped cloud consists of a superfluid core centered in a collisionally hydrodynamic cloud. We assume that the trapping potential is close to cylindrical symmetry, but with a slight, controllable deformation that rotates around the corresponding axis with an angular velocity Ω_{trap}. The nonsuperfluid part of the cloud is then subject to friction with the trap and follows its rotation with an angular velocity Ω[2], which in a steady state ideally reaches $\Omega = \Omega_{\text{trap}}$. The corresponding angular momentum can be expressed as $L = \Theta\Omega$, where Θ denotes the MOI. The superfluid core cannot carry angular momentum, assuming that vortex nucleation is avoided, and therefore does not contribute to the MOI of the system. Thus Θ represents the MOI of the whole system.

The case of a rotating system in a steady state, where the normal part carries the maximum possible angular momentum, allows us to distinguish the superfluid quenching of the MOI from a non-equilibrium quenching effect as studied in Ref. [Cla07]. There the authors investigated the hydrodynamic expansion of a gas with a known angular momentum. This situation, where the velocity fields of the normal and superfluid components are not in a steady state, can also be discussed in terms of a MOI below the rigid-body value. In contrast to the phenomenon investigated in our present work, the effect of Ref. [Cla07] is related to irrotational flow and can occur for both the superfluid and the collisionally hydrodynamic normal phase.

Our measurements rely on the possibility to determine the total angular momentum L of a rotating hydrodynamic cloud by detecting the precession of a radial quadrupole excitation. This method is well established and has been extensively used in the context of atomic Bose-Einstein condensates [Che00, Hal01a, Lea02]. We have recently applied it to a rotating, strongly interacting Fermi gas to investigate the slow decay of angular momentum [Rie09].

[2] We assume that the normal cloud performs a rigid rotation with an angular velocity Ω. This can be justified by the internal friction in the non-superfluid component along with the fact that the rotating trap deformation is applied to all regions of the cloud simultaneously.

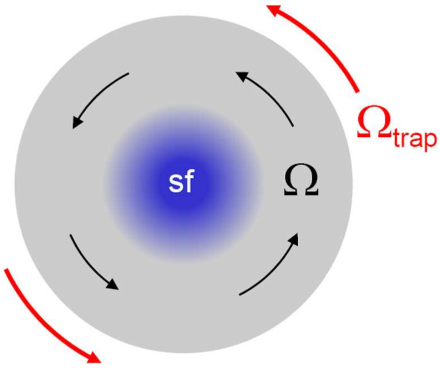

Figure 3.1: Schematic illustration of a strongly interacting Fermi gas in a slowly rotating trap. The normal part rotates with a frequency Ω, which in an equilibrium state approaches the rotation frequency Ω_{trap} that is imposed by the trap. The superfluid core (sf) does not carry angular momentum and therefore does not contribute to the MOI.

The method works under the general condition that the gas behaves hydrodynamically. Then the precession frequency can be written as $\Omega_{\text{prec}} = L/(2\Theta_{\text{rig}})$ [Zam98], where Θ_{rig} corresponds to a moment of inertia as calculated from the density distribution under the assumption that the whole cloud, including the superfluid part, would perform a rigid rotation. Substituting $\Theta\Omega$ for L, we obtain $\Omega_{\text{prec}} = \Theta/(2\Theta_{\text{rig}})\,\Omega$, with $\Theta/\Theta_{\text{rig}} = 1$ for the full MOI in a normal system, and $\Theta/\Theta_{\text{rig}} < 1$ for a MOI that is quenched because of the superfluid core.

3.3 Experimental setup and procedures

The starting point of our experiments is an optically trapped, strongly interacting Fermi gas consisting of an equal mixture of ^{6}Li atoms in the lowest two atomic states [Joc03b, Alt07b]. The broad 834-G Feshbach resonance [Ing08a] allows us to control the s-wave interaction. If not otherwise stated, the measurements presented here refer to the resonance center. Here a unitarity-limited Fermi gas [Gio08, Ing08a] is realized, which is known to exhibit deep hydrodynamic behavior even well above the critical temperature for superfluidity, see e.g. [Wri07]. The cigar-shaped quantum gas is confined in a far red-detuned, single-beam optical dipole trap with additional axial magnetic confinement. The trap can be well approximated by a harmonic potential with radial oscillation frequencies $\omega_x = \omega_y \approx 2\pi \times 680\,\text{Hz}$ and an axial frequency of $\omega_z = 2\pi \times 24\,\text{Hz}$. The Fermi energy of the noninteracting gas is given by $E_F = \hbar(3N\omega_x\omega_y\omega_z)^{1/3}$, where $N = 6\times10^5$ is the total atom number. The Fermi temperature is $T_F = E_F/k = 1.3\,\mu\text{K}$, with k denoting the Boltzmann constant.

Our scheme to study the rotational properties is described in detail in Ref. [Rie09]. It is based on a rotating elliptical deformation of the trap, characterized by a small ellipticity parameter [Rie09] $\epsilon' = 0.1$. In contrast to our previous work, we use a lower rotation frequency of $\Omega_{\text{trap}} = 2\pi \times 200\,\text{Hz} \approx 0.3\,\omega_x$. This low value allows us to avoid a resonant quadrupole mode excitation, which is known as an efficient mechanism for vortex nucleation [Mad01, Hod02]. To excite the quadrupole mode [Alt07b] we switch on an elliptic trap deformation for 50 μs. We detect the resulting oscillation by taking absorption images of the cloud after a variable hold time in the trap and a short free expansion time after release from the trap. More details on this excitation and detection scheme are given in Ref. [Rie09].

At this point it is important to discuss the consequences of residual trap imperfections, still present when we attempt to realize a cylindrically symmetric optical potential. As we showed in previous work [Rie09], we can control the ellipticity down to a level of ∼1%. Moreover, deviations from perfect cylindrical symmetry may occur because of other residual effects, such as corrugations of the optical trapping potential. As a consequence, a certain rotational damping is unavoidable, but damping times can reach typically one second [Rie09]. This has two main effects for our observations. First, our measurements yield precession frequencies slightly below Ω_{prec}. This is because of a delay time of 20 ms between turning off the rotating trap ellipticity and applying the quadrupole mode excitation. It is introduced to make sure that any possible collective excitation resulting from the rotating trap has damped out when the mode precession is measured. Because of rotational damping during this delay time, the measured precession frequencies Ω'_{prec} are somewhat below Ω_{prec}. To compensate for this effect, we directly measure the reduction of Ω_{prec} that occurs during a 20 ms hold time to determine the corresponding damping parameter $\kappa = \Omega'_{\mathrm{prec}}/\Omega_{\mathrm{prec}}$ for each set of measurements, finding day-to-day variations with typical values between 0.85 and 0.9. The second effect is induced by friction with static (nonrotating) trap imperfections when the rotating ellipticity is applied. This leads to equilibrium values for Ω typically a few percent below Ω_{trap}, depending on the ratio between the time constants for spin up and damping [GO00]. For this second effect there is no straightforward compensation, and it needs to be explicitly discussed when interpreting the experimental results.

Thermometry is performed after the whole experimental sequence. We damp out the rotation by stopping the trap rotation and keeping the ellipticity[3]. We convert the gas into a weakly interacting one by a slow magnetic field ramp to 1132 G, and we finally measure the temperature $\mathcal{T}$ [Rie09]. Note that the isentropic conversion tends to decrease the temperature such that $\mathcal{T}$ is always somewhat below the temperature T at unitarity [Che05a]. The relative statistical uncertainty of the temperature measurement is about 5% in the relevant temperature range.

3.4 Experimental results

To discuss our experimental results we introduce a dimensionless precession parameter $\mathcal{P}$ by normalizing our observable Ω_{prec} to its maximum possible value of $\Omega_{\mathrm{trap}}/2$,

$$\mathcal{P} = 2\,\frac{\Omega_{\mathrm{prec}}}{\Omega_{\mathrm{trap}}} = \frac{\Theta}{\Theta_{\mathrm{rig}}} \times \frac{\Omega}{\Omega_{\mathrm{trap}}}\,. \tag{3.1}$$

The maximum possible value of $\mathcal{P} = 1$ corresponds to a fully rotating, classically hydrodynamic cloud. Values $\mathcal{P} < 1$ show the presence of at least one of the two effects, namely the incomplete rotation of the normal part ($\Omega/\Omega_{\mathrm{trap}} < 1$) or the superfluid quenching of the

[3] The temperature increase resulting from conversion of rotational energy into heat is negligibly small.

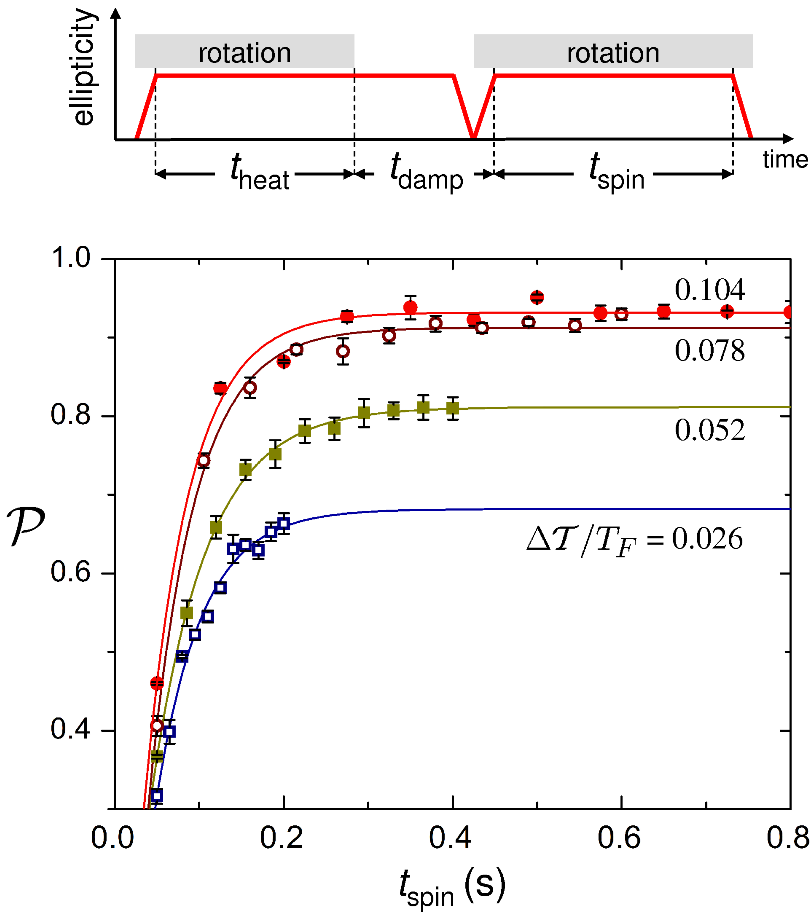

Figure 3.2: Precession parameter $\mathcal{P}$ versus spin-up time t_{spin} for various values of the final temperature, as characterized by the heating parameter $\Delta\mathcal{T}$ (see text). The quenching of the MOI shows up in the temperature-dependent saturation behavior. The applied timing sequence to facilitate measurements at constant temperature is illustrated above the graph. For these sets of measurements $\kappa = 0.85$.

MOI ($\Theta/\Theta_{\mathrm{rig}} < 1$). It is crucial for the interpretation of our experimental results to distinguish between these two effects. Our basic idea to achieve this relies on the fact that $\Theta/\Theta_{\mathrm{rig}}$ represents a temperature-dependent *equilibrium* property, whereas $\Omega/\Omega_{\mathrm{trap}}$ depends on the dynamics of the spin-up before the system has reached an equilibrium. Experimentally, however, measurements of equilibrium properties at a fixed temperature are not straightforward because of the presence of residual heating leading to a slow, steady temperature increase. In the rotating trap we always observe some heating, which under all our experimental conditions can be well described by a constant rate $\alpha = 170\,\mathrm{nK/s} = 0.13\,T_F/\mathrm{s}$[4].

[4]To determine the temparature increase in the rotating trap we measure $\mathcal{T}$ after variable rotation times. We find that, in the relevant temperature range, the behavior of $\mathcal{T}$ is well approximated by a linear increase with time. This justifies the description in terms of a constant heating rate.

3.4.1 Equilibrium state of rotation

To identify the conditions under which our cloud reaches its equilibrium state of rotation, we have developed a special procedure based on the timing scheme illustrated on top of Fig. 3.2. Our procedure takes advantage of the constant heating rate α to control the final temperature of the gas when $\mathcal{P}$ is measured. We apply the trap rotation in two separate stages of duration $t_{\rm heat}$ and $t_{\rm spin}$. In an intermediate time interval of $t_{\rm damp} = 200\,\rm ms$[5] we damp out the rotation that is induced by the first stage. The angular momentum disappears, but the heating effect remains[6]. The second stage spins up the cloud again and induces further heating. When $t_{\rm tot} = t_{\rm heat} + t_{\rm spin}$ is kept constant, we find that the total heating by the two rotation stages is $\Delta\mathcal{T} = \alpha\, t_{\rm tot}$. As only the second stage leads to a final angular momentum, the equilibrium state reached at a constant temperature can be identified when $\mathcal{P}(t_{\rm spin})$ reaches a constant value for increasing $t_{\rm spin}$ and fixed $t_{\rm tot}$. The temperature can be controlled by a variation of the parameter $t_{\rm tot}$ and is obtained as $\mathcal{T} = \mathcal{T}_0 + \Delta\mathcal{T}$. The temperature offset $\mathcal{T}_0$ is set by the initial cooling and some unavoidable heating during the experimental sequence without trap rotation. Under our conditions $\mathcal{T}_0 \approx 0.11\,T_F$.

Our experimental results for $\mathcal{P}(t_{\rm spin})$ are shown in Fig. 3.2 for four different values of the heating parameter $\Delta\mathcal{T}/T_F$ in a range between 0.026 to 0.104, which corresponds to a range of $\mathcal{T}$ between about 0.14 and 0.21 T_F. All four curves show qualitatively the same behavior. Within a few 100 ms, $\mathcal{P}$ rises before reaching a final equilibrium value. This time-dependent increase of $\mathcal{P}$ is related to the spin-up dynamics[7]. We find that the observed increase and saturation of $\mathcal{P}(t_{\rm spin})$ can be well fit by simple exponential curves (solid lines), and we use these fits to extract the different equilibrium values $\mathcal{P}_{\rm eq}$.

The equilibrium values $\mathcal{P}_{\rm eq}$ exhibit an interesting temperature dependence. The lower three values show a pronounced increase with temperature, $\mathcal{P}_{\rm eq} = 0.68$, 0.81, and 0.91 for $\Delta\mathcal{T}/T_F = 0.026$, 0.052, and 0.078, respectively. We interpret this increase as a consequence of the decreasing superfluid core and thus the decreasing MOI quenching effect. For our highest temperature ($\Delta\mathcal{T}/T_F = 0.104$) we only observe a marginal further increase to $\mathcal{P}_{\rm eq} = 0.93$. This indicates that the superfluid core is very small or absent leading to a disappearance of the quenching effect. The fact that the maximum $\mathcal{P}_{\rm eq}$ stays a few percent below 1 can be explained by trap imperfections as discussed in Sec. 3.3.

Let us comment on the possible influence of vortices [Zwi05b]. We cannot exclude their presence[8], as their nucleation can proceed not only via a resonant quadrupole mode excitation [Mad01, Hod02], but also via a coupling to the thermal cloud [Hal01b]. Vortices would result in additional angular momentum in the rotating cloud and its collective behavior would be closer to the normal case. This would tend to increase $\mathcal{P}$ at lower temperatures, counteracting the behavior that we observe.

---

[5] The ellipticity is kept at its full level while the rotation is turned off. To speed up the damping we increase the magnetic field to 920G.

[6] The temperature increase resulting from conversion of rotational energy into heat is negligibly small.

[7] The curves do not show the spin-up process directly, as our measurement procedure fixes the temperature at the time of the measurement of $\mathcal{P}$.

[8] In our setup we cannot directly observe vortices by absorption imaging. The main reason is the technical limitation that our coil system does not allow for fast enough magnetic field ramps as required for increasing the size of vortex cores during expansion [Zwi05b].

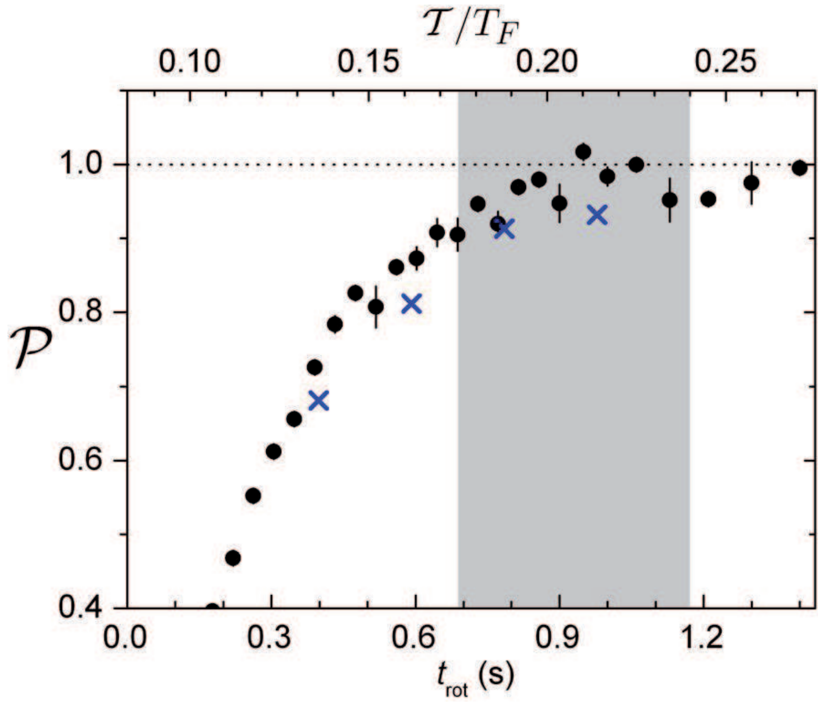

Figure 3.3: The precession parameter $\mathcal{P}$ as a function of the rotation time t_{rot} (filled symbols); the upper scale shows the corresponding temperature $\mathcal{T}$. For comparison, the crosses show the equilibrium values $\mathcal{P}_{\mathrm{eq}}$ as obtained from Fig. 3.2. The shaded region indicates the range in which we expect the superfluid phase transition according to previous experiments [Reg04, Luo07, Ina08, Luo09, Nas10, Hor10]. For this set of measurements $\kappa = 0.90$.

3.4.2 Superfluid phase transition

In a second set of experiments, we study the superfluid phase transition in a way which is experimentally simpler, but which requires information on the equilibrium state as obtained from the measurements presented before. The trap rotation is applied continuously, and we observe the increase of $\mathcal{P}$ with the rotation time t_{rot}. All other parameters and procedures are essentially the same as in the measurements before. Here the temperature is not constant, but rises according to $\mathcal{T} = \mathcal{T}_0 + \alpha t_{\mathrm{rot}}$, where the heating rate $\alpha = 170\,\mathrm{nK/s}$ is the same as before and $\mathcal{T}_0 = 0.085 T_F$ is somewhat lower because of the less complex timing sequence.

Figure 3.3 shows how $\mathcal{P}$ increases with the rotation time t_{rot} (filled symbols); the upper scale shows the corresponding temperature $\mathcal{T}$. The observed increase of $\mathcal{P}$ generally results from both factors in Eq.(3.1), corresponding to the rising $\Omega/\Omega_{\mathrm{trap}}$ (spin-up dynamics) and the rising $\Theta/\Theta_{\mathrm{rig}}$ (decrease of the superfluid MOI quenching). Figure 3.3 also shows the values $\mathcal{P}_{\mathrm{eq}}$ as determined from Fig. 3.2 (crosses), for which we know that the spin-up of the normal component has established an equilibrium with $\Omega/\Omega_{\mathrm{trap}}$ being close to one. The comparison shows that already for $t_{\mathrm{rot}} = 0.4\,\mathrm{s}$ the data set obtained with the simpler procedure follows essentially the same behavior. The small quantitative difference that the crosses are slightly below the open symbols can be explained by a somewhat stronger influence of trap imperfections in the earlier measurements of Sec. 3.4.1[9] or by the uncertainty in the initial temperature $\mathcal{T}_0$. For $t_{\rm rot} \geq 0.4\,$s, we can assume that the system is in an equilibrium state, which follows the slowly increasing temperature, and we can fully attribute the further increase of $\mathcal{P}$ to the quenching of the MOI.

The superfluid phase transition corresponds to the point where the precession parameter $\mathcal{P}$ reaches its saturation value. This is observed for a time $t_{\rm rot} \approx 0.95\,$s, when $\mathcal{T}/T_F \approx 0.21$. The conversion of this temperature parameter (measured in the weakly interacting regime after an isentropic change) to the actual temperature in the unitarity-limit regime [Luo09] yields a value for the critical temperature T_c of about $0.2\,T_F$. This result is consistent with previous experimental results [Reg04, Luo07, Ina08, Luo09, Hor10, Nas10], the range of which is indicated by the shaded region in Fig. 3.3. The result is also consistent with theoretical predictions [Gio08, Hau08].

For a more precise extraction of T_c from experimental MOI quenching data, a theoretical model would be required that describes the saturation behavior of $\Theta/\Theta_{\rm rig}$ as T_c is approached. Theoretical predictions are available for the BEC limit [Str96] and the BCS limit [Far00, Urb03, Urb05]. In the unitarity limit it should, in principle, be possible to extract the MOI from spatial profiles of the normal and the superfluid fraction [Per04, Sta05]. Clearly, more work is necessary to quantitatively understand the quenching effect in the strongly interacting regime.

3.5 Conclusion

We have demonstrated the quenching of the moment of inertia that occurs in a slowly rotating, strongly interacting Fermi gas as a consequence of superfluidity. This effect provides us with a novel probe for the system as, in contrast to other common methods such as expansion measurements and studies of collective modes, it allows us to distinguish between the two possible origins of hydrodynamic behavior, namely collisions in a normal phase and superfluidity.

Acknowledgments

We thank L. Sidorenkov and M. K. Tey for discussions. We acknowledge support by the Austrian Science Fund (FWF) within SFB 15 (project part 21) and SFB 40 (project part 4).

[9]This explanation is supported by the fact that we measured a slower decay of angular momentum for the later experiments of Fig. 3.3 ($\kappa = 0.90$) than we did for the earlier measurements of Fig. 3.2 ($\kappa = 0.85$). Between the two sets of measurements the optical setup of the trapping beam was readjusted, leading to reduced imperfections in the later experiments.

CHAPTER 4

PUBLICATION

Observation of interference between two molecular Bose-Einstein condensates [1]

New J. Phys. **13**, 065027 (2011).

C. Kohstall,[1,2] S. Riedl,[1,2] E. R. Sánchez Guajardo,[1,2] L. A. Sidorenkov,[1,2] J. Hecker Denschlag,[1] and R. Grimm[1,2]

[1] *Institut für Experimentalphysik und Zentrum für Quantenphysik, Universität Innsbruck, 6020 Innsbruck, Austria*

[2] *Institut für Quantenoptik und Quanteninformation, Österreichische Akademie der Wissenschaften, 6020 Innsbruck, Austria*

We have observed interference between two Bose-Einstein condensates of weakly bound Feshbach molecules of fermionic ^{6}Li atoms. Two condensates are prepared in a double-well trap and, after release from this trap, overlap in expansion. We detect a clear interference pattern that unambiguously demonstrates the de Broglie wavelength of molecules. We verify that only the condensate fraction shows interference. For increasing interaction strength, the pattern vanishes because elastic collisions during overlap remove particles from the condensate wavefunction. For strong interaction the condensates do not penetrate each other as they collide hydrodynamically.

4.1 Introduction

Interference manifests the wave nature of matter. The concept of matter waves was proposed by de Broglie in 1923 [Bro23] and now represents a cornerstone of quantum physics. Already in the 1920's, experiments demonstrated the diffraction of electrons [Dav27] and of atoms and

[1] The author of the present thesis developed the experimental procedure, performed the measurements, and analyzed the data supported by S.R., E.S. and L.S.

molecules [Est30]. These early achievements led to the field of atom optics and interferometry [Ada94, Bon04, Cro09].

With the realization of Bose-Einstein condensates (BECs) [And95, Dav95, Bra95], sources of macroscopically coherent matter waves became available. The interference between two BECs was first observed by Andrews et al. [And97]. This landmark experiment evidenced interference between two independent sources and revealed the relative phase between them [Cas97]. Since then, interference measurements have developed into an indispensable tool for research on BEC. Applications include detection of the phase of a condensate in expansion [Sim00], investigation of a condensate with vortices [Ino01], and studies of quasi-condensates [Had06] or Luttinger liquids [Hof07] in reduced dimensions. Another fundamental line of research in matter-wave optics is to explore the transition from the quantum to the classical world by detecting the wave nature of progressively larger particles, like clusters [Sch94], C_{60} [Arn99], and other giant molecules [Ger11].

The creation of molecular Bose-Einstein condensates (mBECs) of paired fermionic atoms [Joc03b, Gre03, Zwi03b] provides us with macroscopically coherent molecular matter waves. In this article, we present the interference of two such mBECs and demonstrate interference as a tool to investigate condensates of atom pairs. This work extends the interference of condensates towards larger, composite particles.

In a Young-type interference experiment, we release two mBECs from a double-well trap and, after the condensates have overlapped, we observe an interference pattern by absorption imaging. In Sec. 4.2, we describe the experimental procedures in detail. In Sec. 4.3, we present our main experimental results, demonstrating the *molecular* de Broglie wavelength and the dependence of the interference contrast on temperature and interaction strength. Increasing the interaction strength reduces the visibility because of increasing elastic scattering losses depleting the coherent matter wave. Section 4.4 gives an outlook to possible extensions and applications of interference of pair condensates.

4.2 Experimental procedures

4.2.1 Preparation of the molecular Bose-Einstein condensate

We create a molecular Bose-Einstein condensate (mBEC), starting from an atomic Fermi gas consisting of an equal mixture of ^{6}Li in the lowest two spin states. The preparation follows the procedures described in our previous work [Joc03b, Bar04b, Alt07a, Rie08].

The atoms are trapped in the potential of a focused, far red-detuned laser beam with a beam waist of 45 μm, derived from a 25 W, 1030 nm single-mode laser source, as illustrated in Fig. 4.1. We choose the coordinate system such that the laser beam propagates along the z-axis and gravity acts in $-y$-direction. A magnetic bias field B can be applied along the y-axis. A broad Feshbach resonance centered at $B = 834$ G [Bar05] facilitates precise tuning of the atomic s-wave scattering length a. Below resonance, a weakly bound molecular state exists [Joc03a]. Molecules in this state represent halo dimers, since their wavefunction extends far into the classically forbidden range [Fer08]. Their size is given by a and their binding energy is $\hbar^2/(ma^2)$, where m denotes the atomic mass and $\hbar$ is Planck's constant h divided by 2π. The intermolecular scattering length is $a_M = 0.6a$ [Pet05b].

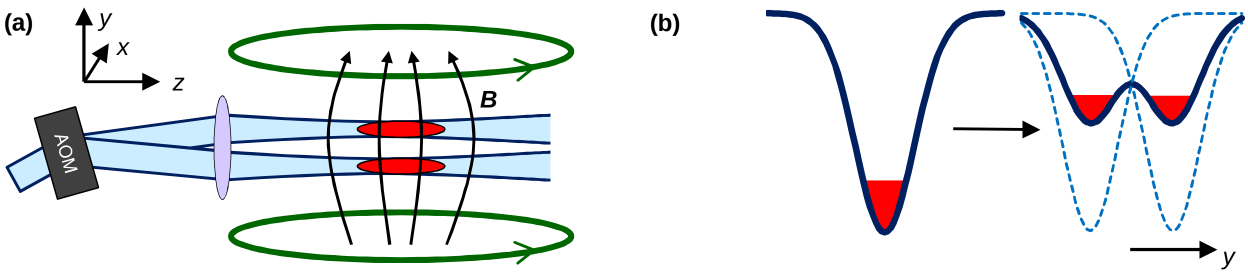

Figure 4.1: Illustration of the trapping and splitting of the mBEC in the presence of a magnetic field B. An acousto-optical modulator (AOM) toggles the laser beam between two positions, which creates an effective double-well potential for trapping two mBECs. (a) Along the x- and y-directions, the optical potential is dominant; along the z-axis the magnetic potential is dominant. (b) The potential shape of the optical dipole trap is Gaussian. The double-well potential is generated from the superposition of two Gaussian potentials.

To create the mBEC we perform evaporative cooling by reducing the laser beam power at a constant magnetic field $B = 764\,\mathrm{G}$. During evaporation, the halo dimers are created through three-body collisions [Joc03b] and eventually they form a mBEC [Ing08a]. After evaporation, we increase the trap depth, thereby compressing the condensate, to avoid spilling particles in all further steps of the experimental sequence. The beam power is adiabatically increased by a factor of about 10 to 45 mW. The trap center can be closely approximated by a harmonic potential. The oscillation frequencies of the molecules, which are the same as the ones of free atoms, are $(\omega_x, \omega_y, \omega_z) = 2\pi \times (250, 250, 20.6 \times \sqrt{B/700\,\mathrm{G}})\,\mathrm{Hz}$. The axial confinement essentially results from the curvature of the magnetic field. We obtain a cigar-shaped cloud containing $N = 1.8 \times 10^5$ molecules. The condensate fraction exceeds 90 % [Joc03b].

Most of our measurements are carried out in the regime of weak interaction between the molecules. We ramp the magnetic field adiabatically down to 700 G in 200 ms, thereby decreasing the scattering length to about $a_M = 1000\,\mathrm{a}_0$; at lower fields the molecules become unstable [Pet05a, Cub03, Joc03a] and limit the lifetime of the mBEC. At 700 G, the chemical potential of the mBEC is $k_B \times 200\,\mathrm{nK}$, with k_B denoting the Boltzmann constant, and the binding energy of the molecules is $k_B \times 8\,\mu\mathrm{K}$. In view of the crossover from BEC to a Bardeen-Cooper-Schrieffer (BCS) type regime [Gio08, Ing08a], one can also express the interaction conditions in terms of the commonly used dimensionless parameter $1/(k_F a)$, where k_F is the Fermi wave number of a non-interacting Fermi gas with $(\hbar k_F)^2/(2m) = E_F$, where $E_F = \hbar(6N\omega_x\omega_y\omega_z)^{1/3}$ is the Fermi energy. For the condition of our mBEC at 700 G we obtain $1/(k_F a) = 3$. Strongly interacting conditions are realized for $1/(k_F a) < 1$, which can be achieved at fields closer to resonance.

4.2.2 Condensate splitting

The mBEC is split into two equal parts along the y-axis. We transform the Gaussian shaped optical dipole potential into a double-well potential, as illustrated in Fig. 4.1(b).

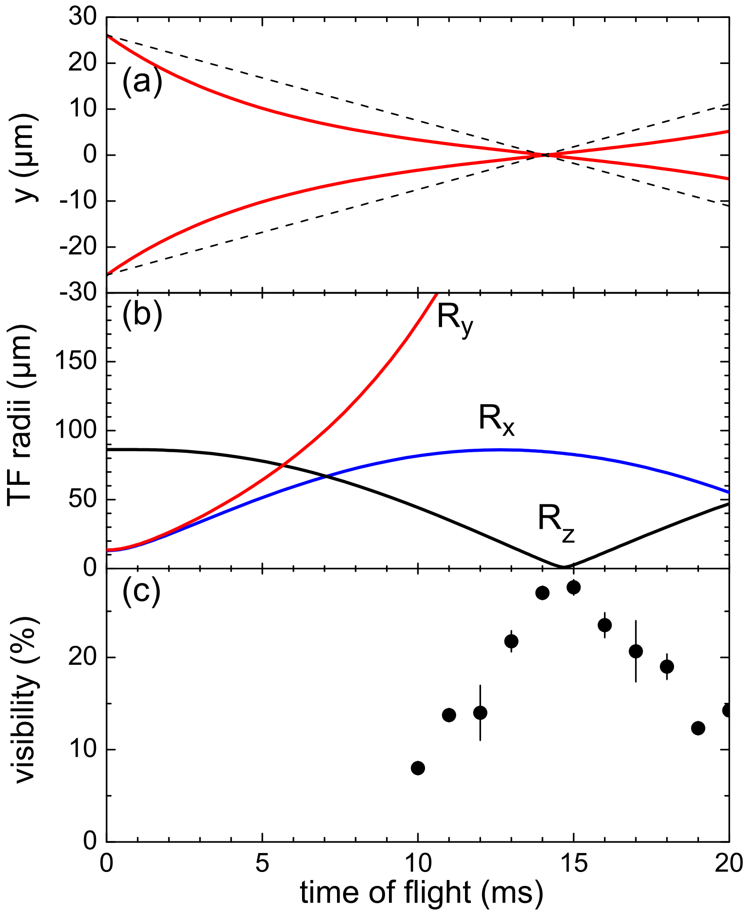

Figure 4.2: Expansion dynamics of the condensates in the magnetic saddle potential. (a) The solid lines are the calculated center-of-mass motion of the condensates, taking into account an initial kick towards each other, see text. The trajectories intersect after $t_{\mathrm{TOF}} = 14\,\mathrm{ms}$. For comparison, the dashed lines represent the trajectories of particles in free expansion intersecting at the same point. (b) The calculated Thomas-Fermi radii of the condensates show the expansion along the x- and y-axis and the compression along the z-axis. The initially cigar-shaped mBEC evolves into a flat disc. (c) The measured visibility of the fringe pattern shows a clear peak, which coincides with the minimum in R_z. The bars indicate the statistical uncertainties derived from 10 individual measurements.

This is accomplished by using time-averaged potentials. An acousto-optical deflection system modulates the trapping beam position so fast that the atoms do not follow and feel the time-averaged beam intensity as their motional potential [Alt07b, Shi04]. The modulation frequency is 200 kHz and the trapping beam is toggled between two positions, the distance of which is increased from 0 to 68 μm within 50 ms. The distance between the minima of the resulting double well is somewhat smaller because the two Gaussian potentials still overlap. The measured distance between the centers of the two condensates is $s = 56\,\mu$m and the measured oscillation frequencies in each well are $(\omega_x, \omega_y, \omega_z) = 2\pi \times (164, 146, 20.6 \times \sqrt{B/700\,\mathrm{G}})$ Hz. The chemical potential of both condensates is $k_B \times 100$ nK and the interaction parameter is $1/(k_F a) = 4$. The barrier height is $k_B \times 160$ nK, which leads to a fully negligible tunneling rate. The number ratio between the two condensates after splitting is sensitive to imperfections of the optical potential. To control equal number splitting, we fine-tune the magnetic gradient field that is applied to compensate for the effect of gravity.

4.2.3 Expansion in the magnetic field

The specific expansion dynamics of the released mBECs in our setup is the key to making interference clearly observable, and the understanding of the expansion is essential for the interpretation of our results. We identify two effects, which result from the curvature of the magnetic field, that are favorable for the observation of interference.

The coils generating the magnetic offset field in our set-up are not in Helmholtz configuration, which leads to second-order terms in $B(x, y, z)$. The resulting magnetic potential is a saddle potential, where the molecules are trapped along the x- and z-directions, but they are anti-trapped along the y-axis, the symmetry axis of the field. The oscillation frequencies are $(\omega_x, \omega_y, \omega_z) = 2\pi \times (20.5, i \times 29, 20.5) \times \sqrt{B/700\,\mathrm{G}}$ Hz, where the imaginary frequency denotes the anti-trap along the y-axis.

We model the expansion by adopting the scaling approach as applied in Refs. [Men02, Alt07b]. Figure 4.2(b) shows the predicted evolution of the Thomas-Fermi (TF) radii R_x, R_y and R_z, which we also verify experimentally. At the beginning, the expansion is driven by the pressure gradient in the cloud, which leads to a fast acceleration in the radial direction. This expansion is then further accelerated along y and decelerated along x because of the magnetic saddle potential. Along the z-axis, the long axis of the trapped cloud, the trap remains basically unchanged when the cloud is released from the optical potential. As the mean field pressure of the expanding cloud decreases, the magnetic confinement leads to a spatial compression of the cloud. We find that after $t_{\mathrm{TOF}} \approx 14$ ms the parameter R_z has a minimum because of this compression effect.

For high interference contrast, large overlap of the two clouds at the time of detection is essential. To achieve this, the condensates are kicked towards each other by switching on the original single-well trap, typically for 0.1 ms right after release from the double well. The solid lines in Fig. 4.2(a) show the calculated center-of-mass motion of the clouds after the initial kick to assure large overlap at $t_{\mathrm{TOF}} \approx 14$ ms.

The interference pattern is determined by the relative velocity between the two condensates. The relative velocity v_{rel} at $y = 0$ and $t_{\mathrm{TOF}} = 14$ ms can be directly deduced from the slopes of the solid lines in Fig. 4.2(a). This velocity is substantially smaller than it

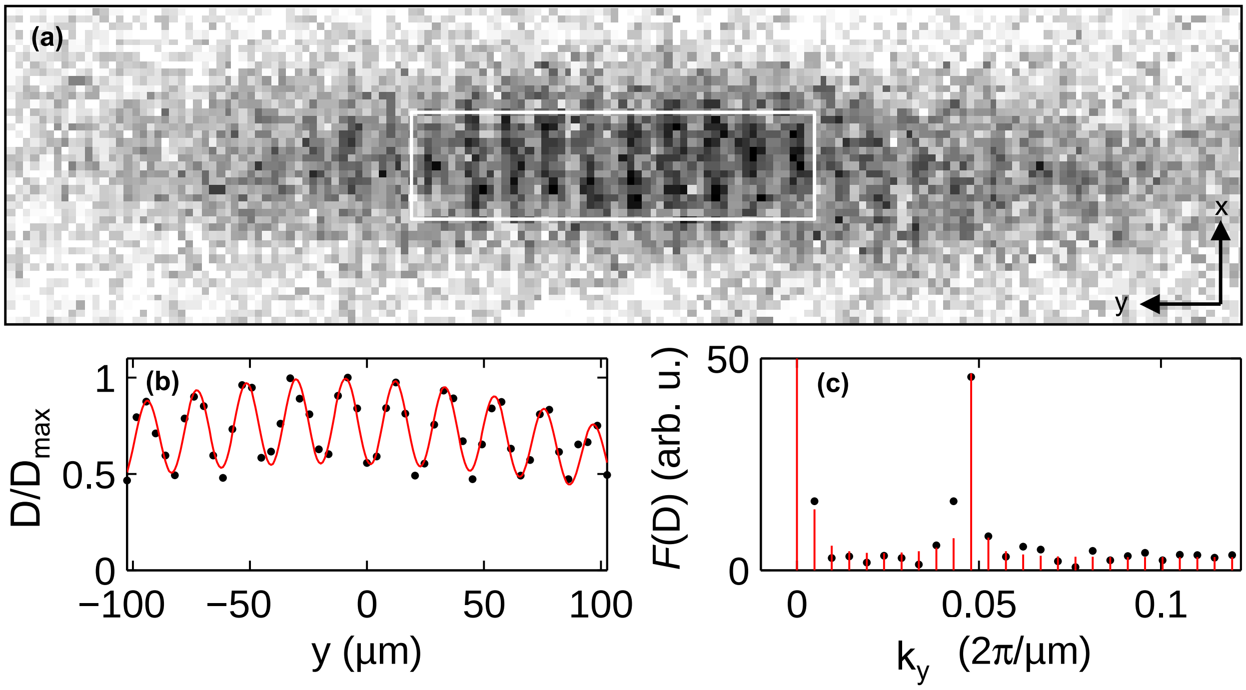

Figure 4.3: Interference image and analysis. (a) The column density along the z-axis after $t_{\mathrm{TOF}} = 14\,\mathrm{ms}$ shows the interference pattern. The field-of-view is $660\,\mu\mathrm{m}\times 170\,\mu\mathrm{m}$. The inner box indicates the region used for analysis. (b) The column density integrated along x gives the density distribution D along y (dots). The solid curve is the result of the fit in Fourier space, see text. (c) The density distribution is Fourier transformed (dots) and fitted (bars).

would be in free expansion without magnetic potential, where particles meeting at $y = 0$ and $t_{\mathrm{TOF}} = 14\,\mathrm{ms}$ would follow the dashed trajectories in Fig. 4.2(a). This deceleration of v_{rel} can be readily visualized by the condensates climbing up the potential hill resulting from the anti-trap in y-direction. This anti-trap also accelerates the expansion in y-direction, see R_y in Fig. 4.2(b). Remarkably, since the velocity field in each of the clouds stays linear, v_{rel} is independent of the position. More rigorously, we calculate v_{rel} using the scaling approach and taking into account the center-of-mass motion of the clouds.

Thus expansion dynamics brings about two favorable effects: First, the spatial compression along the z-axis facilitates clear detection of interference fringes by absorption imaging. Second, the decreased relative velocity leads to an increased fringe period. This means that the anti-trap acts as a magnifying glass for the interference fringes.

4.2.4 Detection and analysis of interference fringes

We detect the clouds by absorption imaging. Figure 4.3(a) shows a typical image of interference after 14 ms time of flight. The imaging beam propagates along the z-axis. It is overlapped with the trapping beam using dichroic mirrors. The imaging light pulse is on for

$10\,\mu$s and its intensity is about the saturation intensity of ^{6}Li atoms. We state-selectively image the atoms in the second-to-lowest Zeeman state. Already the first photon scattering event is likely to dissociate the weakly bound molecule [Bar04b], followed by about 10 more photons scattered by the free atom.

From the absorption images, we determine the visibility and fringe period of the interference pattern. The column density is integrated along the x-direction over the region depicted in Fig. 4.3(a) [2] resulting in a one-dimensional density distribution D, shown in Fig. 4.3(b). The density distribution contains various kinds of noise (e.g. photon or atom shot noise, or camera readout noise), which may be misinterpreted as interference signal. Therefore we analyze the density distribution in Fourier space by considering the Fourier transformed density distribution $\mathcal{F}(D)$, see Fig. 4.3(c). Here all those types of noise are approximately white and show up as a constant offset, whereas, the signal of interference is monochromatic and shows up as a peak. This gives the possibility to subtract the average contribution of noise from the signal. We determine the visibility and fringe period by the custom fit function in Fourier space

$$f = \sqrt{|\mathcal{F}((a + b\;y + c\;y^2) \times (1 + v\;\;\sin(2\pi/d\;y + \phi)))|^2 + n^2}, \tag{4.1}$$

yielding the fringe period d, the visibility v, and the relative phase ϕ. The term $a+b\,y+c\,y^2$ account for the somewhat non-uniform density distribution. The white noise n is the offset in Fourier space. Since the phase between the signal and the noise is random, the corresponding contributions are added quadratically. The discrimination of the noise via this fitting routine is crucial when the visibility is low.

The largest observed visibility is about 30 %. We find that this upper limit can be essentially attributed to the finite resolution of our imaging system. We determine the modulation transfer function of the imaging system and it gives about $30 \pm 10\,\%$ visibility for structures with period $d = 20\,\mu$m. Also other sources can contribute to a reduction of visibility, like a blurring because of a limited depth of focus or a tilt of the planes of constructive and destructive interference. The planes are in general somewhat tilted with respect to the line of sight, thereby obscuring the fringe pattern on the image. But these effects are suppressed by the spatial compression along the imaging axis caused by the magnetic saddle potential. This can be seen by comparing the compression of R_z in Fig. 4.2(b) to the detected visibility in Fig. 4.2(c). The minimum of R_z after $t_{\mathrm{TOF}} = 14\,$ms coincides with the peak in visibility. The peak value of almost 30 % agrees with the resolution limit of the imaging system. All following measurements are performed when the clouds are compressed to about $1\,\mu$m along the imaging axis; in this case, only the limited resolution is relevant. The spatial compression is an alternative to the slicing imaging technique used in Ref. [And97] and brings along the advantage that all particles are imaged.

4.3 Experimental results

The observed interference pattern is the standing wave formed by two macroscopically occupied matter waves, the two molecular BECs. Here we present our main experimental

[2] The size of the region was chosen to produce the optimal signal to noise.

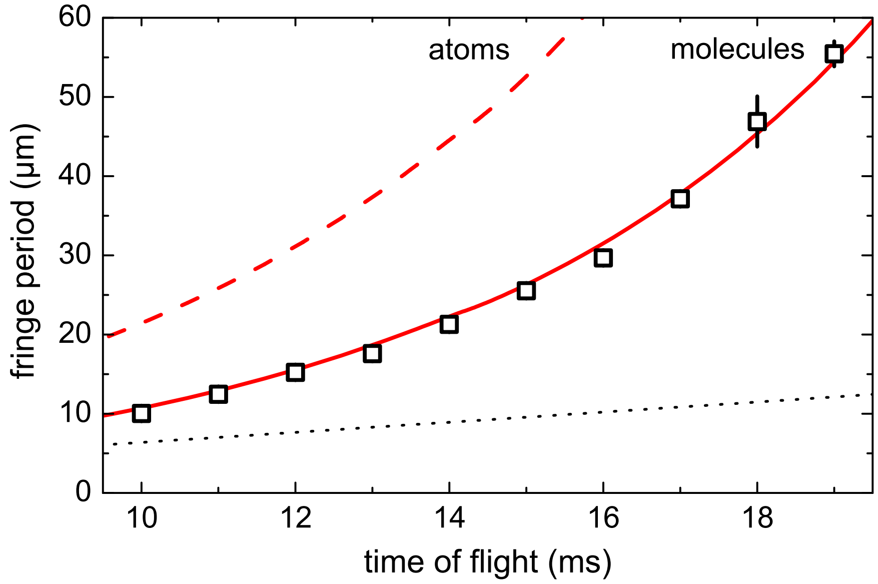

Figure 4.4: Fringe period as a function of time of flight. The symbols are the measured periods with bars, mostly smaller than the symbol size, indicating the statistical uncertainties resulting from 10 individual measurements at a given time of flight. The solid line is the calculated period for molecules and the dashed line for atoms. For free expansion without the magnetic saddle potential, the fringe period of molecules would be much smaller (dotted line).

results. In Sec. 4.3.1, we investigate the fringe period, which evidences that the interfering particles are molecules. In Sec. 4.3.2, we study the visibility when heating the cloud to above the critical temperature for condensation to show that the interference is established by the condensate fraction. In Sec. 4.3.3, we explore the dependence of the visibility on the interaction strength and find that non-forward scattering processes depopulate the momentum component of the matter wave that is responsible for the interference pattern.

4.3.1 Fringe period

The fringe period is an central observable in interference experiments. Figure 4.4 shows the measured fringe period at $B = 700\,\mathrm{G}$ as a function of time of flight. The de Broglie relation yields the fringe period

$$d = \frac{h}{M v_{\mathrm{rel}}}, \tag{4.2}$$

which is determined by the mass M of the interfering particles and by the relative velocity v_{rel} of the two condensates. In our experiment, we calculate v_{rel} from the expansion and center-of-mass motion of the condensates in the magnetic field curvature, as discussed in Sec. 4.2.3. The result is in contrast to the simple relation $v_{\mathrm{rel}} = s/t_{\mathrm{TOF}}$ that holds for the free expansion usually considered in experiments of this type. The solid line in Fig. 4.4 displays the calculated fringe period d for molecules, where we set $M = 2m$. All input parameters

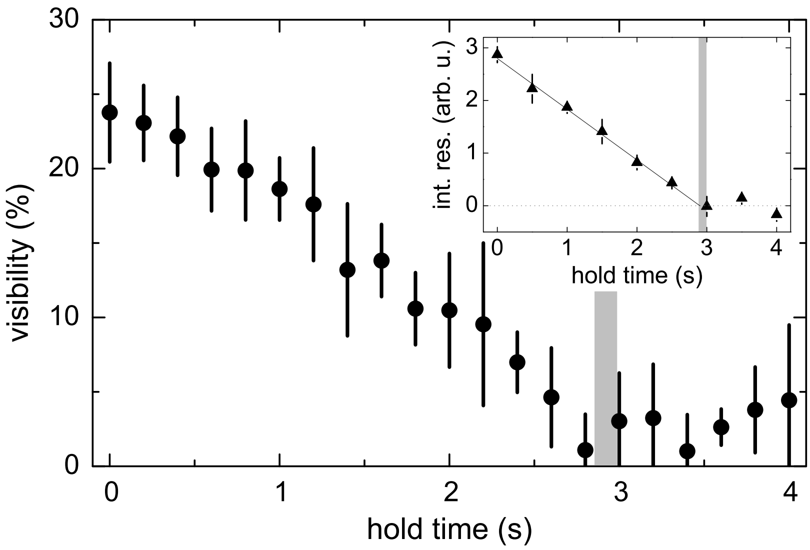

Figure 4.5: Visibility of interference for increasing temperature. The main figure shows the measured mean visibility with bars indicating the standard deviation resulting from 11 measurements. Here, we plot the standard deviation and not the statistical uncertainty to better illustrate the range of measured values. During the hold time in the trap, the temperature increases from low temperature to above T_c. The hold time after which T_c is reached is indicated by the grey bar. The inset shows the integrated residuals of a Gaussian fit, see text. A linear fit to the first six points facilitates a simple extrapolation to zero, which marks the vanishing of the condensate fraction.

for this calculation are determined independently. Their combined uncertainties result in typical uncertainty of 3 % for the fringe period, with the main contribution stemming from the uncertainty in the cloud separation. The data are in remarkable agreement with the calculation. For comparison, we also plot the fringe period for interfering atoms ($M = m$), which is clearly incompatible with the data.

The dotted line in Fig. 4.4 displays the fringe period that would result for freely expanding mBECs without the magnetic saddle potential. Comparing this curve to the much larger fringe period that we observe, highlights the effect of the magnetic field curvature to magnify the fringe period, as discussed in Sec. 4.2.3. The same magnification effect was reported in Ref. [Zaw10].

Note that the fringe period can be increased by interaction-induced slowing down of the two overlapping condensates [Sim00]. The mean-field of one condensate represents a potential hill for the other condensate, which slows down when climbing this hill. Under our experimental conditions at 700 G, the effect is found to be negligible. For stronger interaction, we see indications of this effect in agreement with a corresponding model calculations.

4.3.2 Dependence of interference visibility on condensate fraction

To demonstrate that the interference results only from the condensed molecules and not from the thermal fraction, we perform a controlled heating experiment and show the loss of visibility with vanishing condensate fraction. Starting from an almost pure condensate [Joc03b], we hold the gas in the recompressed optical dipole trap for a variable hold time before splitting. Intensity fluctuations and pointing instabilities of the laser beam as well as inelastic collisions between the molecules [Pet05a] heat the gas and lead to a monotonous temperature increase [Sav97, Wri07]. To demonstrate that the interference results from the condensate, it is sufficient to determine the hold time at which the critical temperature for condensation T_c is reached. Therefore, we fit a Gaussian profile to the density distribution of the cloud, which is recorded after expansion for $t_{\mathrm{TOF}} = 5\,\mathrm{ms}$ from the single-well trap. We find that the integrated residual of the fit gives a good measure whether the cloud shape deviates from a thermal one. The inset in Fig. 4.5 shows that the integrated residual goes to zero after a hold time slightly below 3 s, which locates the phase transition.

The visibility data in Fig. 4.5 are recorded at $B = 700\,\mathrm{G}$ after $t_{\mathrm{TOF}} = 14\,\mathrm{ms}$ [3]. The visibility decreases as the temperature increases and vanishes for a hold time that coincides with the hold time when T_c is reached. The observed decrease of visibility is continuous because we image the full column density including the growing thermal fraction, which does not clearly separate from the condensate in expansion at 700 G. Above T_c, the density distribution does no more show any fringes. Still, the fitting routine produces finite mean values because it can output only positive values. But if the measured visibility is not larger than the standard deviation, its distinction from zero is not significant. The vanishing visibility above the critical temperature confirms that, as expected, the interference is established by the condensate fraction.

Further intriguing evidence that the interference is caused by the condensate is the observation of interference between independent ultracold clouds. An independent production rules out that the interference can be caused by self interference of particles [Mil05]. To investigate interference between independent clouds, we split them already at a temperature far above the critical temperature to a large distance of 180 μm and then create two mBECs independently. Shortly before release, we reduce the distance to obtain the identical geometry as in all the other measurements and proceed as usual. We observe the same kind of interference pattern with a visibility of about 15 %. The lower visibility can be explained by a less efficient evaporation and less control over the equal number preparation in the double well.

4.3.3 Dependence of interference visibility on interaction strength

In a further set of measurements, we investigate how the fringe visibility depends on the interaction strength. Therefore we perform the interference experiment for different magnetic field values, thereby changing the molecular scattering length a_M according to the upper

[3] We verify on images after $t_{\mathrm{TOF}} = 0.4\,\mathrm{ms}$ that the clouds are still separated in the double-well potential despite the higher thermal energies.

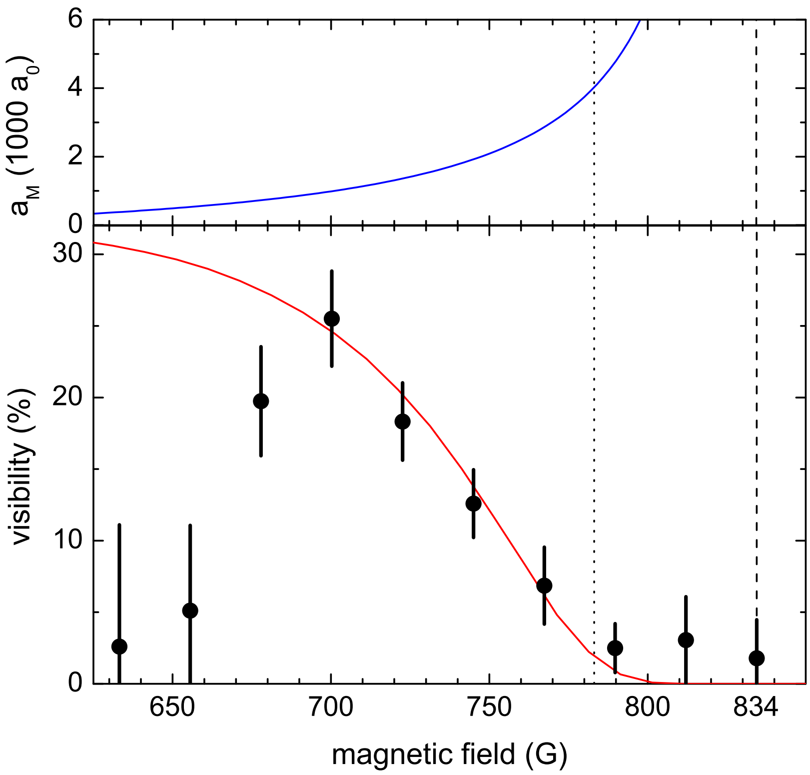

Figure 4.6: Visibility of interference from weak to strong interaction. The upper panel shows how the molecular scattering length a_M increases towards the Feshbach resonance at 834 G, marked by the dashed line. The onset of the strongly interacting regime is marked by the dotted line. In the lower panel, the dots represent the mean visibility with bars indicating the standard deviation resulting from 20 individual measurements. The solid line is the predicted visibility from the simple calculation modeling the non-forward scattering events.

panel of Fig. 4.6 [4]. The observed visibility as a function of the magnetic field is shown in the lower panel in Fig. 4.6. The highest visibility is found at about 700 G. For lower fields, the visibility is decreased, which we attribute to inelastic decay. The inelastic collisions of molecules lead to heating of the gas and loss of particles. The heating reduces the condensate fraction, which decreases the visibility as observed in the previous section. The loss also reduces the signal on the images. This leads to a higher statistical uncertainty in the determination of the visibility, showing up in the larger standard deviations below 700 G.

Towards larger interaction strength, our data show a pronounced decrease of visibility, and the visibility vanishes at about 780 G. This coincides with the onset of strong interaction in the trap, where $1/k_F a \approx 1$. We find that the main effect causing the decrease is elastic non-forward scattering. It is known from experimental and theoretical work on colliding condensates [Chi00, Ban00] that elastic non-forward scattering of particles removes them

[4] We verify on images after $t_{\mathrm{TOF}} = 0.4$ ms that the clouds are still separated in the double-well potential despite the higher chemical potential at higher interaction strength.

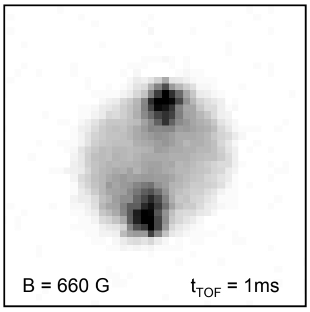

Figure 4.7: Absorption image 1 ms after the collision of two BECs. A spherical shell of scattered particles clearly separates from the two BECs. The field of view is $180 \times 180\,\mu$m.

from the condensate wavefunction. In contrast to the forward scattering accounted for within the usual mean-field approach, this non-forward scattering transfers particles into momentum states of random direction, which therefore do no more contribute to the observed interference pattern. Non-forward scattering is a particle-like excitation, which requires $v_{\rm rel}$ to exceed the speed of sound v_s. The process is suppressed for smaller $v_{\rm rel}$ [Chi00, Ban01]. To estimate the decrease of visibility through this process, we perform a simple model calculation. The velocity dependence of non-forward scattering is included by the following approximation: no suppression for $v_{\rm rel} \geq v_s$ and full suppression otherwise. We calculate the mean number of non-forward scattering events N_e for a representative molecule with molecules of the other condensate until the moment of detection. This representative molecule travels along the center-of-mass path of the condensate; see Fig. 4.2(a). We take the bosonically enhanced, unitarity limited scattering cross section $\sigma = 8\pi a_M^2/(1+(ka_M)^2)$, with $k = mv_{\rm rel}/\hbar$. From N_e, we derive the probability for a molecule to still be part of the condensate. This probability is e^{-N_e} and directly corresponds to the expected visibility, which we fit to the data, excluding the three data points below 700 G. We obtain the solid line in Fig. 4.6. The only fit parameter is a normalization factor, which allows us to account for the reduced detected visibility because of the limited imaging resolution. The fit yields a factor of 0.32, which is consistent with the imaging resolution discussed in Sec. 4.2.4. We find that our simple model for non-forward scattering can very well explain the decrease of visibility towards high interaction strength.

There are also other effects that decrease the visibility for increasing interaction strength, but they turn out to be minor for our experimental conditions: Strong interaction lead to a depletion of the condensate [Dal99]. Only the condensate contributes to the interference pattern and not the depleted fraction.The depleted fraction amounts to about 10 % at 780 G. As we expect the reduction of visibility to be proportional to the depletion, the reduction is negligible (at 780 G from 2.6 % to 2.3 %). Another effect reducing the visibility is the collisional dissociation of molecules during overlap. However, this effect can only occur above 800 G, where the collision energy exceeds the binding energy.

To directly demonstrate the effect of non-forward scattering, we study the collision of two condensates when their relative velocity $v_{\rm rel}$ is much faster than the their expansion velocity. This allows us to observe the non-forward scattered particles in an s-wave shell [Bug04],

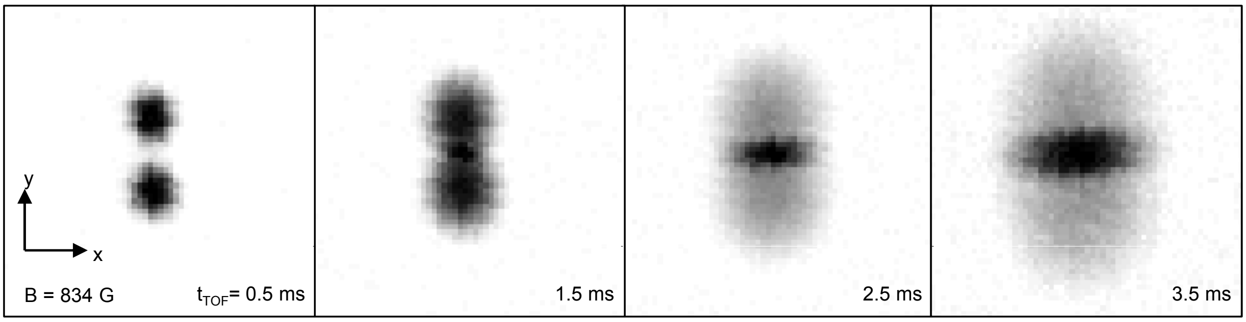

Figure 4.8: The hindered overlap on resonance. The series shows the first few milliseconds of expansion. The two clouds do not penetrate each other, but splash according to hydrodynamics. The field of view is $180 \times 180\,\mu$m.

well separated from the condensates, see Figure 4.7. This separation was not present in the interference experiments reported before because $v_{\rm rel}$ was similar to the expansion velocity. We apply our simple model to calculate the fraction of non-forward scattered particles and find good agreement, confirming our model in an independent and direct way.

Close to the Feshbach resonance, we enter a regime where the number of collisions becomes large. This leads to hydrodynamic behavior also above T_c [O'H02, Wri07]. The time of flight series in Fig. 4.8, taken on resonance, shows that the clouds do not penetrate each other in this regime. Instead, the flow of the particles is redirected into the the x-z-plane leading to the observed high column density in the center. Unlike at low magnetic fields, the clouds do not superimpose. This directly excludes interference of two independent condensates in the strongly interacting regime. The scenario is similar to the one in Ref. [Jos11] and may be described by the analysis therein.

The hindered overlap could be overcome by a magnetic field ramp to weak interaction after release and before overlapping, as done for the detection of vortices in Ref. [Zwi05b]. Like the observation of vortices, the observation of interference would evidence the coherence of the strongly interacting superfluids.

In further measurements, performed above the Feshbach resonance towards the BCS regime, we did not observe interference. To discuss possible reasons for the absence of interference fringes, let us first consider the effect of non-forward scattering on the visibility. As on the BEC side, this effect may hinder overlap and interference for $1/k_F a < -1$, i.e. below 910 G. However, we also have to consider that the pairs on the BCS side may not persist in expansion [Sch07], unlike on resonance or on the BEC side. For the lowest achievable temperature in our experiment and at 910 G, the pairs would be already unstable after a very short expansion time according to Ref. [Sch07].

4.4 Conclusion and outlook

In conclusion, we have observed the interference between two molecular BECs. The interference pattern visualizes the standing matter wave of the weakly bound Feshbach molecules and shows coherence over the spatial extension of the cloud. The contrast of interference vanishes above the critical temperature of condensation, demonstrating that the interference is established by the condensed molecules only. We find that non-forward elastic scattering processes can lead to a depletion of the condensate wavefunction while the clouds overlap. This effect increases towards higher interaction strength and prevents us from observing interference in the strongly interacting regime. On resonance we observe that the two clouds do not overlap but rather collide and deform as a result of deep hydrodynamic behavior.

Interference between condensates of paired fermionic atoms can serve as a powerful tool to investigate many exciting aspects of those systems. A future application will be given, for example, if p-wave condensates become available. Here, interference is predicted to reveal the vector nature of the order parameter [Zha07]. A conceptually interesting regime will be entered when the size of the pairs becomes comparable to the fringe period. Then the detected distribution of atoms may not reveal the interference pattern of the pair distribution. Besides investigating condensates of paired fermions themselves, the system could be used to study the fundamental processes of interference. The wide tunability of the interaction strength could be used to assist self-interference [Ced07] or to investigate to which extent interaction build up the observable relative phase [Xio06].

Suppressing the effect of non-forward scattering during overlap could extend the range of applications of condensate interference. Such a suppression may be achieved by reducing the interaction strength before overlap using fast magnetic field ramping techniques [Gre03, Zwi05b]. This technique would allow for investigating the interference in the regime of strong interaction or even on the BCS side of the resonance, where the interference of Cooper-type pairs is an intriguing question in itself.

Acknowledgments

We thank Christopher Gaul for stimulating discussions. We acknowledge support by the Austrian Science Fund (FWF) within SFB 15 (project part 21) and SFB 40 (project part 4).

CHAPTER 5

PUBLICATION

Feshbach resonances in the ^{6}Li-^{40}K Fermi-Fermi mixture: Elastic versus inelastic interactions [1]

Eur. Phys. J. D **65**, 55 (2011)

D. Naik,[1] A. Trenkwalder,[1] C. Kohstall,[1,2] F.M. Spiegelhalder,[1] M. Zaccanti,[1,3] G. Hendl,[1] F. Schreck,[1] R. Grimm,[1,2] T.M. Hanna,[4] and P.S. Julienne[4]

[1]*Institut für Quantenoptik und Quanteninformation, Österreichische Akademie der Wissenschaften, 6020 Innsbruck, Austria*

[2]*Institut für Experimentalphysik, Universität Innsbruck, 6020 Innsbruck, Austria*

[3]*LENS, Physics Department, University of Florence and INO-CNR, 50019 Sesto Fiorentino, Italy*

[4]*Joint Quantum Institute, NIST and University of Maryland, 100 Bureau Drive, Stop 8423, Gaithersburg MD 20899-8423, USA*

We present a detailed theoretical and experimental study of Feshbach resonances in the ^{6}Li-^{40}K mixture. Particular attention is given to the inelastic scattering properties, which have not been considered before. As an important example, we thoroughly investigate both elastic and inelastic scattering properties of a resonance that occurs near 155 G. Our theoretical predictions based on a coupled channels calculation are found in excellent agreement with the experimental results. We also present theoretical results on the molecular state that underlies the 155 G resonance, in particular concerning its lifetime against spontaneous dissociation. We then present a survey of resonances in the system, fully characterizing the corresponding elastic and inelastic scattering properties. This provides the essential information to identify optimum resonances for applications relying on interaction control in this Fermi-Fermi mixture.

[1]The author of the present thesis contributed to the data analysis. T.M.H. and P.S.J. provided the theoretical calculations.

5.1 Introduction

A new frontier in the research field of strongly interacting Fermi gases [Ing08b, Gio08] has been approached by the recent realizations of ultracold Fermi-Fermi mixtures of ^{6}Li and ^{40}K [Tag08, Wil08, Voi09, Spi09, Tie10, Spi10b, Cos10]. Degenerate Fermi-Fermi mixtures represent a starting point to experimentally explore a rich variety of intriguing phenomena, such as many-body quantum phases of fermionic mixtures [Liu03, For05, Paa06, Isk06, Isk07, Pet07, Isk08, Bar08, Bau09, Nis09a, Wan09, Mor09, Gez09, Die10, Baa10] and few-body quantum states [Pet05a, Nis09b, Lev09, Nis10].

The possibility to precisely tune the interspecies interaction via Feshbach resonances [Chi10] is an important prerequisite for many experiments. This has motivated theoretical and experimental work on Feshbach resonances in the ^{6}Li-^{40}K mixture [Wil08, Tie09, Tie10]. It turned out that all resonances for *s*-wave scattering in this system are quite narrow, the broadest ones exhibiting a width of $\lesssim 2\,$G[1], and their character is closed-channel dominated [Chi10]. This causes both practical and fundamental limitations for experimental applications. Interaction control is practically limited by magnetic field uncertainties and, on more fundamental grounds, the universal range [Chi10] near the center of the resonance is quite narrow.

Our work is motivated by identifying the Feshbach resonances in the ^{6}Li-^{40}K system that are best suited for realizing Fermi-Fermi mixtures in the strongly interacting regime. In a previous study [Tie10], Tiecke *et al.* approached this question by calculating the widths of the different resonances[2], and they studied elastic scattering for one of the widest resonances in the system. Another important criterion is stability against inelastic two-body decay. For the ^{6}Li-^{40}K mixture, inelastic spin-exchange collisions do not occur when at least one of the species is in its lowest spin state [Wil08]. When one of the species is in a higher state, decay is energetically possible, but rather weak as it requires spin-dipole coupling to outgoing higher partial waves. The wider resonances in the ^{6}Li-^{40}K system are found in higher spin channels. This raises the important issue of possible inelastic two-body losses. The question of which is the optimum resonance for a particular application can only be answered if both width and decay are considered.

In this Article, we present a detailed study of Feshbach resonances in the ^{6}Li-^{40}K system, characterizing their influence on both elastic and inelastic scattering properties. In Sec. 5.2 we briefly review a general formalism to describe decaying resonances. In Sec. 5.3 we present a case study of a particularly interesting resonance. In theory and experiment, we investigate its elastic and inelastic scattering properties and the properties of the underlying molecular state. In Sec. 5.4 we present a survey of all resonances, summarizing their essential properties. In Sec. 5.5 we conclude by discussing the consequences of our insights for ongoing experiments towards strongly interacting Fermi-Fermi mixtures.

[1] Here, $\mathrm{G} = 0.1\,\mathrm{mT}$.

[2] Resonance positions and widths have also been calculated by E. Tiemann using a coupled channels approach similar to our theoretical work, private communication.

5.2 Feshbach resonances with decay

A Feshbach resonance results from the coupling of a colliding atom pair to a near-degenerate bound state. If this molecular state can decay into open channels other than that in which the colliding pair is initially prepared, the situation is referred to as a decaying resonance [Chi10]. A formalism for describing such resonances has been developed for optical coupling [Fed96, Boh99], and has also been applied to the magnetically tunable case [Hut07]. A well known example of a decaying resonance exists in the collision of two ^{85}Rb atoms [Rob98], for which molecular lifetimes have been studied [Tho05, Köh05].

The scattering properties in the zero-energy limit can be expressed through a complex s-wave scattering length, $\tilde{a} = a - ib$, where a and b are real. The relation of these two parameters to the two experimentally relevant quantities, the elastic scattering cross section σ and the loss rate coefficient K_2 for inelastic decay, is for non-identical particles given by

$$\sigma = 4\pi(a^2 + b^2) \tag{5.1}$$

and

$$K_2 = \frac{2h}{\mu} b\,. \tag{5.2}$$

Here, h is Planck's constant and μ is the reduced mass.

The complex scattering length can be parametrized by

$$a(B) = a_{\mathrm{bg}} - a_{\mathrm{res}} \frac{\gamma_{\mathrm{B}}(B - B_0)}{(B - B_0)^2 + (\gamma_{\mathrm{B}}/2)^2}\,, \tag{5.3}$$

$$b(B) = 2a_{\mathrm{res}} \frac{(\gamma_{\mathrm{B}}/2)^2}{(B - B_0)^2 + (\gamma_{\mathrm{B}}/2)^2}\,. \tag{5.4}$$

Here, B is the magnetic field strength, the resonance occurs at $B = B_0$, and a_{bg} is the background scattering length. The decay of the "bare" molecular state that causes the resonance is characterized by a rate γ [Köh05], which we conveniently express in magnetic field units, $\gamma_{\mathrm{B}} = \hbar\gamma/\delta\mu$, where $\delta\mu$ is the difference in magnetic moment between the entrance channel and the bare molecular state. The resonance length parameter a_{res} is related to the resonance width Δ by

$$a_{\mathrm{res}} = \frac{a_{\mathrm{bg}}\Delta}{\gamma_{\mathrm{B}}}\,, \tag{5.5}$$

and gives the range $a_{\mathrm{bg}} \pm a_{\mathrm{res}}$ within which the real part of the scattering length can vary, thus providing an indication of the possible control. A common figure of merit for the coherent control of an ultracold gas is the ratio a/b. For $|B - B_0| \gg \gamma_{\mathrm{B}}$, and a change in scattering length much larger than a_{bg}, this can be shown from Eqs. (5.3) and (5.4) to be

$$\frac{a}{b} \approx -2\frac{(B - B_0)}{\gamma_{\mathrm{B}}} \approx 2\frac{a_{\mathrm{res}}}{a}\,. \tag{5.6}$$

A larger a_{res} therefore gives better coherent control and lower losses for a given change in scattering length. Combining Eqs. (5.2) and (5.6) gives a simple expression for the loss rate coefficient

$$K_2 \approx \frac{h}{\mu}\frac{a^2}{a_{\mathrm{res}}}\,, \tag{5.7}$$

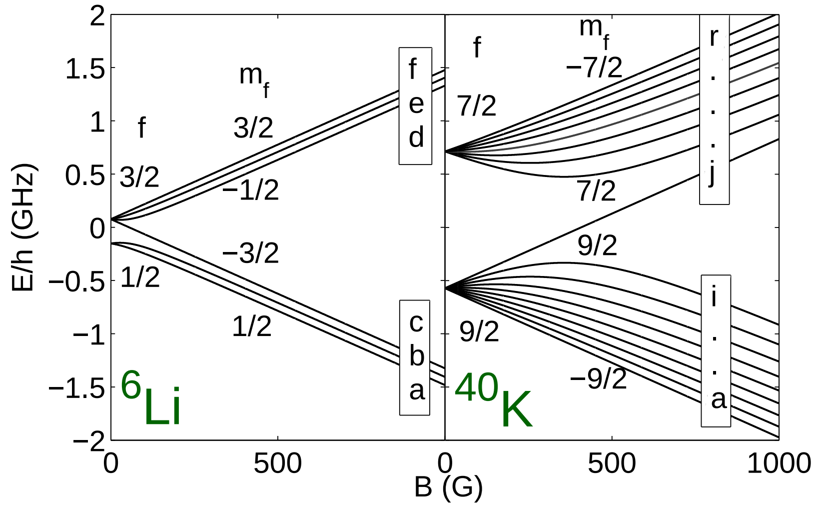

Figure 5.1: Zeeman sub-levels in the electronic ground state of ^{6}Li and ^{40}K, giving the total angular momentum f and its projection m_f along the quantization axis. We label Zeeman states alphabetically in order of increasing energy, as shown.

which shows a general a^2-scaling of two-body loss near a decaying Feshbach resonance.

5.3 Case study of the 155 G resonance

In this Section, we present a thorough study of the 155 G Feshbach resonance, which serves as our main tool for interaction tuning in strongly interacting Fermi-Fermi mixtures. It was first observed in Ref. [Wil08] and used for molecule formation in Ref. [Voi09]. We first (Sec. 5.3.1) present theoretical predictions for the elastic and inelastic scattering properties near this resonance based on coupled channels calculations. We then (Sec. 5.3.2) present our corresponding experimental results, providing a full confirmation of the expected resonance properties. We finally (Sec. 5.3.3) discuss the properties of the molecular state that causes the resonance.

Figure 5.1 shows different magnetic and hyperfine sub-levels of the electronic ground states of ^{6}Li and ^{40}K. Here we follow the notation of Ref. [Chi10] and label the sub-states alphabetically in increasing order of energy. The 155 G resonance occurs in the ac channel, i.e. for a ^{6}Li atom in state a colliding with a ^{40}K atom in state c.

5.3.1 Scattering properties: Theory

We have carried out coupled channels studies [Mie96] of the scattering properties in the ac $s-$wave channel. The potentials used were taken from Ref. [Tie09] and, to make this paper self-contained, we have summarized the important parameters in Table 5.1.

The resonance is created by spin-exchange coupling [Chi10] of the colliding pair to a bound state of the same $M_F = m_1 + m_2$. Here $m_{1,2}$ are the projections along the magnetic

singlet scattering length a_s	$52.61\,a_0$
triplet scattering length a_t	$64.41\,a_0$
vdW coefficient C_6	$2322\,E_h$
vdW length $R_\mathrm{vdW} = \frac{1}{2}(2\mu C_6/\hbar^2)^{1/4}$	$40.8\,a_0$
vdW energy $E_\mathrm{vdW} = \hbar^2/(2\mu R_\mathrm{vdW}^2)$	$h \times 207.6\,\mathrm{MHz}$

Table 5.1: Important parameters of the interaction potentials of ^{6}Li–^{40}K, taken from the potentials of Ref. [Tie09]. The van der Waals (vdW) parameters describe the long range part of the potential, $-C_6/r^6$, where r is the interparticle distance. Here, $a_0 = 0.529177 \times 10^{-10}\,\mathrm{m}$ is the Bohr radius and $E_h = 4.359744 \times 10^{-18}\,\mathrm{J}$ represents a hartree.

field quantization axis of the total angular momenta of atoms 1 and 2, $\vec{f}_{1,2}$, and M_F is that of the total spin angular momentum, $\vec{F} = \vec{f}_1 + \vec{f}_2$. We note that f and F are only good quantum numbers at zero magnetic field.

For a pair of atoms in an excited Zeeman channel, there are two processes that can cause two-body collisional loss. Spin-exchange coupling can lead to inelastic spin relaxation (ISR), in which the colliding pair is coupled into an energetically lower channel of the same M_F and the same partial wave ℓ. Since each resonance considered in this work is in the energetically lowest $s-$wave channel of the relevant M_F, ISR does not occur. Spin dipole coupling [Chi10], however, can couple a colliding pair to channels of a different M_F or ℓ, under the constraints that $M_\mathrm{tot} = M_F + m_\ell$ is conserved, and the change in partial wave is given by $\Delta\ell = \pm 2$. Here, m_ℓ is the projection of $\vec{\ell}$ along the magnetic field quantization axis. For the resonances considered here, spin dipole coupling links s- and d-waves, d- and g-waves, etc., with odd partial waves excluded by symmetry requirements. For the ac channel, the two main decay pathways are the aa and ab $d-$wave channels. Consequently, a basis including all $s-$ and $d-$wave channels with $M_\mathrm{tot} = -2$ is sufficient.

Scattering properties in the vicinity of the 155 G resonance are shown in Fig. 5.2, along with the fit from Eqs. (5.2)-(5.4). The calculation used a collision energy of $k_\mathrm{B} \times 1\,\mathrm{pK}$, while the fit assumes zero temperature. The fit gives excellent agreement, with only small deviations visible outside the core of the resonance, and at the very center, where effects related to finite collision energies become important. The background scattering length near the resonance is $63.0\,a_0$, a suitable value for evaporative cooling, while the resonance width of 0.88 G makes it easily accessible experimentally. The calculation places the center of the resonance at $B_0 = 154.75\,\mathrm{G}$, with an uncertainty on the order of 100 mG resulting from the limited knowledge of the spectroscopically derived potentials.

Suppression of collisional losses is provided by the $k_\mathrm{B} \times 14\,\mathrm{mK}$ height of the d-wave barrier being greater than the Zeeman splitting ($k_\mathrm{B} \times 1.8\,\mathrm{mK}$ for ab, $k_\mathrm{B} \times 3.6\,\mathrm{mK}$ for aa) between the entrance and exit channels. Consequently, decaying pairs must tunnel through the centrifugal barrier. The resulting resonance length is $4.0 \times 10^6\,a_0$. This is comparable to results we have found for much broader, entrance-channel dominated resonances, such as the ee resonance of ^{85}Rb at $B_0 = 155\,\mathrm{G}$, which has $a_\mathrm{res} = 2.5 \times 10^6 a_0$. We note that three-body effects, not included in our calculations, are also of significance for experiments.

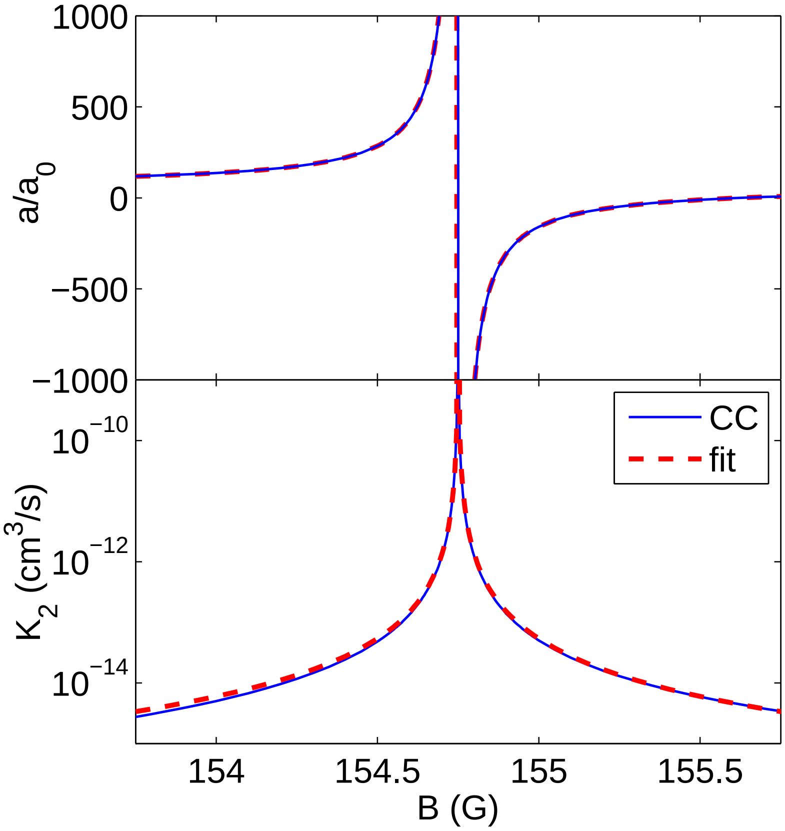

Figure 5.2: s-wave scattering properties of the ac channel, as a function of magnetic field. A coupled channels calculation (CC, solid line) is compared to a fit using Eqs. (5.2)–(5.4) (dashed line). The top panel shows the real part of the scattering length, while the two-body loss rate coefficient is shown in the lower panel.

5.3.2 Scattering properties: Experiment

Experimental conditions

The basic procedures to prepare the Fermi-Fermi mixture near the 155 G Feshbach resonance are described in Ref. [Spi10b]. Here we briefly summarize the main experimental parameters, and mention some issues of particular relevance for the present experiments.

Our optical dipole trapping scheme employs two stages. In the first stage, we use a high-power laser source (200 W fiber laser) to load and evaporatively cool the mixture [Spi09, Spi10b]. As the quality of this high-power beam suffers from thermally induced effects such as spatial shifts and thermal lensing effects, we transfer the mixture into a second trapping beam that uses less laser power and is optimized for beam quality. This beam serves as the trapping beam in the second stage where all the measurements are performed. As the laser source we either use a broadband 5 W fiber laser (IPG YLD-5-1064-LP, central wavelength

1065 nm) or a 25 W single-mode laser (ELS VersaDisk 1030-50, central wavelength 1030 nm)[3]. In both cases the trapping potential (Gaussian beam waist 41 μm) is essentially the same, but we found that the broadband fiber laser can induce inelastic losses[4]. For our measurements on elastic interactions (Sec. 5.3.2) we used the broadband laser, and we later switched to the single-mode laser for the measurements of inelastic decay (Sec. 5.3.2). At a laser power of 70 mW the trapping frequencies for Li (K) are 13 Hz (4.5 Hz) axially[5] and 365 Hz (210 Hz) radially, and the trap depth is 1.6 μK (3.6 μK).

The mixture contains about 10^5 Li atoms at a temperature $T^{\mathrm{Li}} \approx 140$ nK together with about 2×10^4 K atoms at a temperature $T^{\mathrm{K}} \approx 160$ nK; the temperatures are measured by time-of-flight imaging. Note that the two species are not fully thermalized at this point, such that $T^{\mathrm{K}} > T^{\mathrm{Li}}$. In terms of the corresponding Fermi temperatures $T_F^{\mathrm{Li}} = 490$ nK and $T_F^{\mathrm{K}} = 140$ nK, the temperatures can be expressed as $T^{\mathrm{Li}}/T_F^{\mathrm{Li}} \approx 0.3$ and $T^{\mathrm{K}}/T_F^{\mathrm{K}} \approx 1.1$.

The magnetic field was calibrated by driving RF transitions between the b and the c state of K and using the Breit-Rabi formula[6]. In our set of measurements on the elastic scattering properties (Sec. 5.3.2) the magnetic-field uncertainty was about 20 mG, with a substantial contribution from magnetic field ripples connected with the 50-Hz power line. In the later experiments on inelastic decay (Sec. 5.3.2) we could reduce this uncertainty down to about 5 mG.

Elastic Scattering

Our measurements on elastic scattering are based on the observation of sloshing motion, serving as a simple and sensitive probe for interspecies interactions [Gen01, Mad00a, Fer02, Fer03]. Without interaction both components would oscillate independently with their different sloshing frequencies. The interaction induces friction between the two components and thus leads to damping. In the regime of weak interactions with up to a few scattering events per oscillation period, the damping rate can be assumed to be proportional to the elastic scattering cross section. Note that an alternative approach, based on cross-dimensional relaxation, was followed in Ref. [Cos10].

Here we restrict our attention to the slow axial sloshing motion. We excite this motion by an additional infrared beam intersecting our trapping beam[7]. The magnetic field is quickly

[3] Specific product citations are for the purpose of clarification only, and are not an endorsement by the authors, JQI or NIST.

[4] When using the fiber laser (bandwidth 0.5 nm) we found inelastic loss near the 155 G Feshbach resonance to be enhanced by roughly a factor of four. We attribute this effect to light-induced collisional decay [Chi10], which we confirmed by measuring its dependence on the intensity of the trapping light. When using the single-mode laser this loss contribution was absent. Consequently, all measurements on inelastic decay were performed with the single-mode laser.

[5] The axial confinement predominantly results from the curvature of the magnetic field.

[6] In the vicinity of the resonance the transition frequency between the b and the c state of ^{40}K can be expressed as $\nu_{\mathrm{RF}} = 38.5756\,\mathrm{MHz} + 195.5\,\mathrm{kHz/G} \times (B - 154.707\,\mathrm{G})$.

[7] The displacement beam is derived from the same laser source as the trapping beam. It has a power of 25 mW and a waist of 60 μm, and it intersects the trapping beam at an angle of 17.5° about 120 μm away from the focus of the trapping beam. By adiabatically turning on the displacement beam we shift the centers of the two trapped species in the axial direction. Then, by suddenly extinguishing the displacement beam, the clouds are released into the unperturbed trap potential and they start their oscillations.

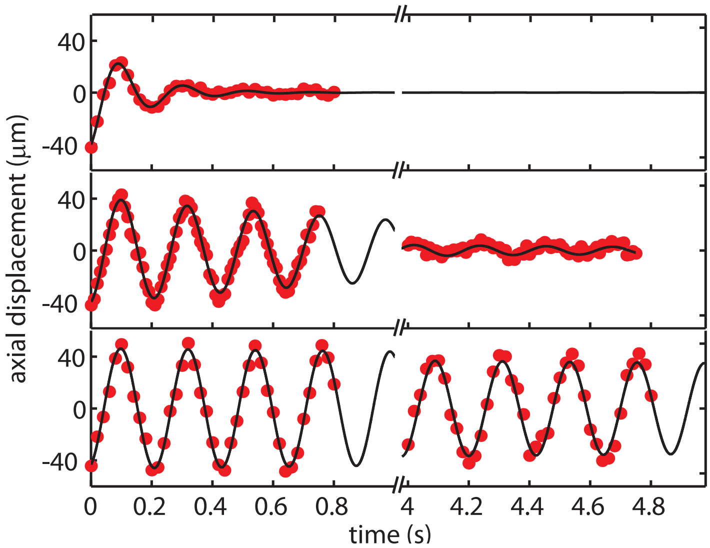

Figure 5.3: Samples of the damped sloshing motion of ^{40}K for three different settings of the magnetic field (upper panel 154.60 G, middle panel 154.96 G, lower panel 155.66 G). The solid circles represent the experimental data, with uncertainties smaller than the size of the symbols. The solid lines are fits under the assumption of a simple damped harmonic oscillation.

ramped to the final setting that is applied in the measurements. After a variable hold time in the trap, we image both clouds to record their damped oscillatory motions. Our data analysis is based on the position of the K cloud, which is completely immersed in the much larger Li cloud. Its motion is analyzed by fitting a simple damped harmonic oscillation,

$$z(t) = Ae^{-\zeta t}\sin(\omega t + \phi) + z_0\,, \tag{5.8}$$

to the observed axial center-of-mass position. Here A is the oscillation amplitude, ζ represents the damping rate, ω is the oscillation frequency, and z_0 the equilibrium position.

Near the Feshbach resonance, the observed damping strongly depends on the magnetic field, as demonstrated by the three sample oscillations displayed in Fig. 5.3. The measured damping rate as a function of the magnetic field, shown in Fig. 5.4, reflects the characteristic Fano profile of the elastic scattering cross section. The measured rates vary over three orders of magnitude, prominently showing both the pole of the resonance and its zero crossing.

We analyze the observed magnetic-field dependence of the damping under the basic assumption that the rate ζ is proportional to the elastic scattering cross section, which itself is proportional to a^2. Moreover, we take a background damping[8] into account which is independent of the interspecies interaction and express the total magnetic-field dependent damping rate as

$$\zeta(B) = Aa(B)^2 + \zeta_0\,. \tag{5.9}$$

[8] Weak damping of K sloshing with a rate of $\sim$0.04 s^{-1} is also observed when the Li component is absent. We attribute this residual damping to imperfections of the trapping potential such as corrugations and anharmonicities.

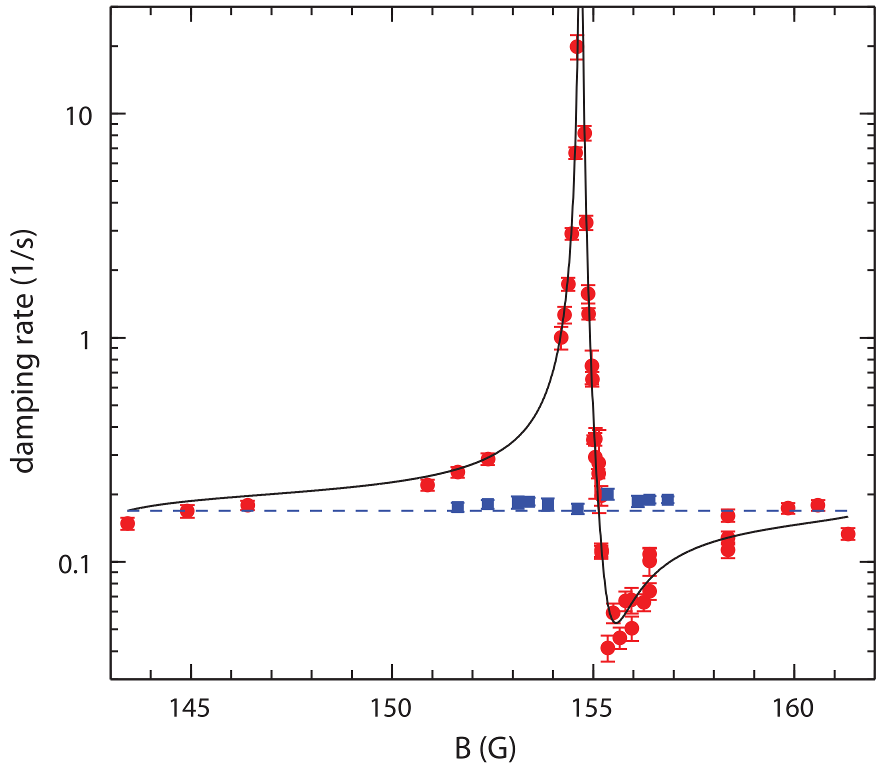

Figure 5.4: Elastic scattering near the 155 G interspecies Feshbach resonance. The measured rates for the ^{40}K sloshing motion are shown (filled red circles) together with a fit based on a coupled-channels calculation of the scattering length (solid black line). For comparison we also plot damping rates measured for the non-resonant *ab* channel (solid blue squares) together with a theoretical line derived from the corresponding non-resonant scattering length (dashed blue line). The error bars shown for the experimental data indicate the fit errors of the damping rate.

For the scattering length $a(B)$ we use the result of the coupled-channels calculation as presented in Sec. 5.3.1. The theory has an uncertainty in the resonance position of the order of 100 mG, limited by the accuracy of the spectroscopically derived potentials. We therefore allow for a magnetic-field offset by setting

$$a(B) = a_{cc}(B + \delta)\,, \tag{5.10}$$

where $a_{cc}(B)$ refers to the scattering length resulting from the coupled-channels calculation (Sec. 5.3.1) and δ is used as a free parameter. Based on Eqs. (5.9) and (5.10) we fit the experimental damping data with the three free parameters A, ζ_0, and δ.

The fit result, shown by the solid line in Fig. 5.4, shows excellent agreement with the experimental data. For the background damping of the non-interacting mixture, the fit yields $\zeta_0 = 0.0053(3)\,\mathrm{s}^{-1}$, which is consistent with independent measurements on K without Li[8]. For the magnetic field offset parameter, the fit yields $\delta = +69(3)$ mG. Based on the theoretical results of Sec. 5.3.1 and this shift, we obtain a resonance position of 154.69(2) G with the 20 mG calibration uncertainty being the dominant error source.

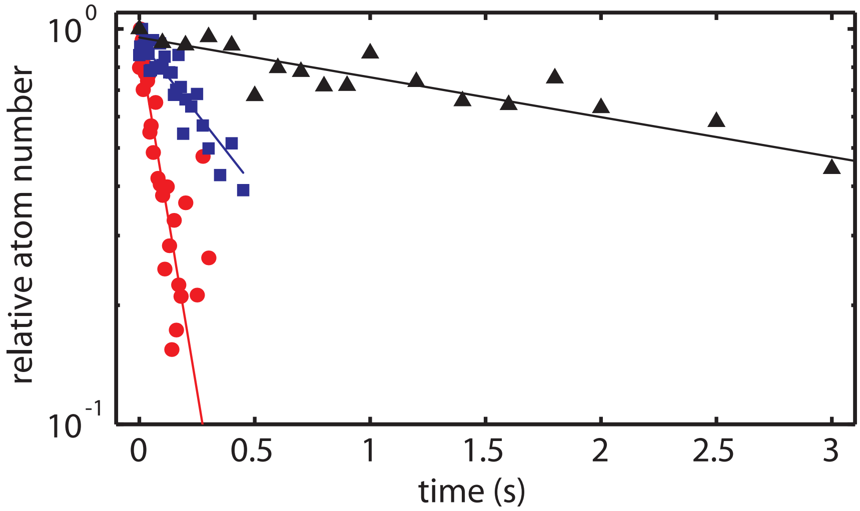

Figure 5.5: Decay of K immersed in the Li cloud for different magnetic fields, far away from resonance at 154.770 G (triangles), very close to resonance at 154.716 G (circles), and for a setting in between at 154.731 G (squares). The scatter of the data indicates the shot-to-shot variations of the measurements. As the lifetimes are plotted on a logarithmic scale, the good linear fits indicate pure exponential decay.

The experimental data can also be analyzed independently of the coupled-channels calculations by using the standard Feshbach resonance expression (Eq. (5.3) in the limit $\gamma_B \rightarrow 0$) for a fit in which the width Δ is kept as a free parameter. Our corresponding result $\Delta = 920(50)$ mG is consistent with the prediction $\Delta = 880$ mG resulting from the coupled-channels calculation.

For comparison, we have also investigated elastic scattering in a Li-K mixture in the *ab* channel (solid squares in Fig. 5.4), which near 155 G is weakly interacting. Our measurements show a damping of the sloshing motion that is consistent with the predicted non-resonant scattering length of 68 a_0 for this channel (solid line).

Inelastic Scattering

To probe inelastic decay, we first prepare a weakly interacting, long-lived Li-K mixture in the *ab* channel at a variable magnetic field near 155 G. We then apply a short RF π-pulse (duration 90 μs) to quickly transfer the mixture into the *ac* channel. This transfer method avoids fast magnetic field ramps and thus any waiting time for the magnetic field to be settled to a constant value before measurements can be taken.

Figure 5.5 shows example decay curves. The K loss is essentially exponential, which results from the fact that the K cloud is immersed in a much larger Li sample [Spi09]. In this regime, the Li cloud serves as a large bath with essentially constant density. Here the loss curves do not allow us to distinguish between two-body losses where one K atom interacts with one Li atom and such three-body losses, where one K atom interacts with two Li atoms. Three-body losses resulting from two K atoms interacting with one Li atom would not lead

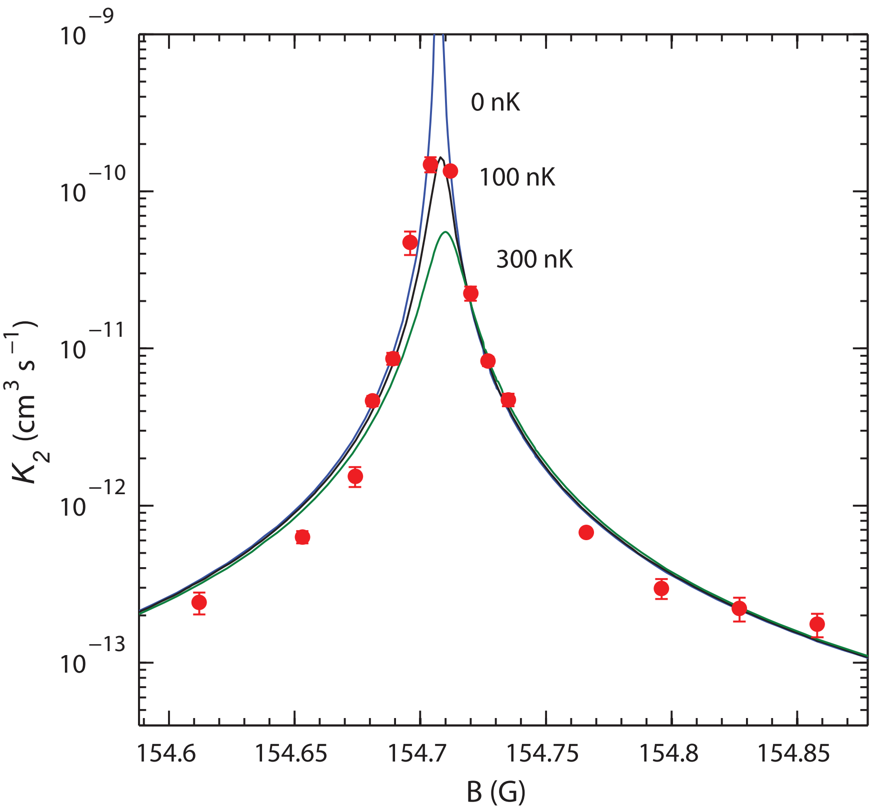

Figure 5.6: Inelastic loss near the 155 G interspecies Feshbach resonance. The measured values for the two-body loss rate coefficient K_2 (solid circles) are compared with theory. The three theoretical curves (solid lines) represent three different collision energies E/k_B (1 pK, labelled 0 to indicate the zero energy limit, 100 nK, and 300 nK), showing the limiting effect of finite collision energy. The error bars represent the statistical errors from fitting the loss curves.

to exponential loss.

We analyze the decay under the hypothesis of dominant two-body loss, which is motivated by the decaying character of the Feshbach resonance as discussed in Sec. 5.3.1. The total K decay rate can be approximated by $\Gamma = K_2\langle n_{\mathrm{Li}}\rangle + \Gamma_{\mathrm{bg}}$, where Γ_{bg} is a small background loss rate[9]. The mean Li number density is given by $\langle n_{\mathrm{Li}}\rangle$, where the angle brackets denote averages weighted by the K density distribution. For our experimental parameters we obtain $\langle n_{\mathrm{Li}}\rangle = 5.9\times10^{11}\,\mathrm{cm}^{-3}$, which is about 75 % of the peak density in the center of the Li cloud.

Figure 5.6 shows the measured values for the loss rate coefficient K_2. The data show the expected resonance behavior (Sec. 5.3.1). The values peak at the center of the Feshbach resonance and strongly decrease within a few 10 mG away from the center. For large scattering lengths, the data follow the scaling $K_2 \propto a^2$ according to Eq. (5.7). The observed resonance behavior thus confirms our assumption of the dominant two-body nature of loss. Three-

[9] The background loss results mainly from rest gas collisions. We use $\Gamma_{\mathrm{bg}} = 0.009\,\mathrm{s}^{-1}$, which we obtained by analyzing the decay of a pure K sample [Spi09]. Regardless, the influence of this weak loss contribution on our data analysis remains very small.

body losses in a two-component Fermi mixture would show a much stronger dependence on a [D'I05], not consistent with this observed behavior. However, significant three-body loss contributions may be present very near to the resonance center.

The figure also shows three theoretical curves, calculated for three different values of the collision energy ($k_B \times 1\,$pK, representing the zero energy limit, $k_B \times 100\,$nK, and $k_B \times 300\,$nK) in a range relevant for our experiments. As a typical value for the collision energy, we can consider an estimate of 200 nK[10]. Very close to the resonance the theory curves illustrate how K_2 increases in the zero temperature limit up to a value corresponding to $b = 2a_{\rm res}$. In the case of non-zero collision energies it is limited to lower values. For magnetic detunings exceeding about 20 mG, the effect of the finite collision energies can be neglected in the interpretation of the experimental data, which makes the comparison between theory and experiment straightforward. Here we find excellent quantitative agreement, confirming two-body decay as the dominant loss mechanism. Very close to the center of the resonance the situation is more complicated. If one completely attributes loss to two-body decay, the 100 nK curve provides an excellent fit to the experimental data. This, however, is somewhat below our estimate of 200 nK for an effective collision energy, which may point to additional three-body losses at the very center of the resonance.

To extract the precise resonance position we proceed in an analogous way as for analyzing the elastic scattering data, allowing for a small magnetic field shift δ between theory and experiment. We write the actual loss coefficient as $K_2(B) = K_{2,cc}(B + \delta)$, where $K_{2,cc}$ refers to the coupled-channels result for K_2 as discussed in Sec. 5.3.1. In the fit, we exclude the three experimental data points that exceed $3 \times 10^{-11}\,\mathrm{cm}^3/s$ to avoid the region where finite collision energies become important. This also makes sure that the loss data are dominated by two-body decay. The shift δ is the only free parameter, and we obtain a small value of $\delta = +38(1)\,$mG, well in the range of the theoretical uncertainty. We finally obtain a resonance position of $B_0 = 154.707(5)\,$G, where the main uncertainty results from the magnetic field calibration. Within the experimental uncertainties this value is consistent with the less precise resonance position obtained from elastic scattering measurements.

5.3.3 Bound state properties

In the context of Feshbach molecules, universality refers to the range of magnetic fields sufficiently close to resonance within which the molecular and scattering properties can be described solely by the atomic masses and the scattering length $a(B)$. Within this region, the molecule has the form of a halo state, in which a significant part of the wavefunction lies beyond the classically allowed outer turning point of the potential. This results in a strong enhancement of the lifetime of a decaying bound state [Tho05, Köh05]. The universal binding energy is given by

$$E_{\rm B} = \frac{\hbar^2}{2\mu a(B)^2}\,. \tag{5.11}$$

[10] The main contribution to the mean collision energy in our trapped sample stems from the kinetic energy of the degenerate Li component. In the trap center, where the K cloud overlaps with the Li, the mean kinetic energy of the Li atoms is given by $(3/10)T_F^{\rm Li} \approx 200\,$nK.

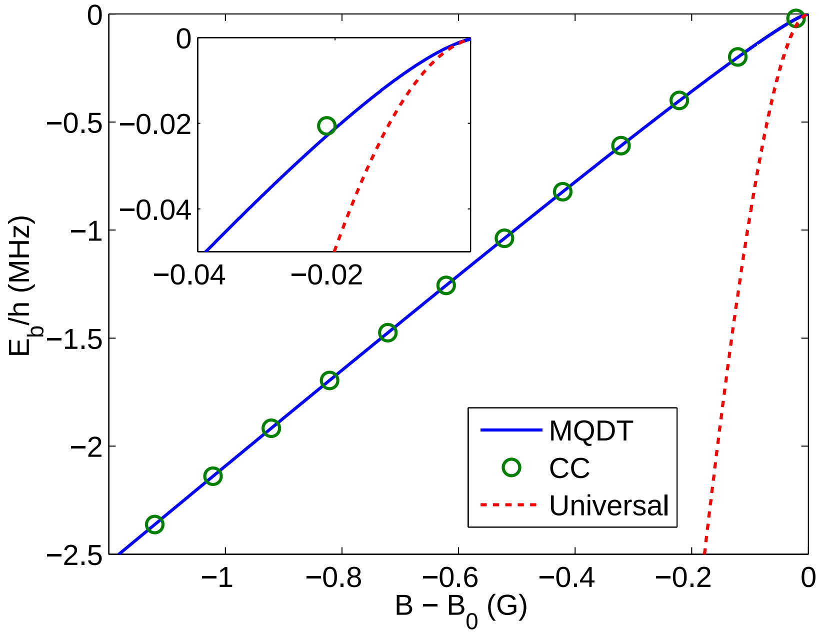

Figure 5.7: Molecular binding energy as a function of magnetic field. MQDT (blue line) refers to the three-parameter model of Ref. [Han09], while CC (green points) indicates a coupled channels calculation. Sufficiently close to the resonance the binding energy converges to the universal result of Eq. (5.11) (red dashed line).

Calculations of the relevant bound state energy using the coupled channels method and the simplified three-parameter model of Ref. [Han09] are shown in Fig. 5.7. We note that the three-parameter model, while useful for bound state and resonance characterisation, does not couple partial waves and so can not be used for calculating decay properties in the present case. The energy variation is linear for binding energies greater than a few tens of kHz, having a relative magnetic moment of $\delta\mu/h = 2.3\,\mathrm{MHz/G}$ with respect to the *ac* threshold. The universal region, as can be seen from the inset of Fig. 5.7, covers a magnetic field range of order mG. This makes it hard to access experimentally. The universal region is wider for broad, entrance channel dominated resonances [Chi10]. However, in the present case, the suppression of decay by the centrifugal barrier allows the molecules to have a long lifetime in the nonuniversal regime.

We now consider the lifetime of ^{6}Li-^{40}K molecules close to the *ac* resonance at 155 G. Outside the very narrow universal region, the analytic approach of Ref. [Köh05] does not apply. We therefore derive the molecular lifetime from a coupled channels scattering calculation including the two open d-wave channels into which it decays. The spin-dipole induced decay discussed in the previous section is mediated by the bound state causing the resonance. For collisions at an energy E near the energy E_b of this bound state, the off-diagonal $|T_{12}(E)|^2$ matrix element for the transition probability from one decay channel to the other follows the standard form [Mot65]

$$|T_{12}(E)|^2 = \frac{\hbar^2\gamma_1\gamma_2}{(E-E_\mathrm{b})^2 + \frac{\hbar^2}{4}\Gamma^2}\,. \tag{5.12}$$

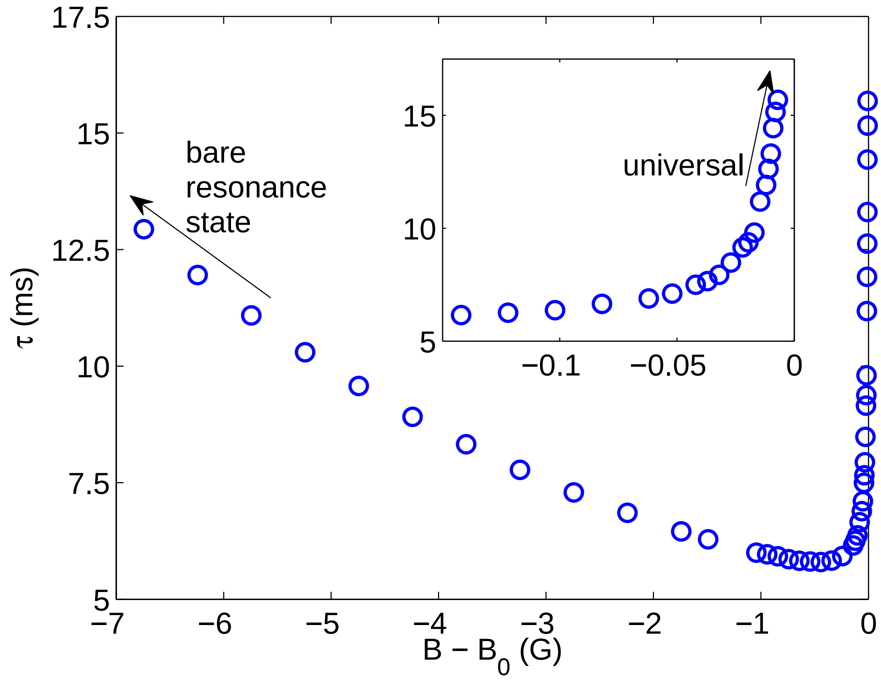

Figure 5.8: Calculated molecular lifetime as a function of magnetic field. The molecular lifetime varies at lower field according to its tunnelling rate through the d-wave centrifugal barrier into the exit channels. The arrows indicate the sharp increase in lifetime as the universal regime is entered, and the region away from resonance where the molecular lifetime converges to that of the bare resonance state.

Here, γ_1 and γ_2 are the decay rate of the molecule into the ab and aa channels, respectively. The total decay rate is given by $\Gamma = (\gamma_1 + \gamma_2)$, and the molecular lifetime by $\tau = 1/\Gamma$. Fitting our calculated $|T_{12}(E)|^2$ to the form of Eq. (5.12) determines the magnitude of Γ for a given B. This calculation includes the entrance channel component and so reproduces the increase in lifetime as the Feshbach molecule takes on a halo form. This should be distinguished from the decay rate of the bare resonance state which appears in Eqs. (5.3) and (5.4).

Our calculated lifetimes are shown in Fig. 5.8. As discussed above, a sharp increase in lifetime occurs as the universal region near B_0 is approached. Above the maximum lifetime shown in the Fig. 5.8, the decay peak described by Eq. (5.12) narrows to the point where we can no longer resolve it in our calculations. The slower increase as B is moved away from B_0 occurs because the bound state moves further behind the centrifugal barrier. Decay from tunnelling through the barrier is then further suppressed. The lifetime of molecules in the vicinity of the 155 G resonance was measured by Voigt *et al.* [Voi09]. They observed a sharp increase in lifetime near the resonance, with which our results qualitatively agree. Their measured background lifetime of ~ 3 ms away from resonance is lower than our calculated minimum of 6 ms. However, our calculations do not include relevant atom-dimer and dimer-dimer collisions, and so may be considered as an upper bound to experimentally observable lifetimes. A lifetime of several ms will permit measurements and manipulation of the Feshbach molecules.

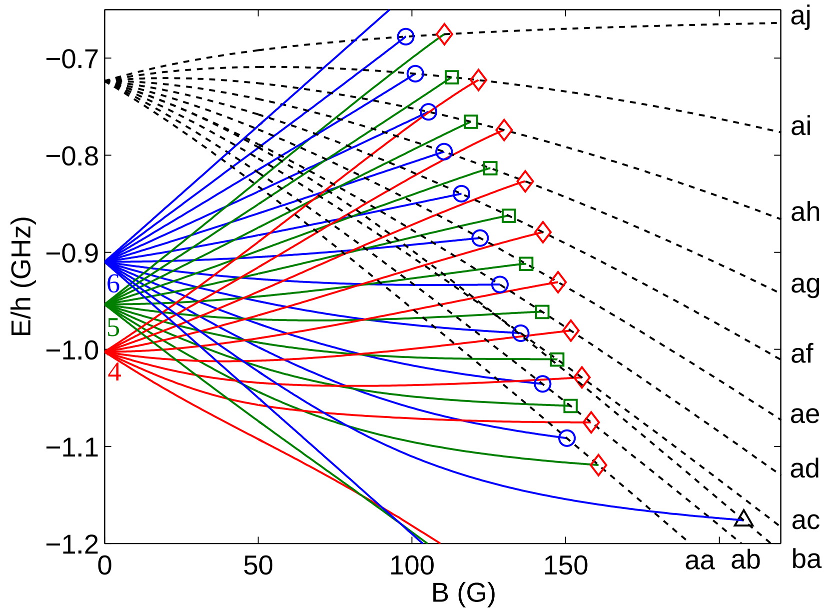

Figure 5.9: Energies of the bound states underlying the resonances studied in this paper, as a function of magnetic field. Collision thresholds of relevant channels are shown as dotted lines, labelled at the right of the figure. The resonances arise from three zero-field bound states of $F = 4, 5$ and 6 (labelled at the left of the figure), which are projected into channels of $|M_{\rm tot}| \le F$ at non-zero field. Deeper bound states are not shown for reasons of clarity. Avoided crossings between bound states of the same $M_{\rm tot}$ give rise to three identifiable groups of resonances, indicated by the same symbols used in Fig. 5.10 and Table 5.2. Within each group, resonance parameters vary smoothly (see Fig. 5.10 and text).

5.4 Survey of resonances

In this section we discuss resonances occurring in various channels of the ^{6}Li-^{40}K mixture. We focus on channels with ^{6}Li in the a state and ^{40}K in the lower ($f = 9/2$) manifold, for which inelastic spin-exchange collisions do not occur. At zero magnetic field, there are three bound states of $F = 4$, 5 and 6 in the range 200 MHz to 300 MHz below these thresholds, as shown in Fig. 5.9. At nonzero magnetic field, these states are projected into their Zeeman sublevels, which give rise to Feshbach resonances when degenerate with the collision threshold of a channel of the same $M_{\rm tot}$. Consequently, three proximate resonances are found in channels of $-3 \le M_{\rm tot} \le 4$. The bound state underlying each resonance adiabatically correlates with one of the zero field F states. We note that the bound state energies shown in Fig. 5.9 were produced with the three-parameter model of Ref. [Han09], which produces slightly different resonance locations to the coupled channels calculations that follow.

We have performed a coupled channels analysis of each resonance, analogous to that performed with the asymptotic bound state model in Ref. [Tie10]. With our more rigorous approach[2], we obtain good agreement with all experimental data, including the new set of measurements on the 155 G resonance presented in Sec. 5.3.2. The simplified approach

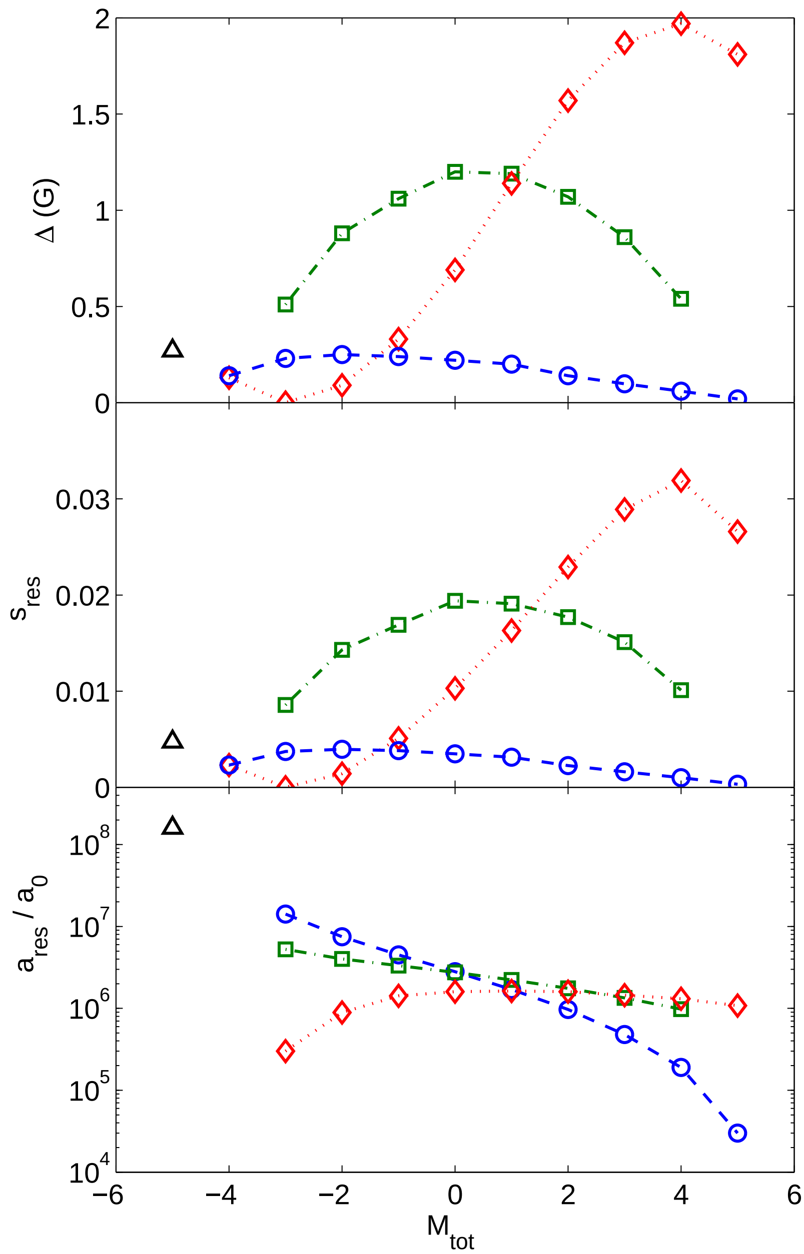

Figure 5.10: Theoretical survey of ^{6}Li–^{40}K s-wave resonances. Each panel shows a resonance parameter as a function of $M_{\rm tot}$: the width Δ (top), strength $s_{\rm res}$ (middle), and length $a_{\rm res}$ (bottom). The ^{6}Li atom is in the a state, except for $M_{\rm tot} = -5$ for which it is in b. The ^{40}K atom is in the lowest Zeeman state producing the relevant $M_{\rm tot}$. The symbols, also used in Fig. 5.9 and Table 5.2, correspond to the resonance groups discussed in the text.

			Experiment			Coupled channels						
Channel	M_{tot}	Group	B_0 (G)	Δ (G)	Ref.	B_0 (G)	Δ (G)	a_{bg}/a_0	$\delta\mu/h$ (MHz/G)	a_{res} ($10^6\,a_0$)	s_{res}	γ_B (μG)
ba	-5	△	215.6		[Wil08]	215.52	0.27	64.3	2.4	160	0.0048	0.11
aa	-4	○	157.6		[Wil08]	157.50	0.14	65.0	2.3		0.0023	0
		◇	168.170(10)		[Spi10b]	168.04	0.13	63.4	2.5		0.0023	0
ab	-3	○	149.2		[Wil08]	149.18	0.23	67.0	2.1	14	0.0037	1.1
		□	159.5		[Wil08]	159.60	0.51	62.5	2.4	5.3	0.0086	6.1
		◇	165.9		[Wil08]	165.928	2×10^{-4}	58	2.5	0.3	3.3×10^{-6}	0.04
ac	-2	○	141.7		[Wil08]	141.46	0.25	67.6	2.1	7.5	0.0040	2.3
		□	154.707(5)	0.92(5)	this work	154.75	0.88	63.0	2.3	4.0	0.014	14
		◇	162.7		[Wil08]	162.89	0.09	56.4	2.5	0.89	0.0014	5.7
ad	-1	○				134.08	0.24	68.7	2.0	4.5	0.0038	3.7
		□				149.40	1.06	63.8	2.2	3.3	0.017	20
		◇				159.20	0.33	55.8	2.45	1.4	0.0051	13
ae	0	○				127.01	0.22	68.5	2.05	2.8	0.0035	5.4
		□				143.55	1.20	65.7	2.2	2.8	0.020	29
		◇				154.81	0.69	55.1	2.4	1.6	0.010	24
af	1	○				120.33	0.20	66.8	2.1	1.7	0.0031	7.9
		□				137.23	1.19	65.3	2.2	2.2	0.019	35
		◇				149.59	1.14	53.6	2.4	1.6	0.016	37
ag	2	○				114.18	0.14	67.4	2.1	0.97	0.0023	9.7
		□				130.49	1.07	66.4	2.2	1.8	0.018	40
		◇				143.39	1.57	54.4	2.4	1.6	0.023	53
ah	3	○				108.67	0.098	66.6	2.2	0.48	0.0016	14
		□				123.45	0.86	68.4	2.3	1.3	0.015	44
		◇				135.90	1.87	55.9	2.45	1.5	0.029	72
ai	4	○				104.08	0.06	65.9	2.25	0.19	0.0010	21
		□				116.38	0.54	68.6	2.4	0.98	0.010	38
		◇				126.62	1.97	54.7	2.6	1.3	0.032	83
aj	5	○				100.90	0.02	64.3	2.3	0.03	3.2×10^{-4}	43
		◇	114.47(5)	1.5(5)	[Tie10]	114.78	1.81	57.3	2.3	1.08	0.027	96

Table 5.2: Survey of s-wave resonances in ^{6}Li-^{40}K. The first two columns give the channel $\alpha\beta$ and total angular momentum projection M_{tot}, with α and β representing the Zeeman state of Li and K, respectively. The third column gives the symbol for the corresponding group of resonances that is used in Figs. 5.9 and 5.10. The next three columns give experimental values of the resonance location B_0 and width Δ, where available, with references. The remaining columns give the results of the coupled channels calculations performed for the current work - B_0 and Δ, as well as the background scattering length a_{bg}, relative magnetic moment $\delta\mu$, resonance length a_{res}, resonance strength s_{res}, and decay rate in magnetic field units, γ_B. Note that a_{res} is not defined for the stable aa channel. Note also that the experimental values for B_0 from Ref. [Wil08] are subject to typical uncertainties of about 0.5 G.

of Ref. [Tie10] seems to underestimate the widths of the resonances by almost a factor of two. With the coupled channels approach, we can also study the decay properties of the resonances. The resonance parameters are shown in Fig. 5.10, and tabulated in Table 5.2. We group the resonances of each channel that are lowest (◯), middle (□) and highest (♢) in B_0, using the indicated symbols to distinguish the resonance groups in Figs. 5.9 and 5.10, and Table 5.2. Within each of these groups, resonance properties vary smoothly as a function of $M_{\rm tot}$. The resonances with $M_{\rm tot} = -4$ and 5 have properties consistent with the lowest and highest group, while the *ba* resonance with $M_{\rm tot} = -5$ has substantially different properties. This is due to F being a good quantum number only at zero magnetic field, and several bound states having avoided crossings in the relevant range of magnetic field. There are several resonances with $\Delta \gtrsim 1\,$G, offering good opportunities for control of collisional properties. However, several other factors are also useful for deciding the suitability of a resonance for a given application.

One parameter used for quantifying the extent to which a resonance is entrance-channel dominated is the resonance strength parameter [Chi10], defined by

$$s_{\rm res} = \frac{a_{\rm bg}}{\bar{a}} \frac{\delta\mu\Delta}{\bar{E}} \,. \tag{5.13}$$

Here, $\bar{a} = [4\pi/\Gamma(1/4)^2]R_{\rm vdw} \approx 0.956 R_{\rm vdW}$ is the mean scattering length [Gri93], and $\bar{E} = \hbar^2/(2\mu\bar{a}^2) \approx 1.094 E_{\rm vdW}$ is the associated energy. If $s_{\rm res} \geq 1$, the bound state and near-threshold scattering states are concentrated in the entrance channel over a magnetic field range comparable to Δ. In the present case, all resonances are closed-channel dominated, as shown in the middle panel of Fig. 5.10. The background scattering lengths of the resonances are all in the range $55\,a_0$ to $70\,a_0$, and the relative magnetic moments are in the range 2 MHz/G to 2.6 MHz/G. Consequently, the resonance strength follows trends similar to the resonance widths. For the *ac* 155 G resonance we have $s_{\rm res} = 0.014$. This is reflected in the universal region being only a few mG wide, as discussed above.

Calculated resonance lengths are shown in the lower panel of Fig. 5.10. The range in $a_{\rm res}$ is approximately 3 orders of magnitude, with better stability in channels of lower $M_{\rm tot}$. This occurs because the energy gaps between higher channels are larger, reducing the height of the centrifugal barrier through which the decaying atoms tunnel. However, all the resonance lengths are sufficiently high that we expect each resonance with $\Delta \gtrsim 1\,$G to be very useful.

In view of interaction control in a strongly interacting gas, we now discuss three selected resonances that have received particular attention in experiments: the 168 G resonance in the *aa* channel [Spi10b], the 155 G resonance in the *ac* channel [Voi09] (see Sec. 5.3), and the 114 G resonance in the *aj* channel [Tie10]. In practice, the possible degree of control is limited by uncertainties (drifts and fluctuations) of the magnetic field. A corresponding figure of merit is the maximum controllable scattering length $a_{\rm ctrl} = a_{\rm bg}\Delta/\delta_B$, where δ_B stands for the magnetic field uncertainty. Assuming a realistic value of $\delta_B = 5\,$mG one obtains $a_{\rm ctrl} \approx 1600\,a_0$, $11\,000\,a_0$, and $21\,000\,a_0$ for the three resonances considered (168 G, 155 G, and 114 G, respectively). On one hand, this can be compared with the typical requirement of $|a| \gtrsim 5000\,a_0$ for attaining strongly interacting conditions. On the other hand, it can be compared with the condition for universal behavior $|a| \gg \bar{a}/s_{\rm res}$[11], which requires $a_{\rm ctrl} \gg$

[11] $\bar{a}/s_{\rm res} = R^*$ with R^* being defined in reference [Pet04a].

17 000 a_0, 2800 a_0, and 1450 a_0. This shows that the resonance at 168 G is too narrow for controlling a strongly interacting Fermi-Fermi mixture, but the other resonances at 155 G and 114 G are broad enough. Although the 114 G resonance is wider than the 155 G resonance by a factor of 2.1, inelastic loss is 3.7 times faster. The higher collisional stability is an important advantage of the 155 G resonance.

5.5 Conclusions

We have characterized elastic and inelastic scattering near Feshbach resonances in the ^{6}Li-^{40}K mixtures. The presence of open decay channels for all broader resonances has two important consequences. Atomic two-body collisions acquire a resonantly enhanced inelastic component, which unavoidably limits the stability of an atomic Fermi-Fermi mixture with resonantly tuned interactions. When Feshbach molecules are created via these decaying resonances, they will undergo spontaneous dissociation.

The intrinsic decay has important consequences for present experiments towards strongly interacting Fermi-Fermi mixtures. Under typical experimental conditions, the lifetime of a Fermi-Fermi mixture with resonantly tuned interactions ($a \to \pm\infty$) will be limited to $\sim$10 ms. This in general means a limitation of possible experiments to short time scales, such as the observation of the expansion of the mixture after trap release [O'H02, Bou03] or measurements of fast collective oscillation modes [Kin04a, Bar04a, Alt07a]. Experiments that require long time scales, such as precise studies of equilibrium states [Zwi06a, Nas10], may be problematic in this decaying mixture.

The short lifetime of the Feshbach molecules, also being of the order of 10 ms, excludes the production of a long-lived molecular Bose-Einstein condensate (mBEC) such as formed in ^{6}Li [Joc03b, Zwi03b]. Transient ways to form mBECs, as demonstrated for ^{40}K [Gre03], will still be possible. The detection of fermionic condensates by rapid conversion of many-body pairs into molecules [Reg04] also seems to be a realistic possibility. Moreover, the predicted increase of the molecular lifetime for larger binding energies can be of general interest for the coherent manipulation of Feshbach molecules [Fer09] and in particular for optimizing the starting conditions for a transfer to the ro-vibrational ground state [Ni08, Lan08, Dan10].

Finally, the question of which Feshbach resonance provides optimum conditions for interaction tuning in ^{6}Li-^{40}K has no straightforward answer. All the broad resonances occurring in the channels ac-aj (widths 0.88 G - 1.97 G) seem to be well suited for controlled interaction tuning. Because of the tradeoff between width and stability, the best choice will depend on the particular application.

We thank Bo Gao for stimulating discussions. We acknowledge support by the Austrian Science Fund (FWF) and the European Science Foundation (ESF) within the EuroQUAM/FerMix project and support by the FWF through the SFB FoQuS. T.M.H. and P.S.J. acknowledge support from an AFOSR MURI on Ultracold Molecules.

Note

Note that the value given for B_0 refers to the particular optical trap used in the experiments. It includes a small shift induced by the trapping light, as the molecules have slightly different polarizabilities than the free atoms, leading to a difference in the Stark shift. In free space, without the light shift, the resonance center is located at 154.698(5) G, see also Methods in Chap.7.

CHAPTER 6

PUBLICATION

Hydrodynamic expansion of a strongly interacting Fermi-Fermi mixture [1]

Phys. Rev. Lett **106**, 115304 (2011)

A. Trenkwalder,[1] C. Kohstall,[1,2] M. Zaccanti,[1,3] D. Naik,[1] A. I. Sidorov,[1,4] F. Schreck,[1] and R. Grimm[1,2]

[1] *Institut für Quantenoptik und Quanteninformation, Österreichische Akademie der Wissenschaften, 6020 Innsbruck, Austria*

[2] *Institut für Experimentalphysik, Universität Innsbruck, 6020 Innsbruck, Austria*

[3] *LENS, Physics Department, University of Florence and INO-CNR, 50019 Sesto Fiorentino, Italy*

[4] *Centre for Atom Optics and Ultrafast Spectroscopy and ARC Centre of Excellence for Quantum-Atom Optics, Swinburne University of Technology, Melbourne, Australia*

We report on the expansion of an ultracold Fermi-Fermi mixture of ^{6}Li and ^{40}K under conditions of strong interactions controlled via an interspecies Feshbach resonance. We study the expansion of the mixture after release from the trap and, in a narrow magnetic field range, we observe two phenomena related to hydrodynamic behavior. The common inversion of the aspect ratio is found to be accompanied by a collective effect where both species stick together and expand jointly despite of their widely different masses. Our work constitutes a major experimental step for a controlled investigation of the many-body physics of this novel strongly interacting quantum system.

Since the first observations of strongly interacting Fermi gases [O'H02, Bou03] the field has produced many exciting results and provided important new insights into the many-body behavior of strongly interacting quantum matter [Ing08b, Blo08b, Gio08]. The general

[1] The author of the present thesis acquired the data together with A.T., performed the data analysis for the last three figures, and contributed to the interpretation of the results.

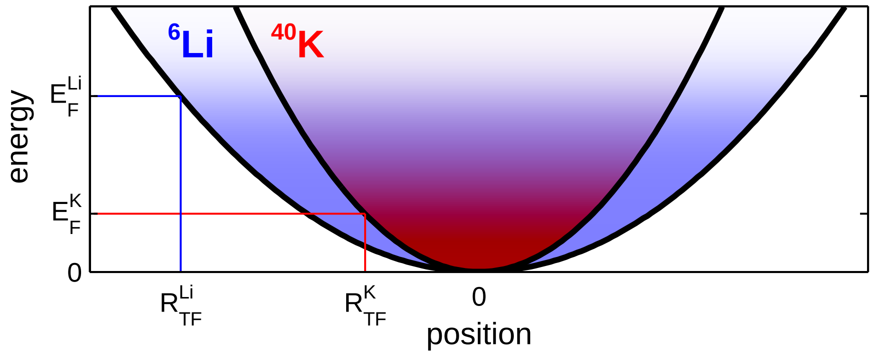

Figure 6.1: Illustration of the optically trapped Fermi-Fermi mixture. A small, moderately degenerate ^{40}K cloud resides in the center of the larger Fermi sea of ^{6}Li. The optical trapping potential of ^{40}K is about 2.1 times deeper than the one for ^{6}Li (solid lines). The Thomas-Fermi radii $R_{\rm TF}^{\rm Li}$ and $R_{\rm TF}^{\rm K}$ of both species differ by a factor of about two.

interest cuts across different branches of physics, ranging from strongly correlated condensed-matter systems to neutron stars and the quark-gluon plasma.

Experimental realizations of strongly interacting Fermi gases rely on ultracold mixtures of two components with magnetically tunable s-wave interaction. First experiments focused on spin mixtures of a single fermionic species with equal populations in two different Zeeman states [Ing08b]. The introduction of population imbalance [Zwi06b, Par06] then paved the way to the rich physics of polarized Fermi gases [Rad10, Che10]. The recent experimental efforts to create ultracold mixtures of two different fermionic species [Tag08, Wil08, Voi09, Spi09, Spi10b, Tie10, Cos10, Nai11] have brought the field close to a new research frontier with intriguing new possibilities, e.g., related to novel types of superfluids and quantum phases [Liu03, Isk07] and to new few-body states [Lev09, Nis08].

In this Letter, we report on the creation of an ultracold Fermi-Fermi mixture of ^{6}Li and ^{40}K atoms, featuring the high degree of interaction control that is necessary to explore the strongly interacting regime. As a first experimental benchmark, we demonstrate the hydrodynamic expansion after release from the trap. Near the center of an interspecies Feshbach resonance, we observe two different hydrodynamic phenomena with a pronounced dependence on the interactions strength. The first one is the well-known inversion of the aspect ratio [O'H02]. The second one is a hydrodynamic drag between both species, causing their flow velocities to be equal.

We point out that both hydrodynamic phenomena find close analogies in experiments aiming at the creation of a quark-gluon plasma [Bra07, Jac10]. Experiments of this kind study the high-energy collisions of heavy nuclei and detect the expanding collision products. In this context "elliptic flow" refers to an anisotropy of the expansion, which is understood as a consequence of the hydrodynamic interaction between the various collision products. The second analogy becomes evident in the transverse energy spectra of the collision products. Here it is found that heavier particles carry larger energies than the lighter ones [Bea97]. Such a mass-dependence is interpreted as a result of "collective flow" (see, e.g., [Yag05]), which provides another signature of the hydrodynamic nature of the expansion. The analogy between elliptic flow and the expansion of a strongly interacting Fermi gas has been pointed out already in context with early experiments on ultracold Fermi gases [O'H02, Tho10, Sch09a]. The collective flow analogy is another striking example for the fascinating relation between two fields of physics at energies differing by more than 20 orders of magnitude.

The starting point of our experiments is a weakly interacting mixture of 7.5×10^4 ^{6}Li atoms and 2.0×10^4 ^{40}K atoms in an optical dipole trap[2]; see the illustration in Fig. 6.1. The anisotropy of the trapping potential leads to a cigar-shaped sample with an aspect ratio of about 6.5. The preparation procedures are described in detail in Ref. [Spi10b]. At a temperature $T \approx 300\,\mathrm{nK}$ the Li component forms a degenerate Fermi sea with $T/T_F^{\mathrm{Li}} \approx 0.3$ and the K component is moderately degenerate with $T/T_F^{\mathrm{K}} \approx 0.7$; here the Fermi temperatures of both species are given by $T_F^{\mathrm{Li}} = 1.1\,\mu\mathrm{K}$ and $T_F^{\mathrm{K}} = 500\,\mathrm{nK}$. The K cloud is concentrated in the center of the bigger Li cloud, with approximately equal peak densities.

Interaction control is achieved by the 155 G interspecies Feshbach resonance, which occurs for Li in its lowest internal state ($m_f^{\mathrm{Li}} = +1/2$) and K in its third to lowest state ($m_f^{\mathrm{K}} = -5/2$) [Wil08, Voi09, Nai11]. The s-wave scattering length a can be tuned according to the standard resonance expression $a = a_{\mathrm{bg}}(1 - \Delta/(B - B_0))$ with $a_{\mathrm{bg}} = 63.0\,a_0$ (a_0 is Bohr's radius), $\Delta = 880\,\mathrm{mG}$, and $B_0 = 154.707(5)\,\mathrm{G}$ [Nai11].

The Li Fermi energy $E_F^{\mathrm{Li}} = k_B T_F^{\mathrm{Li}}$ represents the leading energy scale in our system. Therefore, a natural condition for strong interactions of the K minority component in the degenerate Fermi sea of Li is given by $k_F^{\mathrm{Li}}|a| > 1$, where $k_F^{\mathrm{Li}} = (2m_{\mathrm{Li}}E_F^{\mathrm{Li}})^{1/2}/\hbar = 1/(3600\,a_0)$. In terms of magnetic detuning, this condition translates to $|B - B_0| < 15\,\mathrm{mG}$. The character of the Feshbach resonance is closed-channel dominated [Chi10], but near-universal behavior can be expected throughout the strongly interacting regime [Nai11].

We create the strongly interacting mixture in a transient scheme, which minimizes the time spent near resonance and thus avoids the detrimental effect of inelastic losses [Nai11]. We start with a weakly interacting combination of spin states with $m_f^{\mathrm{Li}} = +1/2$ and $m_f^{\mathrm{K}} = -7/2$. The magnetic field is set to the target field near B_0 with an estimated uncertainty as low as 3 mG. Then we quickly convert the mixture into a strongly interacting one by flipping the spins of the K atoms to $m_f^{\mathrm{K}} = -5/2$ using a $60\,\mu\mathrm{s}$ radio-frequency π-pulse. We immediately turn off the optical trap, releasing the sample into free space. This procedure provides well-defined initial conditions for the expansion, with the density distributions being the ones of the noninteracting system.

In a first set of experiments, we study the expansion dynamics for a magnetic field very close to resonance ($B = 154.709\,\mathrm{G}$). After a variable time of flight t_{TOF}, absorption images are taken for both species and analyzed by simple two-dimensional Gaussian fits to determine their radial and axial widths, σ_r and σ_z. In Fig. 6.2 we present the resulting data in terms of the aspect ratios $A_i = \sigma_r^i/\sigma_z^i$ and volume parameters $V_i = (\sigma_r^i)^2\sigma_z^i$, where $i = \mathrm{Li}, \mathrm{K}$. For comparison, we also show corresponding measurements performed on a noninteracting sample, where the expansion proceeds ballistically and the aspect ratios asymptotically approach unity[3]. For resonant interactions, the aspect ratios of both species, A_{Li} and A_{K}, undergo an inversion, thus showing the expected hallmark of hydrodynamic behavior. Also, the volume

[2] The trap is realized with two crossed beams derived from a 1030 nm single-mode laser source. The measured trap frequencies for Li (K) are 560 Hz (390 Hz) radially and 90 Hz (57 Hz) axially.

[3] We compared the expansion of a weakly interacting mixture ($a \approx a_{\mathrm{bg}}$) with the noninteracting case realized near the zero crossing of the scattering length ($a = 0$), and found no significant difference.

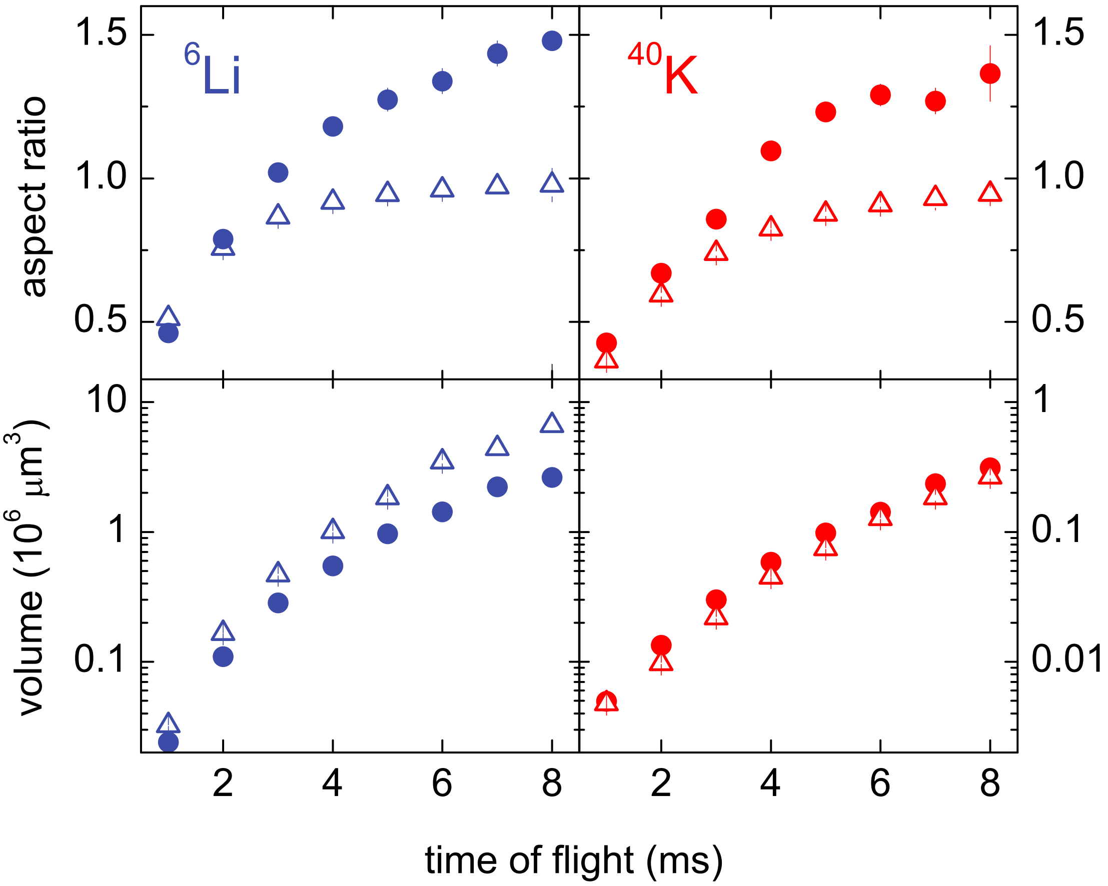

Figure 6.2: Expansion dynamics of the strongly interacting ^{6}Li-^{40}K mixture. The upper two panels show the aspect ratios A_{Li} and A_{K}, while the lower two panels display the volume parameters V_{Li} and V_{K}. The closed symbols refer to the resonant case (154.709 G), while the open symbols refer to noninteracting conditions (155.508 G). The error bars show the statistical uncertainties of the measurements.

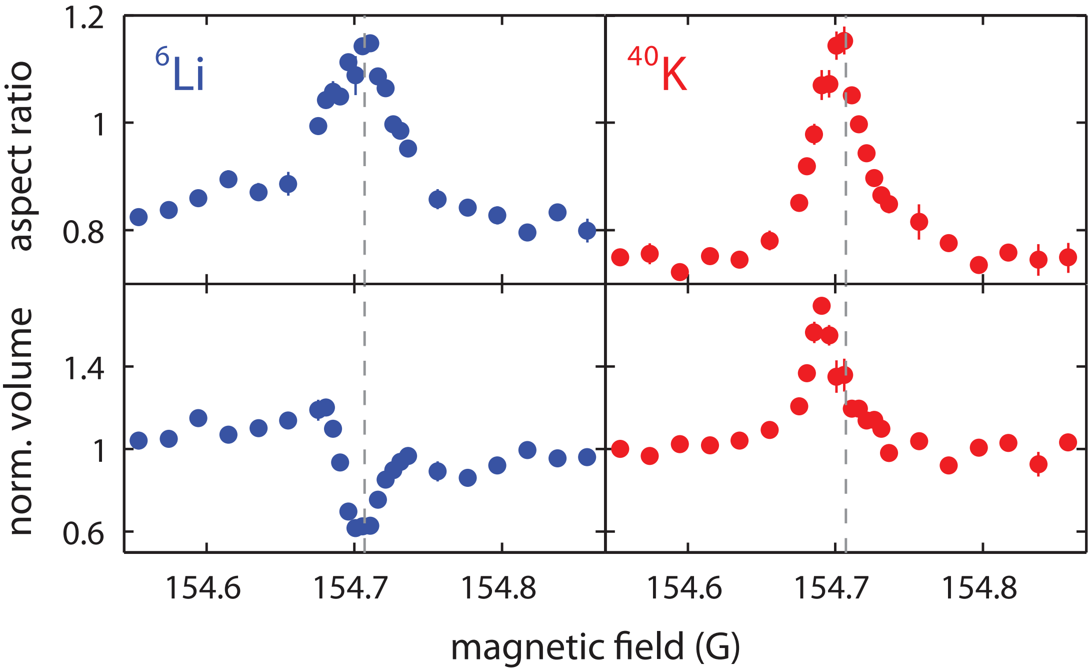

Figure 6.3: Magnetic-field dependence of the hydrodynamic expansion observed at $t_{\mathrm{TOF}} = 4\,\mathrm{ms}$. The upper panels show the aspect ratios A_{Li} and A_{K}. The lower panels show the volume parameters V_{Li} and V_{K}, normalized to their values measured for the noninteracting case. The dashed vertical lines indicate the resonance position B_0. The statistical uncertainties are on the order of the size of the symbols.

parameters V_{Li} and V_{K} reveal striking interaction effects. While V_{Li} is substantially reduced by the interaction, V_{K} shows a small but significant increase. This observation fits to the expectation of collective flow as resulting from the hydrodynamic drag effect.

In a second set of experiments, we observe the expansion at a fixed $t_{\mathrm{TOF}} = 4\,\mathrm{ms}$ for variable interaction strength. Figure 6.3 shows the experimental data obtained for the aspect ratios and volume parameters of both species as a function of the magnetic field. Interaction effects are observed in a range with a total width of the order of 100 mG. Deep hydrodynamic behavior, however, shows up only in a narrow range within the 30 mG wide regime of strong interactions where $k_F^{\mathrm{Li}}|a| > 1$. The observed magnetic-field dependence also points to interaction effects beyond elastic scattering. In the mean-field regime, the interaction is repulsive below resonance and attractive above resonance, which leads to a respective increase or decrease of the cloud size. The corresponding dispersive behavior indeed shows up in our measurements of V_{Li}. As another interaction effect, the maximum of the volume parameter V_{K} displays a shift towards lower magnetic fields with respect to both the resonance position and the maximum observed for the aspect ratio. We speculate that this shift may be related to the magnetic-field dependence of the interaction energy in the strongly interacting regime.

Let us now turn our attention to another striking manifestation of the hydrodynamic drag effect, a bimodality in the spatial distribution of the expanding Li cloud. In the trap center, the Li atoms spatially overlap with the K cloud (see Fig. 6.1). This inner part can, together

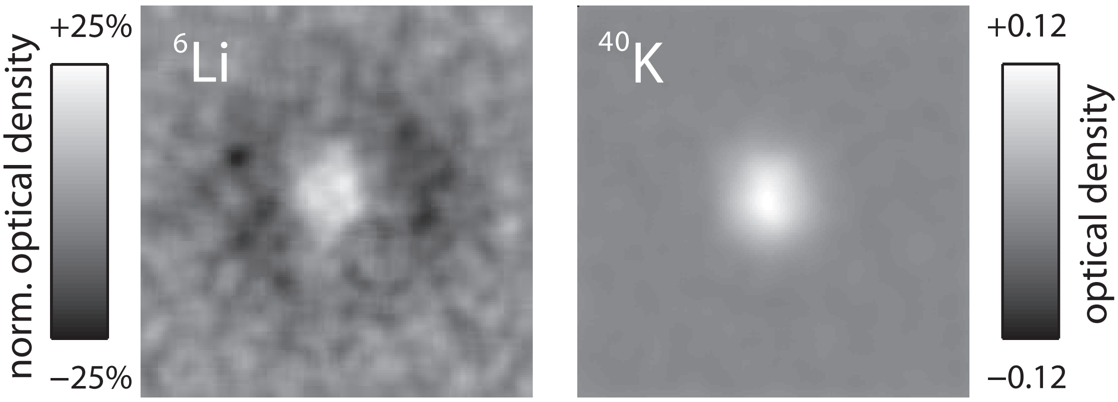

Figure 6.4: Images of the hydrodynamic core of the cloud ($t_{\mathrm{TOF}} = 4\,\mathrm{ms}$) in the regime of resonantly tuned interactions (154.706 G), where ^{6}Li and ^{40}K expand collectively. The image on the left-hand side is a differential image of the Li atoms, where we subtracted a reference image of the noninteracting cloud. The corresponding greyscale refers to the optical density as normalized to the maximum in the noninteracting distribution. The image on the right-hand side shows the K atoms in the strongly interacting cloud. Here the greyscale gives the optical density. The field of view of both images is $500\,\mu\mathrm{m} \times 500\,\mu\mathrm{m}$. The images are averaged over seven individual shots.

with the K atoms, form a hydrodynamic core, which is surrounded by a large noninteracting cloud of excess Li atoms. In this core, multiple elastic collisions prevent the two species from separating. This leads to a slow collective expansion of the light Li atoms sticking together with the much heavier K atoms. In contrast, the expansion of the outer part of the cloud is fast and proceeds in an essentially ballistic way[4].

Figure 6.4 shows images of the hydrodynamic core. To increase its visibility on the background of the ballistically expanding particles we show a differential Li image, where a reference image taken under noninteracting conditions is subtracted from the image of the strongly interacting cloud. This Li image is compared with a standard absorption image of the K cloud, as all K atoms are expected to contribute to the hydrodynamic core. The inner distribution detected for the Li component closely resembles the shape and size of the K cloud, supporting our interpretation of a jointly expanding Li-K cloud. The formation of this hydrodynamic core implies that particles are missing in the outer part, which undergoes a near-ballistic expansion[4]. Consequently, the differential Li image shows a negative signal in the outer region.

We analyze the bimodal distribution of the Li cloud by two-dimensional double-Gaussian fits. Two examples for the corresponding spatial profiles are shown in the upper panels of Fig. 6.5. The lower panel displays the fraction of Li atoms in the hydrodynamic core that we find from such fits as a function of the magnetic field. The maximum core fraction near 20% contains about 1.5×10^4 Li atoms, which corresponds to essentially all Li atoms in the overlap region. The maximum in the core fraction of Li near 154.7 G may be interpreted in

[4]During the expansion some atoms in the outer cloud can interact with the hydrodynamic core, which also makes their distribution anisotropic.

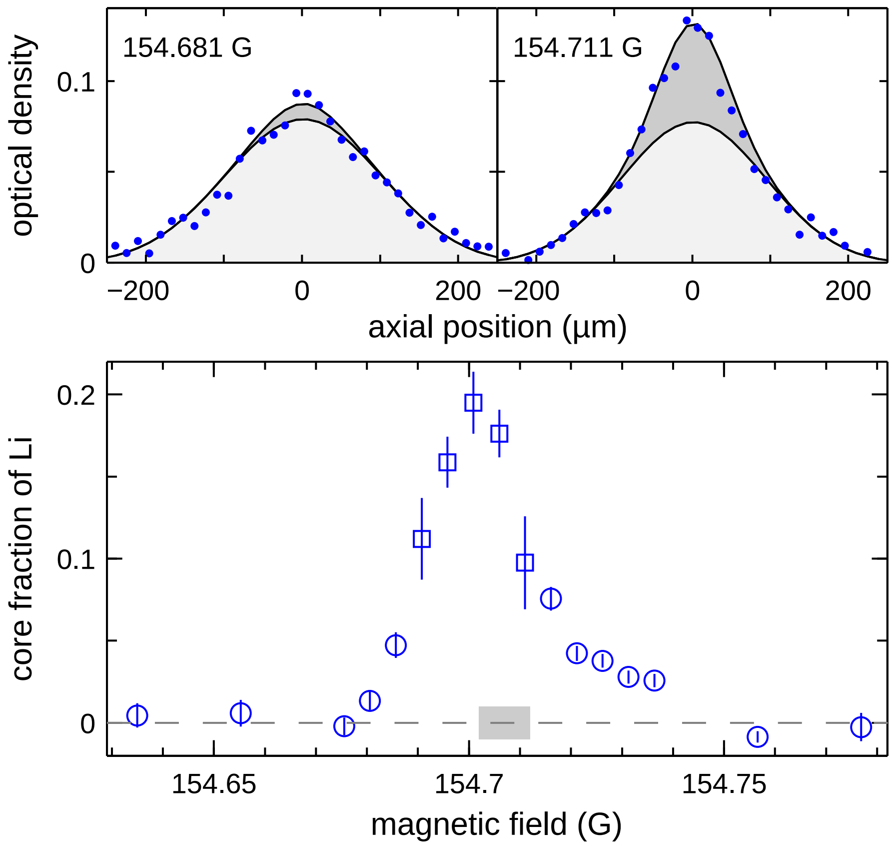

Figure 6.5: Bimodal distributions of ^{6}Li observed at $t_{\mathrm{TOF}} = 4\,\mathrm{ms}$. The upper panels show two example profiles representing axial cuts through the two-dimensional distribution, obtained from a narrow strip of 15 μm width in radial direction. The solid lines show double-Gaussian fits. The lower panel shows the corresponding fraction of atoms in the hydrodynamic core as a function of the magnetic field. The central five points (open squares) are based on fits where the widths of the core were kept as free parameters. Further away from resonance (open circles) the bimodality is much less pronounced and such a multiparameter fit is not applicable. Here the widths were fixed to corresponding widths of the K distribution. The error bars indicate the statistical uncertainties resulting form seven individual measurements at a given magnetic field. The grey shaded area indicates the uncertainty range for the resonance center according to Ref. [Nai11].

terms of a maximum collision cross section, thus marking the exact resonance position B_0, but it may also point to interaction phenomena beyond elastic scattering.

The physics of interactions in the strongly interacting regime can be very rich, and more detailed investigations on the hydrodynamic core will unravel the complex many-body interactions of the system. Besides mean-field shifts, for which we have already observed indications, strong polaronic interactions [Sch09b] or a substantial influence of pairing may be expected at sufficiently low temperatures. On the $a > 0$ side, weakly bound dimers [Voi09, Spi10b] may be formed either directly by radio-frequency association or indirectly by three-body recombination. We may speculate that on resonance, already at the moderate degeneracies realized in our present experiments, many-body pairs may contribute. Superfluidity may be expected at lower temperatures. All these phenomena need further detailed investigations and represent exciting future research topics.

In conclusion, we have explored a strongly interacting Fermi-Fermi mixture by studying its expansion dynamics. Our results show pronounced effects of hydrodynamic behavior, manifested in both an anisotropic expansion and in collective flow as resulting from interspecies drag. Our near-future work will be dedicated to a better understanding of the role of interaction effects, in particular, to the equation of state at unitarity [Gez09], and to the equilibrium and dynamics in the trap [Ors08]. The novel system offers many more intriguing possibilities to explore its quantum many-body physics. Already the experiments on strongly interacting spin mixtures [Ing08b, Gio08] suggest a rich tool box of different experimental methods, such as measurements on *in situ* spatial profiles, studies of collective modes, the application of radio-frequency or Bragg spectroscopy, and detection of molecular condensates and fermionic pair condensates. Moreover, the Fermi-Fermi mixture offers conceptually new possibilities through the application of species-selective optical potentials, which will allow for independent control of both components, e.g., for an independent manipulation of the Fermi surfaces in optical lattices [Fei09] or for the creation of mixed-dimensional fermionic systems [Nis08].

We thank A. Recati, S. Giorgini, and S. Stringari for stimulating discussions and G. Hendl for technical assistance. We acknowledge support by the Austrian Science Fund (FWF) and the European Science Foundation (ESF) within the EuroQUAM/FerMix project and support by the FWF through the SFB FoQuS.

Note

Note that the value given for B_0 refers to the particular optical trap used in the experiments. It includes a small shift induced by the trapping light, as the molecules have slightly different polarizabilities than the free atoms, leading to a difference in the Stark shift. In free space, without the light shift, the resonance center is located at 154.698(5) G, see also Methods in Chap.7.

CHAPTER 7

PREPRINT

Metastability and coherence of repulsive polarons in a strongly interacting Fermi mixture [1]

submitted (2011)

C. Kohstall,[1,2] M. Zaccanti,[1] M. Jag,[1] A. Trenkwalder,[1] P. Massignan,[3] G. M. Bruun,[4] F. Schreck,[1] and R. Grimm[1,2]

[1] *Institut für Quantenoptik und Quanteninformation, Österreichische Akademie der Wissenschaften, 6020 Innsbruck, Austria*
[2] *Institut für Experimentalphysik, Universität Innsbruck, 6020 Innsbruck, Austria*
[3] *ICFO - Institut de Ciències Fotòniques, Mediterranean Technology Park, 08860 Castelldefels (Barcelona), Spain*
[4] *Department of Physics and Astronomy, University of Aarhus, 8000 Aarhus C, Denmark*

[1] The author of the present thesis developed the experimental procedures, performed the measurements and analyzed the data together with M.Z., M.J., and A.T. The theoretical calculations of this publication were contributed by P.M. and G.M.B.

Ultracold Fermi gases with tuneable interactions represent a unique test bed to explore the many-body physics of strongly interacting quantum systems [Blo08b, Gio08, Rad10, Che10]. In the past decade, experiments have investigated a wealth of intriguing phenomena, and precise measurements of ground-state properties have provided exquisite benchmarks for the development of elaborate theoretical descriptions. Metastable states in Fermi gases with strong repulsive interactions [Dui05, LeB09, Con09, Jo09, Pil10, Cha11, San11] represent an exciting new frontier in the field. The realization of such systems constitutes a major challenge since a strong repulsive interaction in an atomic quantum gas implies the existence of a weakly bound molecular state, which makes the system intrinsically unstable against decay. Here, we exploit radio-frequency spectroscopy to measure the complete excitation spectrum of fermionic ^{40}K impurities resonantly interacting with a Fermi sea of ^{6}Li atoms. In particular, we show that a well-defined quasiparticle exists for strongly repulsive interactions. For this “repulsive polaron” [Pil10, Mas11, Sch11] we measure its energy and its lifetime against decay. We also probe its coherence properties by measuring the quasiparticle residue. The results are well described by a theoretical approach that takes into account the finite effective range of the interaction in our system. We find that a non-zero range of the order of the interparticle spacing results in a substantial lifetime increase. This major benefit for the stability of the repulsive branch opens up new perspectives for investigating novel phenomena in metastable, repulsively interacting fermion systems.

7.1 Main results

Landau’s theory of a Fermi liquid [Lan57] and the underlying concept of quasiparticles lay at the heart of our understanding of interacting Fermi systems over a wide range of energy scales, including liquid ^{3}He, electrons in metals, atomic nuclei, and the quark-gluon plasma. In the field of ultracold Fermi gases, the normal (non-superfluid) phase of a strongly interacting system can be interpreted in terms of a Fermi liquid [Lob06, Sch09b, Nav10, Nas11]. In the population-imbalanced case, quasiparticles coined Fermi polarons are the essential building blocks and have been studied in detail experimentally [Sch09b] for attractive interactions. Recent theoretical work [Pil10, Mas11, Sch11] has suggested a novel quasiparticle associated with *repulsive* interactions. The properties of this repulsive polaron are of fundamental importance for the prospects of repulsive many-body states. A crucial question for the feasibility of future experiments is the stability against decay into molecular excitations [Pek11a, Mas11, San11]. Indeed, whenever a strongly repulsive interaction is realized by means of a Feshbach resonance [Chi10], a weakly bound molecular state is present into which the system may rapidly decay.

Our system consists of impurities of fermionic ^{40}K atoms immersed in a large Fermi sea of ^{6}Li atoms, which is characterised by a Fermi energy $\epsilon_F = h \times 37\,\mathrm{kHz}$ and a temperature $T = 0.16\,\epsilon_F/k_B$ (see Methods), with h and k_B denoting Planck’s and Boltzmann’s constants. In a particular combination of spin states [Nai11], the ^{6}Li -^{40}K mixture features a Feshbach resonance centered at $B_0 = 154.719(2)\,\mathrm{G}$. The resonance allows to widely tune the s-wave interaction, parametrised by the scattering length a, via a magnetic field B. The interaction

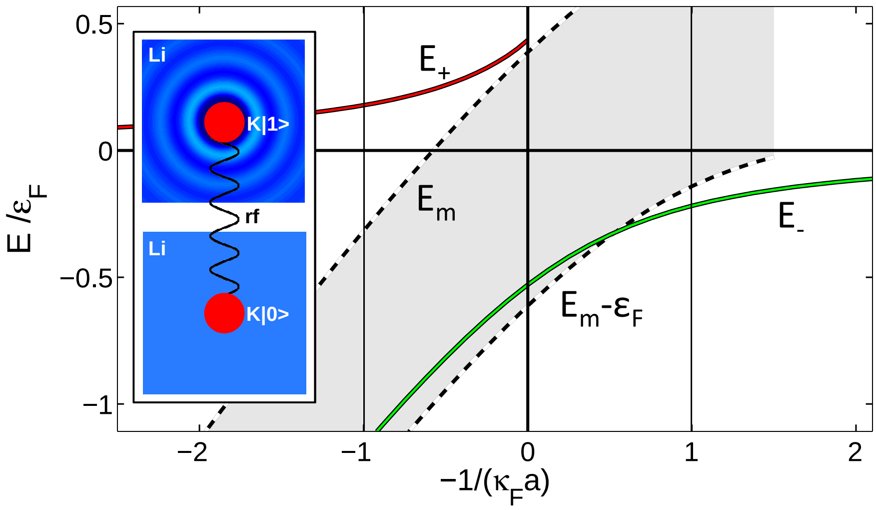

Figure 7.1: **Energy spectrum of the impurity in the Fermi sea.** For the two polaronic branches, the energies E_+ (red line) and E_- (green line) are plotted as a function of the interaction parameter $-1/(\kappa_F a)$. The shaded area between the dashed lines representing E_m and $E_m - \epsilon_F$ (see text) shows the continuum of molecular excitations. The vertical lines at $1/(\kappa_F a) = \pm 1$ indicate the width of the strongly interacting regime. The inset illustrates our rf spectroscopic scheme where the impurity is transferred from a noninteracting spin state $|0\rangle$ to the interacting state $|1\rangle$.

strength is described by the dimensionless parameter $-1/(\kappa_F a)$, where $\kappa_F = \hbar^{-1}\sqrt{2m_{\mathrm{Li}}\epsilon_F} = 1/(2850\, a_0)$ is the Fermi wave number; here $\hbar = h/2\pi$, a_0 is Bohr's radius, and m_{Li} is the mass of a ^{6}Li atom. Near the resonance center, the linear approximation $-1/(\kappa_F a) = (B - B_0)/20\,\mathrm{mG}$ holds. The momentum dependence of the interaction is characterised by the effective range, which we express in terms of the parameter [Pet04a] $R^* = 2700\, a_0$ (see Supplementary Information).

Figure 7.1 illustrates the basic physics of our impurity problem in the $T = 0$ limit, showing the energies of different states as a function of the interaction parameter. The situation is generic for any impurity in a Fermi sea, but quantitative details depend on both the mass ratio and the particular width of the Feshbach resonance. The theoretical curves are based on an extension of an approach presented in Refs. [Pun09, Mas11] to our case of a relatively narrow Feshbach resonance with $\kappa_F R^* = 0.95$ and thus a considerable effective range of the interaction (see Supplementary Information).

The spectrum exhibits two quasiparticle branches, which do not adiabatically connect when the resonance is crossed, and a molecule-hole continuum (MHC). The interaction-induced energy shifts of the two branches ($E_+ > 0$ and $E_- < 0$) are generally described in a many-body picture by dressing the impurities with particle-hole excitations. Far away from resonance this simplifies to a mean-field shift proportional to a. The lower branch E_- of the system (green line) corresponds to the *attractive polaron*, which has recently received a great deal of attention theoretically [Che10, Lob06, Com07, Pun09, Sad11] as well as experimentally [Nas09b, Sch09b, Nav10]. This polaronic branch remains the ground state of the system until a critical interaction strength is reached, where the system energetically prefers to form a bosonic molecule by binding the impurity to an atom taken from the Fermi sea [Pro08, Pun09, Sad11]. The continuum arises from the fact that a majority atom with an energy between 0 and ϵ_F can be removed from the Fermi sea to form the molecule. The MHC thus exists in an energy range between E_m and $E_m - \epsilon_F$ (dashed lines in Fig. 7.1), where E_m represents the energy of a dressed molecule including the binding energy of a bare molecule in vacuum and a positive interaction shift. The attractive polaron can decay into a molecular excitation if this channel opens up energetically ($E_- \geq E_m - \epsilon_F$).

The upper branch (red line in Fig. 7.1) corresponds to the *repulsive polaron* [Pil10, Mas11, Sch11] with an energy $E_+ > 0$. Approaching the resonance from the $a > 0$ side, E_+ gradually increases and reaches a sizeable fraction of ϵ_F. However, the polaronic state becomes increasingly unstable as it decays to the lower lying states (attractive polaron and MHC). Close to the resonance center, the polaronic state becomes ill-defined as the decay rate approaches $E_+/\hbar$.

To investigate the excitation spectrum of the impurities, we employ radio-frequency (rf) spectroscopy [Chi04, Shi07, Ste08]. We initially prepare the ^{40}K atoms in a non-interacting spin state $|0\rangle$ and then, with a variable frequency ν_{rf}, drive rf transitions into the resonantly interacting state $|1\rangle$. Our signal is the fraction of atoms transferred, measured as a function of the rf detuning $\nu_{\mathrm{rf}} - \nu_0$ with respect to the unperturbed transition frequency ν_0 between the two spin states. This excitation scheme provides access to the full energy spectrum of the system. In particular, it allows us to probe the metastable repulsive polaron as well as all states in the MHC. We furthermore take advantage of the *coherence* of the excitation process by driving Rabi oscillations. As an important practical advantage, this enables very fast and efficient transfer of population into a short-lived quasiparticle state by application of π-pulses. Moreover, we will show that measurements of the Rabi frequency directly reveal quasiparticle properties.

In Fig. 7.2 we show false-colour plots of our signal, detected for different values of the detuning parameter $\Delta = h(\nu_{\mathrm{rf}} - \nu_0)$ and for variable interaction strength $-1/(\kappa_F a)$. Figure 7.2a displays a set of measurements that was optimised for signal and spectral resolution of the polaronic excitations by using moderate rf power (see Methods). The spectrum in Fig. 7.2b was optimised for detection of the molecular excitations. Here a much higher rf power had to be employed because of the reduced Franck-Condon wavefunction overlap. For the polaronic branches the high rf power leads to a highly nonlinear saturation behaviour.

Our data clearly show *both* polaronic branches, with their measured energies being in excellent agreement with theory. The attractive polaron is found to disappear in the strongly interacting regime. This behaviour, which is different from the one observed for ^{6}Li spin mixtures [Sch09b], is consistent with the crossing of E_- and $E_m - \epsilon_F$ at $-1/(\kappa_F a) \approx +0.6$ predicted for our system. In contrast, the repulsive polaron extends far into the strongly interacting regime. A sharp peak is observed in the spectrum with decreasing signal strength until it finally fades out very close to resonance at $-1/(\kappa_F a) \simeq -0.3$ (see Supplementary Information). The low rf power only produces a weak signal for the MHC, whereas the high rf power clearly unveils the presence of the MHC. Further on the $a > 0$ side of the resonance, the molecular signal gets weaker because of the decreasing Franck-Condon overlap, and outside of the strongly interacting regime the situation corresponds to the rf association of

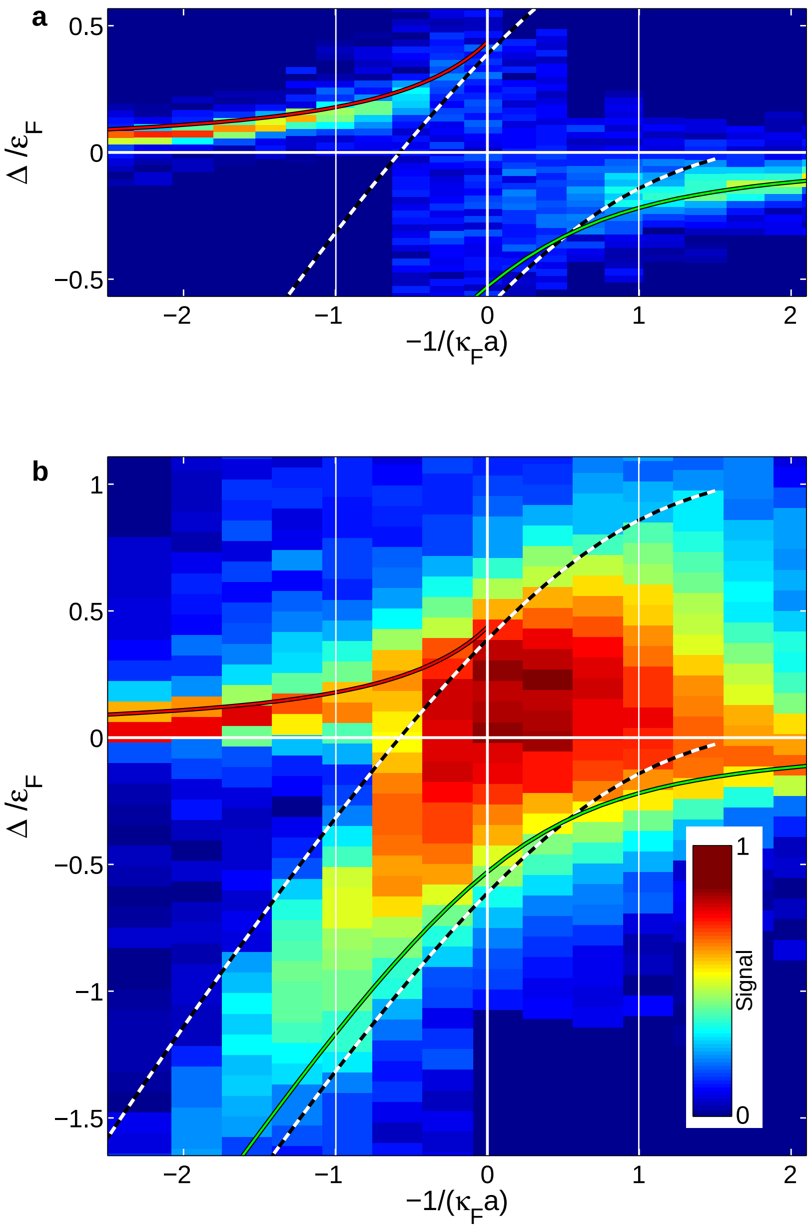

Figure 7.2: **Spectral response of ^{40}K impurities in a ^{6}Li Fermi sea.** The false-colour plots show the fraction of ^{40}K atoms transferred from the non-interacting spin state $|0\rangle$ into the interacting state $|1\rangle$ for different values of the rf detuning parameter $\Delta = h(\nu_{\mathrm{rf}} - \nu_0)$ and for variable interaction strength $-1/(\kappa_F a)$. The panels **a** and **b** refer to low and high rf power. For comparison, the lines correspond to the theoretical predictions for E_+, E_-, E_m, and $E_m - \epsilon_F$ as shown in Fig. 1.

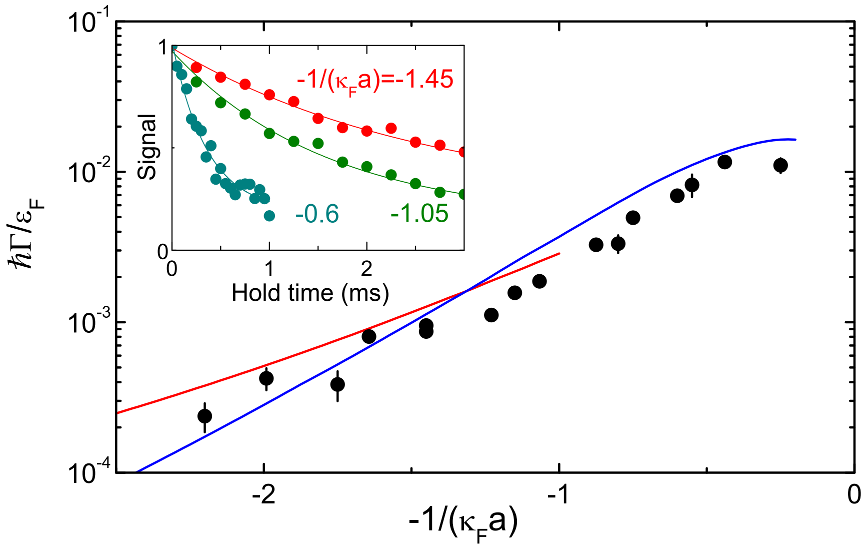

Figure 7.3: **Decay rate of the repulsive polaron.** The data points display the measured decay rates Γ as extracted by exponential fits from decay curves; the error bars indicate the fit uncertainties. Sample decay curves are shown in the inset. The solid lines represent theoretical calculations of the two-body decay (blue line) and the three-body decay (red line) into the attractive polaron or the MHC, respectively.

bare molecules (see Supplementary Information).

To investigate the decay of the repulsive branch, we apply an rf pulse sequence to selectively convert repulsive polarons back into non-interacting impurities after a variable hold time (see Methods). The back conversion sensitively depends on the rf resonance condition and thus allows us to discriminate ^{40}K atoms in the polaronic state against those ones forming molecules. Figure 7.3 presents the experimental results. The inset shows three sample curves, taken for different values of the interaction parameter. The main panel displays the values extracted for the decay rate Γ from the decay curves by simple exponential fits. The data reveal a pronounced increase of decay as the resonance is approached, which is in good agreement with theoretical model calculations [Mas11] (see Supplementary Information). The decay populates the MHC and may happen in a two-step process where the repulsive polaron first decays via a two-body process into an attractive polaron (blue line) and then decays into a molecular excitation. Alternatively, a three-body process may directly lead into the MHC (red line). Very close to the resonance, for $-1/(\kappa_F a) = -0.25$, we find $\hbar\Gamma/\epsilon_F \approx 0.01$, which corresponds to a $1/e$ lifetime of about $400\,\mu$s. Relating this decay rate to the corresponding energy shift $E_+ = 0.30\,\epsilon_F$, we obtain $\hbar\Gamma/E_+ \approx 0.03 \ll 1$, which demonstrates that the repulsive polaron exists as a well resolved, metastable quasiparticle even deep in the strongly interacting regime.

The lifetime observed for the repulsive branch appears to be remarkably long, when compared to recent experiments on ^{6}Li spin mixtures [San11]. The latter system is a mass-balanced one and it features a broad Feshbach resonance with a negligible effective range. Our theoretical approach allows to answer in a general way the question how mass imbal-

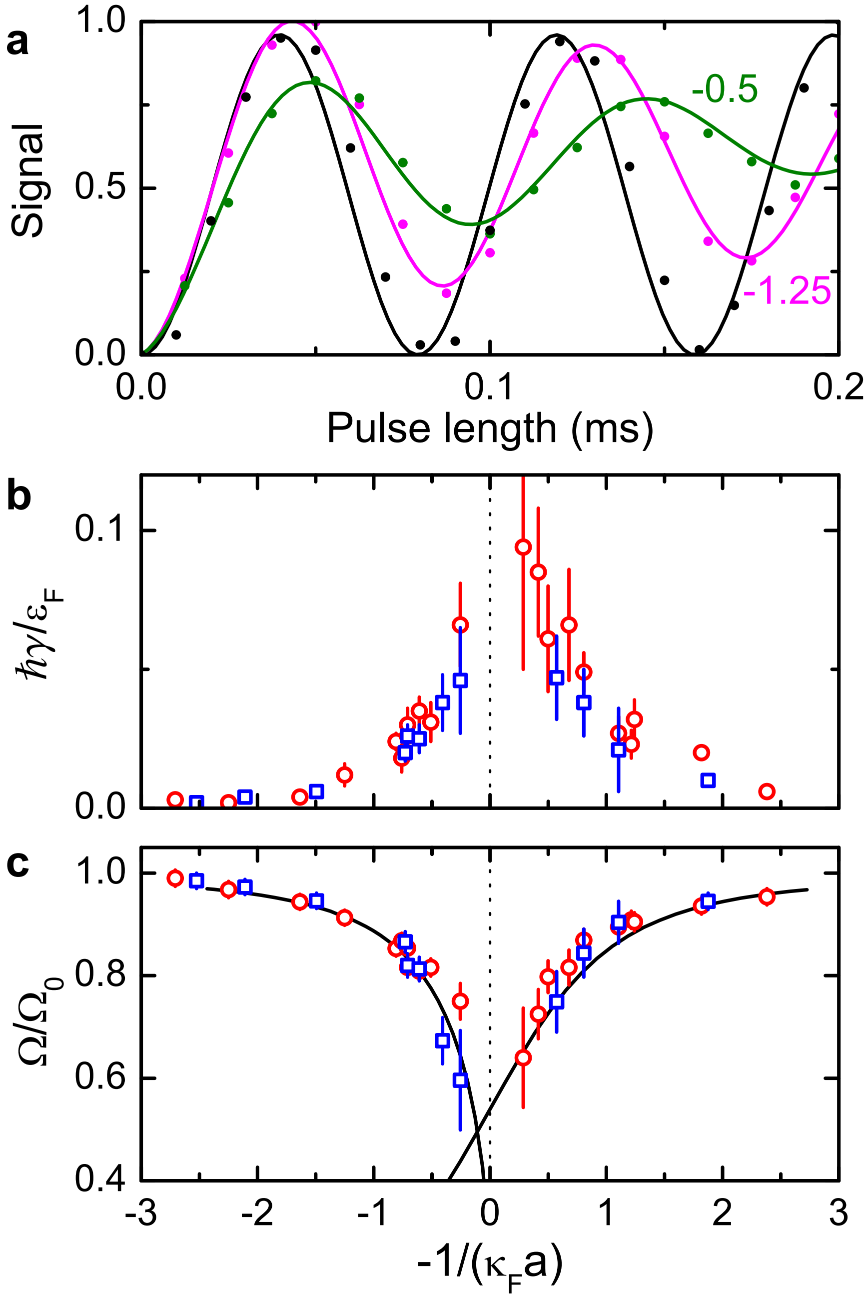

Figure 7.4: **Rabi oscillations and the quasiparticle residue. a**, Sample Rabi oscillations (magenta and green data points for $-1/(\kappa_F a) = -1.25$ and -0.5, respectively) with harmonic oscillator fits (solid lines) demonstrate the two effects of the interaction with the Fermi sea: damping and a reduction of the Rabi frequency. The black curve is a reference curve recorded without ^{6}Li . In **b** and **c**, the data points show the damping rates γ and the normalized Rabi frequencies Ω/Ω_0 as measured for two different values of the rf power; the blue squares and red dots refer to $\Omega_0 = 2\pi \times 6.5\,\mathrm{kHz}$ and $12.6\,\mathrm{kHz}$, respectively. The error bars indicate the fit uncertainties. The solid lines represent the theoretical behavior of $\sqrt{Z}$ for the repulsive and the attractive polaron.

ance and the width of the resonance influence the lifetime. We find that, while the mass imbalance does only play a minor role [Mas11], the dominant effect results from the finite effective range, which is associated with the narrow character of the Feshbach resonance that we exploit. Comparing our situation with a hypothetical system with a broad Feshbach resonance, and thus with a zero-range interaction, we find that in the strongly interacting regime the same amount of energy can be obtained with an almost ten times increased lifetime (see Supplementary Information).

Besides energy and lifetime, the polaron is characterized by its effective mass m^* and its quasiparticle residue Z. The difference between effective and bare mass [Mas11] does not produce any significant features in our rf spectra. The residue Z ($0 \leq Z \leq 1$) quantifies how much of the non-interacting particle is contained in the polaron's wavefunction, which can be written as $\sqrt{Z}\,|1\rangle$ plus terms describing excitations in the Fermi sea. The pre-factor $\sqrt{Z}$ directly manifests itself in the Rabi frequency Ω that describes the coherent rf coupling between the noninteracting and the polaronic state (see Supplementary Information).

Figure 7.4 presents the experimental data on Rabi oscillations for variable interaction strength. The sample curves in Fig. 7.4a demonstrate both the interaction-induced change in the frequency and a damping effect. We apply a simple harmonic oscillator model (including a small increasing background) to analyse the curves, which yields the damping rate γ and the frequency Ω. The damping strongly increases close to the resonance center, but does not show any significant dependence on Ω_0, see Fig. 7.4b. It is interesting to note that the population decay rates Γ measured for the repulsive branch (Fig. 7.3) stay well below the values of γ, which points to collision-induced decoherence as the main damping mechanism.

Figure 7.4c displays the measured values for the Rabi frequency Ω, normalized to the unperturbed value Ω_0. The interaction-induced reduction of Ω/Ω_0 is found to be independent of the particular value of Ω_0 (comparison of blue squares and red dots; see also Supplementary Information). The solid lines show $\sqrt{Z}$ as calculated within our theoretical approach for both the repulsive and the attractive polaron. The comparison with the experimental data demonstrates a remarkable agreement with the relation $\sqrt{Z} = \Omega/\Omega_0$. Our results therefore suggest measurements of the Rabi frequency as a precise and robust method to determine the quasiparticle residue Z, and thus provides a powerful alternative to methods based on the detection of the narrow quasiparticle peak in the spectral response [Sch09b, Pun09].

In conclusion, we have realized an ultracold model system of ^{40}K and ^{6}Li atoms to investigate the quasiparticle behavior of heavy impurities resonantly interacting with a Fermi sea of light particles. Our spectroscopic approach has confirmed the existence of the predicted repulsive branch [Pil10, Mas11, Sch11] and has demonstrated that the repulsive polaron can exist as a well-defined quasiparticle even deep in the strongly interacting regime. The long lifetime of the repulsive polaron in our system, which we ascribe to the finite effective range of the interparticle interaction, may be a key factor to overcome the problem of decay into molecular excitations [Pek11a, San11] in the experimental investigation of metastable many-body states that rely on repulsive interactions. In particular, the creation of states with two fermionic components phase-separating on microscopic or macroscopic scales [Dui05, LeB09, Con09, Jo09, Cha11, San11] appears to be an intriguing near-future prospect.

Acknowledgements. We thank A. Sidorov for contributions in the early stage of the experiments, and T. Enss, S. Giorgini, W. Ketterle, J. Levinsen, C. Lobo, D. Petrov, A. Recati,

R. Schmidt, J. Song, C. Trefzger, P. Zoller, W. Zwerger, M. Zwierlein, and in particular M. Baranov for many stimulating discussions. We acknowledge support by the Austrian Science Fund FWF through the SFB FoQuS. M.Z. is supported within the Lise Meitner program of the FWF. P.M. is indebted to M. Lewenstein for support through the ERC Advanced Grant QUAGATUA.

7.2 Methods

Experimental conditions. Our system consists of 2×10^4 ^{40}K atoms and 3.5×10^5 ^{6}Li atoms confined in an optical dipole trap. The trap is realized with two crossed beams derived from a 1064 nm single-mode laser source. The measured trap frequencies for Li (K) are $\nu_r =$ 690 Hz (425 Hz) radially and $\nu_z = 86$ Hz (52 Hz) axially; this corresponds to a cigar-shaped sample with an aspect ratio of about 8. The preparation procedure is described in detail in Ref. [Spi10a]. The Fermi energies, according to the common definition $E_F = h\sqrt[3]{6N\nu_r^2\nu_z}$ for harmonic traps, are $E_F^{\mathrm{Li}} = h \times 44\,\mathrm{kHz} = k_B \times 2.1\,\mu\mathrm{K}$ and $E_F^{\mathrm{K}} = h \times 10.4\,\mathrm{kHz} = k_B \times 500\,\mathrm{nK}$. At a temperature $T \approx 290\,\mathrm{nK}$ the ^{6}Li component forms a deeply degenerate Fermi sea ($k_BT/E_F^{\mathrm{Li}} \approx 0.14$) while the ^{40}K component is moderately degenerate ($k_BT/E_F^{\mathrm{K}} \approx 0.6$).

Effective Fermi energy. The ^{40}K atoms experience a nearly homogeneous ^{6}Li environment. This is because the optical trapping potential for ^{40}K is about 2 times deeper than for ^{6}Li and the ^{40}K cloud is confined in the center of the much larger ^{6}Li Fermi sea [Tre11b]. This allows us to describe the system in terms of the effective Fermi energy ϵ_F, defined as the mean Fermi energy experienced by the ^{40}K atoms. We find $\epsilon_F = h \times 37\,\mathrm{kHz}$, with two effects contributing to the fact that this value is about 15% below E_F^{Li}. The finite temperature reduces the Li density in the trap center, leading to a peak local Fermi energy of $h \times 40\,\mathrm{kHz}$. Moreover, the ^{40}K atoms sample a small region around the trap center, where the density and local Fermi energy are somewhat lower. The distribution of Fermi energies experienced by the ^{40}K cloud, i.e. the residual inhomogeneity of our system, can be quantified by a standard deviation of $h \times 1.9\,\mathrm{kHz}$.

Concentration. The mean impurity concentration (mean density ratio $n_{\mathrm{K}}/n_{\mathrm{Li}}$) is about 0.4, if one considers the population of K atoms in both spin states. This may be *a priori* too large to justify the interpretation of our data in terms of the low-concentration limit. We find that this interpretation is nevertheless valid, as we take advantage of several facts. Under strongly interacting conditions only a fraction of the K atoms is transferred into spin state $|1\rangle$ (see Fig. 7.2), which reduces the concentration of interacting impurities. A recent quantum Monte Carlo calculation of the equation of state of a zero-temperature ^{6}Li -^{40}K Fermi-Fermi mixture [Gez09] further supports our interpretation in the low-concentration limit: The strongest interaction in the mass-imbalanced system is expected when one has about 4 times more ^{40}K atoms than ^{6}Li atoms, and for concentrations up to a value of 1 the interaction energy per ^{40}K atom is expected to remain essentially constant. To support our basic assumption with experimental data, we also took rf spectra for variable numbers of ^{40}K atoms, confirming that in the relevant parameter range finite concentration effects remained negligibly small.

Interaction control via Feshbach resonance. The Feshbach resonance used for interaction tuning is discussed in detail in Refs. [Nai11, Tre11b]. It is present for ^{6}Li in the lowest spin state and ^{40}K in the third-to-lowest spin state. The latter represents our interacting state $|1\rangle$; the corresponding quantum numbers are $F = 9/2$ for the hyperfine and $m_F = -5/2$ for the magnetic sub-state. The neighboring state with $m_F = -7/2$ serves as state $|0\rangle$; here the interspecies scattering length (about $+65\,a_0$ with a_0 being Bohr's radius) is so small that it can be neglected to a good approximation. The tunable scattering length for state $|1\rangle$ in the Fermi sea is well described by the standard formula $a = a_{\mathrm{bg}}(1 - \Delta B/(B - B_0))$ with $a_{\mathrm{bg}} = 63.0\,a_0$, $\Delta B = 880\,\mathrm{mG}$, and $B_0 = 154.719(2)\,\mathrm{G}$. Note that the value given for B_0 refers to the particular optical trap used in the experiments, as it includes a small shift induced by the trapping light. The value therefore somewhat deviates from the one given in Refs. [Nai11, Tre11b]. In free space, without the light shift, the resonance center is located at 154.698(5) G. The character of the resonance is closed-channel dominated [Chi10]. Following the definition [Pet04a] of a range parameter $R^* = \hbar^2/(2m_r a_{\mathrm{bg}}\,\delta\mu\,\Delta B)$, with $m_r = m_{\mathrm{Li}}m_{\mathrm{K}}/(m_{\mathrm{Li}} + m_{\mathrm{K}})$ being the reduced mass and $\delta\mu$ the differential magnetic moment, the resonance is characterized by $R^* = 2700\,a_0$. This value accidentally lies very close to $1/\kappa_F = 2850\,a_0$, which also means that the strongly interacting regime roughly corresponds to the universal range of the resonance. Our system therefore represents an intermediate case ($\kappa_F R^* = 0.95$), where the behavior is near universal, but with significant effects arising from closed-channel contributions.

Details on Rf pulses. For taking the data of Fig. 7.2 we used Blackman pulses [Kas92] to avoid side lobes in the spectrum. For the upper panel, the pulses were 1 ms long (spectral width $0.7\,\mathrm{kHz} \simeq 0.02\,\epsilon_F/h$) and the rf power was adjusted such that π-pulses would be realized in the absence of interactions with the Fermi sea. For the data in the lower panel, the rf power was increased by a factor of 100 and the pulse duration was set to 0.5 ms. This resulted in pulses with an area of 5π without the Fermi sea. For the lifetime measurements in Fig. 7.3, we used a sequence of 3 Blackman pulses. The first pulse (duration between 150 μs and 500 μs) was set to drive the non-interacting impurity from spin state $|0\rangle$ ($m_F = -7/2$) into state $|1\rangle$ ($m_F = -5/2$); here the frequency was carefully set to resonantly create repulsive polarons and the pulse area was set to fulfill the π-pulse condition. The second pulse was a short (60 μs) cleaning pulse, which removed the population remaining in $|0\rangle$ by transfer to another, empty spin state ($m_F = -9/2$). The third pulse had the same parameters as the first one and resonantly back-transferred the population from the polaronic state in $|1\rangle$ to the non-interacting state $|0\rangle$, where it was finally measured by spin-state selective absorption imaging. The measurements of Rabi oscillations in Fig. 7.4 were performed with simple square pulses.

7.3 Supplementary information

7.3.1 Theoretical framework

The theoretical results presented in the main text and in this Supplementary Information are obtained from a model that describes the behaviour of a single impurity embedded in a Fermi sea with tuneable s-wave interaction near a Feshbach resonance with arbitrary effective range. Two different wavefunctions are needed, depending on whether one is interested in the polaron [Che06, Com07] or molecule [Mor09, Pun09, Com09] properties. The quasiparticle parameters for the polaron (energy E_+ and E_-, residue Z, effective mass) and the molecule properties can be found either variationally, or diagrammatically using the ladder approximation. Both approaches yield identical results, which closely match independent Monte-Carlo calculations [Pro08]. The properties of the repulsive polaron, which is intrinsically unstable due to the presence of the molecule-hole continuum (MHC) and of the attractive polaron, are obtained from the self energy. In particular, the interaction induced energy shift and the decay rate are given by the real part and twice the imaginary part of the self energy, respectively [Mas11].

Previous treatments [Che06, Com07, Mor09, Pun09, Com09, Pro08, Mas11] were based on a universal scattering amplitude, describing broad Feshbach resonances. To include effects of the finite effective range we employ a many-body T-matrix given by [Bru05, Mas08b]

$$T(\mathbf{K},\omega) = \left[\frac{m_r}{2\pi\hbar^2\tilde{a}(\mathbf{K},\omega)} - \Pi(\mathbf{K},\omega)\right]^{-1}. \tag{7.1}$$

Here $\hbar\mathbf{K} = \mathbf{p}_{\mathrm{K}} + \mathbf{p}_{\mathrm{Li}}$ is the total momentum with $\mathbf{p}_{\mathrm{Li}}$ and $\mathbf{p}_{\mathrm{K}}$ the momenta of ^{6}Li and ^{40}K, $m_r = m_{\mathrm{Li}}m_{\mathrm{K}}/(m_{\mathrm{Li}} + m_{\mathrm{K}})$ the reduced mass, $\Pi(K,\omega)$ the ^{6}Li -^{40}K pair propagator in the presence of the Fermi sea, and $\tilde{a}(\mathbf{K},\omega) \equiv a_{\mathrm{bg}}\left(1 - \frac{\Delta B}{B-B_0-E_{\mathrm{CM}}/\delta\mu}\right)$ an energy-dependent length parameter, with a_{bg}, ΔB, B_0, and $\delta\mu$ being the background scattering length, the width, the center, and the relative magnetic moment of the Feshbach resonance. $E_{\mathrm{CM}}(\mathbf{K},\omega) = \hbar\omega - \hbar^2\mathbf{K}^2/(2M) + \epsilon_F$, with $M = m_{\mathrm{Li}} + m_{\mathrm{K}}$, is the energy in the center of mass reference frame of the colliding pair. In vacuum and close to resonance, the scattering amplitude of our model has the usual low energy expansion

$$-f_k^{-1} = a^{-1} + ik - r_e k^2/2 + \ldots, \tag{7.2}$$

with the relative momentum $\hbar\mathbf{k} = (m_{\mathrm{Li}}\mathbf{p}_{\mathrm{K}} - m_{\mathrm{K}}\mathbf{p}_{\mathrm{Li}})/M$. The effective range is approximated by $r_e \approx -2R^*(1-a_{\mathrm{bg}}/a)^2$, where we introduce the range parameter $R^* = \hbar^2/(2m_r a_{\mathrm{bg}}\Delta B\delta\mu)$, see Ref. [Pet04a]. A detailed theoretical analysis of this model will be given elsewhere [Mas].

7.3.2 Polaron peak in the spectral response

The spectra in Fig. 7.2a of the main text show a narrow, *coherent* peak on top of a spectrally broad, *incoherent* background. Here, we investigate these two spectral parts in more detail. Note that the background is actually better visible in Fig. 7.2b, but these spectra do not allow for a quantitative comparison of the two parts because of the strong saturation of the narrow polaron peaks.

The narrow peak stems from the attractive or repulsive polarons, which correspond to well defined energy levels, provided that the lifetime of the quasiparticle exceeds the pulse duration. As a consequence, the lineshape is expected to be Fourier limited except for the rapidly decaying repulsive polarons very close to resonance. In contrast, the background is spectrally wide, on the order of ε_F. The main contribution to the background stems from the MHC. Another contribution may arise from the excitation of additional particle-hole pairs

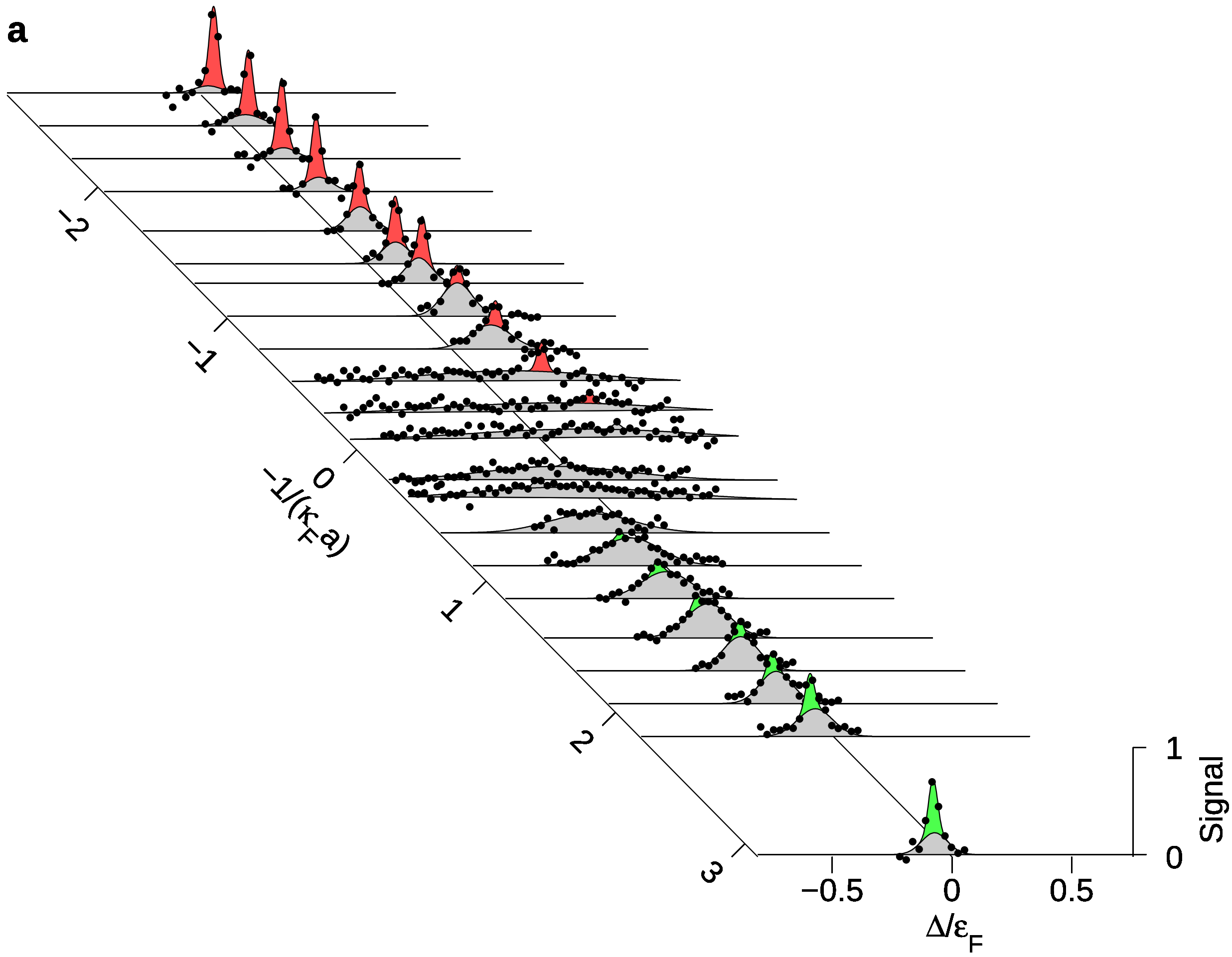

Figure 7.5: See figure caption below.

in the Fermi sea when transferring to a quasiparticle with a momentum that is different from the momentum of the impurity in the initial state.

We distinguish between the narrow peak and the wide background by means of a double Gauss fit. Vertical cuts through Fig. 7.2a are presented in Fig. 7.5a together with the fit curves. The width σ_p of the Gauss function fitting the narrow peak is fixed to the one associated with the Gaussian fit of the Blackman pulse line shape used in the experiment, $\sigma_p = 0.7\,\text{kHz} = 0.019\,\varepsilon_F/h$. We constrain the width σ_b of the Gauss function reproducing the background to $3\times0.019\,\varepsilon_F/h < \sigma_b < 0.5\,\varepsilon_F/h$. The lower bound avoids the misinterpretation of the narrow peak as background and the upper bound, corresponding to the maximal width of the continuum as obtained from the spectra in Fig. 7.2b, avoids unphysically large values of σ_b when the background signal is weak. We find that the narrow peak dominates for weak positive and negative interaction strength while the wide background dominates in the strongly interacting regime. This trend is shown in Fig. 7.5b and Fig. 7.5c, where we present the maximum signal of the narrow peak and the area of the background, respectively. Note that the signal in Fig. 7.5b is proportional to the area of the narrow peak since σ_p is

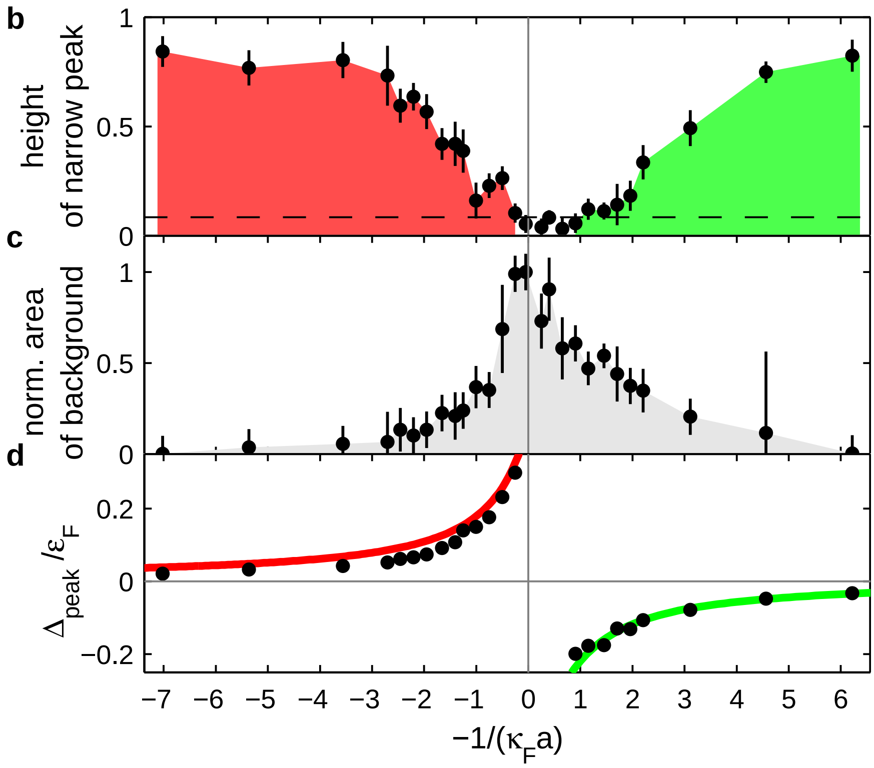

Figure 7.5: Double Gauss analysis of the low-power spectra. The data are the same as presented in Fig. 2a plus additional data in an extended range of $1/(\kappa_F a)$. (a) The Gauss function fitting the wide background is shaded grey. The Fourier-limited Gauss function, fitting the narrow peak, is coloured red (green) along the repulsive (attractive) polaron branch. We identify the narrow peak with one of the polaron branches only if its maximum signal exceeds a threshold value of 0.085, corresponding to two times the standard deviation of the noise in our data. Any smaller peak may be caused by fitting to a noise component. The lower panels show (b) the maximum signal of the narrow peak with the dashed line indicating the threshold, (c) the area under the wide Gauss function normalized to its maximum value, and (d) the detuning at the center of the narrow peak, provided that the peak signal exceeds the threshold, compared to the theoretical calculation of E_+ and E_- (red and green line). The error bars indicate the fit uncertainties.

kept constant. Figure 7.5d shows the detuning at the center of the narrow peak, which corresponds to the energy of the quasiparticles. The measured energies agree remarkably well with the calculation. The slight mismatch between theory and experiment may be attributed to systematic errors in the determination of ε_F and B_0.

The area of the wide background exhibits a maximum close to $-1/(\kappa_F a) = 0$, but it shows an asymmetry as it falls off significantly slower on the attractive ($a < 0$) side, see

Fig. 7.5c. We attribute this asymmetry to the narrow character of the Feshbach resonance. The interaction becomes resonant when the real part of the inverse scattering amplitude, given in Eq. 7.2, is zero. This leads to the resonance condition $a_{\mathrm{res}}^{-1} = r_e k^2/2$, where a_{res} is the value of the scattering length at which the interaction becomes resonant. In the limit of a broad resonance with $r_e = 0$, this condition is fulfilled for any k at the center of the resonance, where the scattering length diverges. However, at a narrow resonance with $r_e < 0$ the condition requires a negative a_{res} for $k > 0$. The mean square momentum in the Fermi sea is $3/5 \times \kappa_F^2$, leading to a mean square relative momentum of $3/5 \times (40/46 \times \kappa_F)^2$. Using this value for k^2, and inserting $r_e \approx -2R^*$ in the above resonance condition, we obtain $-1/(\kappa_F a) = 0.43$. This represents an effective shift of the Feshbach resonance center, as we average over all momenta of the Fermi sea [Ho11]. The magnitude of this shift agrees well with the observed asymmetry. Moreover, we find that many features at our narrow resonance appear to be shifted, e.g. the polaron-to-molecule crossing. However, the narrowness has many more implications and cannot simply be reduced to this shift. We will come back to this point in the context of the lifetime of the repulsive polaron, see Sec. 4.

The repulsive polaron peak is clearly visible up to $-1/(\kappa_F a) \approx -0.3$ while the attractive polaron peak vanishes already at $-1/(\kappa_F a) \approx 0.9$, see Fig. 7.5b. The fading out of the quasiparticle peak towards the strongly interacting regime approximately coincides with the position where the quasiparticle branches merge into the MHC. This shows that the polaron state is hardly observable as soon as it becomes degenerate with molecule-hole excitations. The MHC is not strictly limited to the range from E_m to $E_m - \varepsilon_F$, as discussed in more detail in Sec. 3. It extends below $E_m - \varepsilon_F$ because of finite temperature effects. It also extends slightly above E_m because of additional excitations in the spectral function of the molecules [Sch11]. As a consequence, for finite temperature, the attractive polaron can become degenerate with molecule-hole excitations for values of the interaction parameter above the calculated polaron-to-molecule crossing. This explains that the observed sharp peak is observed to disappear already at $-1/(\kappa_F a) \approx 0.9$, which lies somewhat above the zero-temperature polaron-to-molecule crossing predicted at 0.6.

It is interesting to consider the data analysis presented in Fig. 7.5b and c in relation to the common method of extracting the quasiparticle residue Z from the spectral weight of the narrow peak [Din01]. Close to resonance, we are in the linear response regime and our data can be interpreted in terms of this method. Our data suggests that this method leads to a significant underestimation of Z. For example at $-1/(\kappa_F a) \approx 0.9$, where the narrow peak of the attractive polaron vanishes, our theory still predicts $Z \approx 0.7$. This underestimation is consistent with the one reported in Ref. [Sch09b], see also related discussion in Ref. [Pun09]. A plausible explanation may be that such a method does not probe the polaron states alone, but also the molecule-hole excitations, which are degenerate with the polaron state. Our alternative method of measuring the residue via the Rabi frequency, as presented in the main paper, offers the advantage of being much less affected by the molecule-hole contribution. In fact, only the coherent part of the quasiparticle is expected to produce Rabi oscillations, see Sec. 6.

7.3.3 Molecule-hole continuum

The spectra presented in Fig. 7.2b of the main text reveal the MHC. This continuum arises from processes where the rf field associates a ^{40}K impurity and a ^{6}Li atom out of the Fermi sea to a molecule. Here we present a simple model for the spectral line shape, which allows us to interpret the data up to $-1/(\kappa_F a) \approx -1$, see Fig. 7.6.

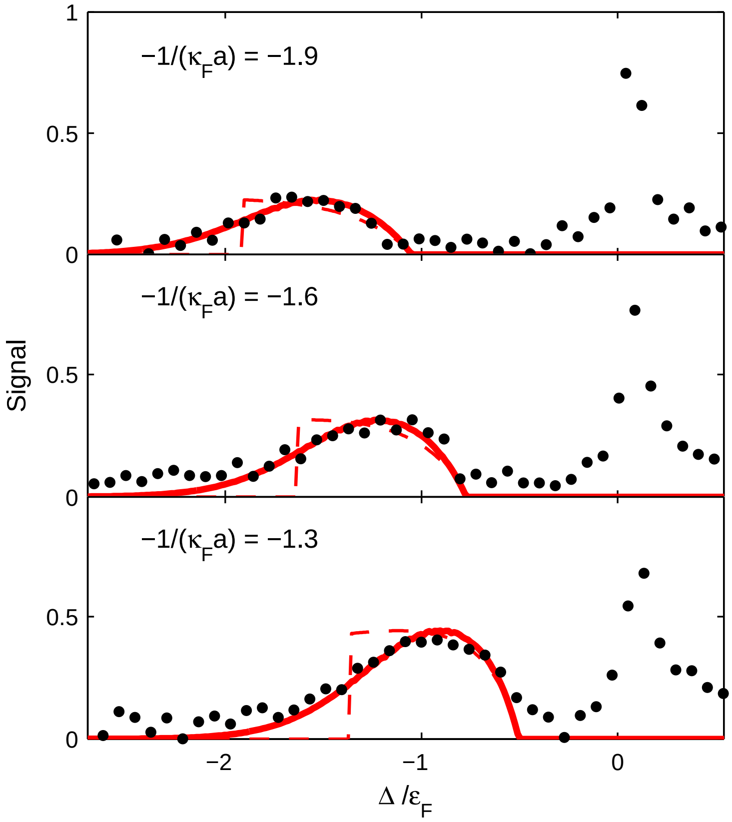

Figure 7.6: Molecule association spectra for different values of the interaction parameter. The signal is the fraction of transferred atoms as a function of the rf detuning. The data correspond to vertical cuts through Fig. 7.2b. The dashed line is the line shape model for zero temperature and the solid line for finite temperature. The upper threshold of the theoretical spectra corresponds to E_m.

For modeling the line shape, we consider two-body processes in which the rf field associates one ^{40}K and one ^{6}Li atom to a molecule. Higher-order processes, involving more than two particles, are neglected in this model but are briefly discussed at the end of this section. Let us first consider the association of ^{6}Li and ^{40}K with momenta $p_{\mathrm{Li}} = p_{\mathrm{K}} = 0$. This results in a molecule at rest plus a Fermi sea with a hole in the center. The energy of this state is determined by the binding energy of the molecule and by the interaction of the molecule with the Fermi sea. It is given by E_m and sets the onset of the MHC from the right (the top) in Fig. 7.6 (Fig. 7.2b). In general, ^{6}Li and ^{40}K have finite initial relative momentum $\hbar k$, leading to an initial relative kinetic energy in the center of mass frame $E_r = \hbar^2 k^2/2m_r$. The energy conservation of the association process is expressed in the Dirac δ function in Eq. 7.3. As a consequence, the molecule spectrum extends downwards to energies below E_m. We now consider an ensemble of ^{40}K and ^{6}Li atoms. Our experimental conditions are well approximated by a thermal cloud of ^{40}K in a homogeneous Fermi sea of ^{6}Li (see Methods). The momentum distribution of ^{6}Li is given by the Fermi-Dirac distribution $f_{\mathrm{Li}}^{\mathrm{FD}}(E_{\mathrm{Li}})$, with $E_{\mathrm{Li}} = p_{\mathrm{Li}}^2/2m_{\mathrm{Li}}$. The one of ^{40}K is approximated by the Maxwell-Boltzmann distribution $f_{\mathrm{K}}^{\mathrm{MB}}(E_{\mathrm{K}})$, with $E_{\mathrm{K}} = p_{\mathrm{K}}^2/2m_{\mathrm{K}}$. The latter distribution does not change its momentum dependence with position, thus, no integration over space is needed to obtain the spectral response

$$\mathcal{S}(\Delta) \propto \int\int d^3p_{\mathrm{Li}} \;\; d^3p_{\mathrm{K}} \;\; f_{\mathrm{Li}}^{\mathrm{FD}}(E_{\mathrm{Li}}) \;\; f_{\mathrm{K}}^{\mathrm{MB}}(E_{\mathrm{K}}) \;\; \mathcal{F}(k) \;\; \delta(-E_m + E_r + \Delta), \tag{7.3}$$

where $\mathcal{F}(k)$ is the Franck Condon overlap of the initial wavefunction with the molecule wavefunction. In our case the interaction in the initial state is negligible and $\mathcal{F}(k)$, as given in Ref. [Chi05], reduces to $\mathcal{F}(k) \propto (E_r/E_b^3)^{1/2}(1+E_r/E_b)^{-2}$. The parameter E_b is the binding energy of a molecule in vacuum at a resonance with finite effective range and reads $E_b = \hbar^2/(2m_r a^{*2})$ with the parameter [Pet04a] $a^* = -r_e/(\sqrt{1-2r_e/a}-1)$. In the calculation of $\mathcal{F}(k)$, we do not account for interactions with the Fermi sea. Because of this approximation, we apply the model only for $-1/(\kappa_F a) < -1$. For fitting the model line shapes to the experimental data, adjustable parameters are the individual heights of the spectra and the center of the Feshbach resonance. The latter parameter is required to be the same for all data sets in Fig. 7.6. Independently determined parameters are $k_B T/\varepsilon_F = 0.16$ and $\varepsilon_F = h \times 37\,\mathrm{kHz}$. The model (solid lines) reproduces our data remarkably well. It allows us to pinpoint the resonance position to $B_0 = 154.719(2)\,\mathrm{G}$. This determination of B_0 relies on our theoretical model to calculate E_m. To test this model dependence, we replace E_m simply by the binding energy of the molecule in vacuum plus the mean field energy, considering the corresponding atom-dimer scattering length [Lev11]. Using this simple model, the fit yields a resonance position that is 1 mG higher, which shows that the model dependence causes only a small systematic uncertainty. Moreover, the statistical fit uncertainty and the field calibration uncertainty are about 1 mG each.

For $T = 0$ and all other parameters unchanged, the model provides the dashed lines in Fig. 7.6. The spectra show a sharp drop at $\Delta = E_m - (40/46)\,\varepsilon_F$, which corresponds to the association of an impurity at rest and a majority atom at the Fermi edge. In an equal-mass mixture this process would occur at $\Delta = E_m - (1/2)\,\varepsilon_F$. Thus, the width of the MHC in the two-body approximation is much larger for a heavy impurity than it is for an equal-mass impurity and it is even narrower for a light impurity.

The true zero temperature ground state is actually at the energy $E_m - \varepsilon_F$, a molecule at rest formed from a ^{40}K atom at rest and a ^{6}Li atom at the Fermi edge. However, to reach this state, momentum conservation requires a higher-order process, i.e. the scattering of at least one additional ^{6}Li atom from and to the Fermi surface. Such processes are not included in the model presented here, which only considers the direct association of two atoms by an rf photon.

In the strongly interacting regime the spectral function of the molecule shows additional excitations above the molecular ground state [Sch11]. This leads to an extension of the MHC spectral response above E_m, of which we find clear indications in our data. The lower panel in Fig. 7.6 shows finite signal above E_m and the extension above E_m is very evident in the strongly interacting regime, see Fig. 7.2b.

7.3.4 Decay rate of the repulsive polarons

We analyse the decay of the repulsive polarons by assuming that they decay into well defined attractive polarons or well-defined molecules. In this quasiparticle picture, the decay is associated with the formation of a particle-hole pair in the Fermi sea to take up the released energy. In this sense, the decay into the attractive polaron is a 2-body process and the decay into the molecule is a 3-body process. We calculate the decay rate for these two channels by including them into the polaron self energy using a pole expansion of the ^{40}K propagator writing $G(\mathbf{k},\omega) \simeq Z_+/(\hbar\omega - E_+ - \hbar^2k^2/(2m_\mathrm{K})) + Z_-/(\hbar\omega - E_- - \hbar^2k^2/(2m_\mathrm{K}))$ and a pole expansion of the T-matrix writing $T(\mathbf{k},\omega) \simeq Z_m g^2/(\hbar\omega - (E_m - \varepsilon_F) - \hbar^2k^2/(2M))$. Here, $Z_\pm$ is the quasiparticle residue of the repulsive and attractive polaron respectively and Z_m the quasiparticle residue of the molecule. The factor $g^2 = 2\pi\hbar^4/(m_r^2 a^* \sqrt{1-2r_e/a})$ is the residue of the vacuum T-matrix for a general resonance. The details of this approach are given in Refs. [Mas11, Bru10], the only difference being that here we include the effects of the finite effective range. The imaginary part of the self energy gives the decay rate of the wavefunction and we thus take twice the imaginary part to calculate the population decay. The 2-body decay into the attractive polaron and an additional particle-hole pair is calculated numerically to all orders in the T-matrix by inserting the pole expansion for the ^{40}K propagator in the self energy in the ladder approximation. For the 3-body decay into a molecule and an additional particle-hole pair, we include terms containing two ^{6}Li holes in the ^{40}K self energy [Bru10], and an expansion to second order in the T-matrix relevant for $-1/(\kappa_F a) \ll -1$ yields

$$\Gamma_{PM} \simeq \frac{64\kappa_F a}{45\pi^3}\frac{Z_+^3}{m_\mathrm{K}^2\sqrt{m_\mathrm{Li}}}\left(1+\frac{m_\mathrm{Li}}{M}\right)^{3/2}\left(\frac{\hbar\kappa_F}{\sqrt{2(E_+ - E_m + \epsilon_F)}}\right)^5 \frac{a}{a^*\sqrt{1-2r_e/a^*}}\frac{\epsilon_F}{\hbar}. \qquad (7.4)$$

For simplicity, we have taken $Z_m = 1$, which is an appropriate assumption for $-1/(\kappa_F a) \ll -1$. The effect of the narrow resonance on the decay rate enters through the quasiparticle residue Z_+, the energies E_+, E_-, E_m and directly through the effective range r_e. This decay rate has the same a^6 dependence as the three-body decay in vacuum in the limit of a broad resonance derived in Ref. [Pet03]. The numerical prefactor however differs since we have included the effects of the Fermi sea in a perturbative calculation.

The results for the decay rates of repulsive polarons are shown in Fig. 7.7. The experimental data agree well with the theoretical results obtained for our narrow resonance (continuous lines) as already shown in Fig. 7.3 in the main text. For comparison, we also show the decay rates one would obtain in the limit of a broad resonance (dashed lines). We find that as magnitude of the effective range increases with respect to the interparticle spacing, the dominant two-body decay is strongly suppressed. This suppression is mainly

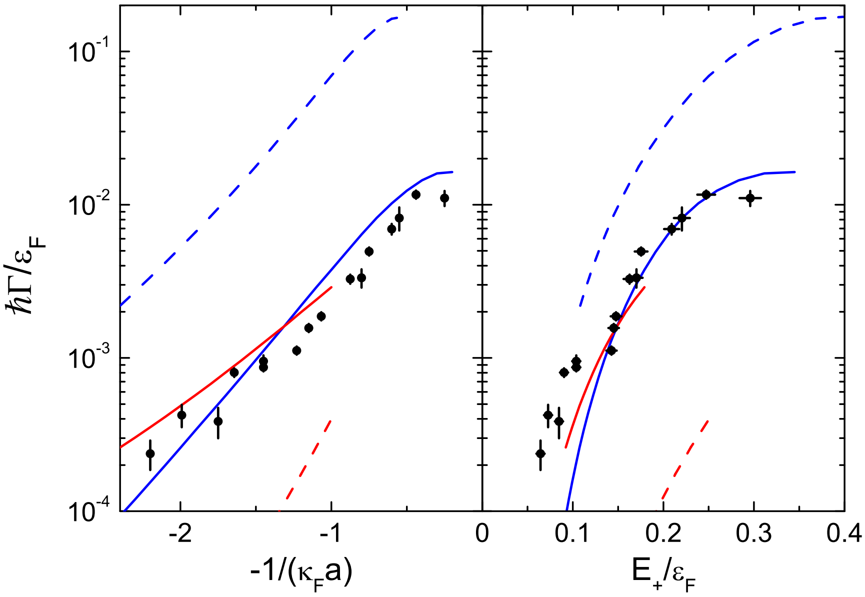

Figure 7.7: Decay rates of repulsive ^{40}K polarons in a Fermi sea of ^{6}Li atoms, shown as a function of interaction strength (left) and of the energy of the repulsive polaron (right). Blue and red lines represent the two- and three-body contributions, respectively, while data points are the experimental findings as also shown in Fig. 3 of the main text. The results for the moderately narrow resonance under study here (solid lines) is compared with the theoretical results obtained for the universal limit of a very broad resonance (dashed lines). The experimental values of E_+ are obtained by interpolation of the narrow peak position data Δ_{peak}, see Fig. 7.5d.

due to a large reduction of the attractive polaron residue Z_-. Instead, the weaker three-body decay increases, which we attribute to the reduction of the polaron-molecule energy difference $E_+ - E_m + \epsilon_F$. Taking both decay rates together, the decay rate is at least an order of magnitude smaller at our narrow resonance as compared to the case of a broad resonance. It is important to note that this strong suppression of the decay at a given $-1/(\kappa_F a)$ cannot be simply attributed to the effective resonance shift at our narrow Feshbach resonance as discussed in Sec. 2. When taking this shift into account, a suppression factor of five to ten remains. To highlight this point, we choose a representation that is independent of the interaction parameter and that gives the dependence on the polaron energy, a direct manifestation of strong interactions. The right panel shows the same data and calculations as a function of E_+. Also for a given E_+, the repulsive polaron at our narrow resonance turns out to be much more stable than the repulsive polaron at a broad resonance.

7.3.5 Decay of repulsive polarons to molecules

The decay of the repulsive polarons, shown in Fig. 7.3 of the main text, is measured by applying a special three-pulse scheme (see Methods). In this section we exploit the flexibility of this scheme to study the decay to lower-lying energy states in more detail. At a given interaction strength $-1/(\kappa_F a) = -0.9$, we demonstrate that the repulsive polarons decay to molecules by showing that an rf spectrum taken after decay perfectly matches a reference spectrum of molecules.

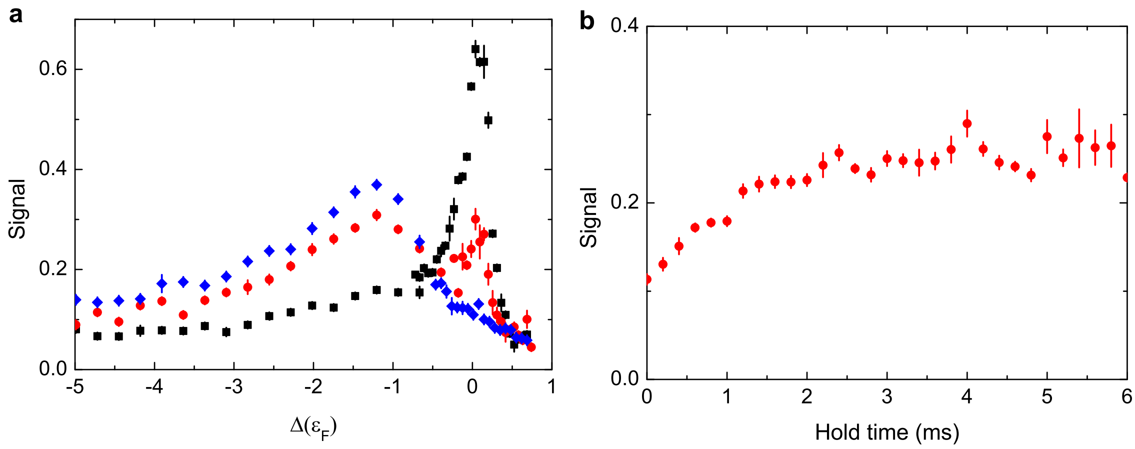

Figure 7.8: Decay of repulsive polarons to molecules at $-1/(\kappa_F a) = -0.9$. (a) The black squares (red dots) show the spectrum right after (2 ms after) the repulsive polaron has been populated. The blue diamonds show the dissociation spectrum of molecules for reference. The signal is the fraction of atoms transferred from the interacting spin state $|1\rangle$ to the noninteracting spin state $|0\rangle$. Note that the polaron peak at positive detuning is highly saturated and thus its signal is not proportional to the number of polarons. (b) The rf energy detuning is fixed to $\Delta = -1.3\,\varepsilon_F$ and the signal is recorded versus hold time. The error bars indicate the statistical uncertainties derived from at least three individual measurements.

To populate the repulsive polaron branch, as done for the measurements of the decay rate, we tune the energy of the first pulse to E_+, corresponding to $\Delta = 0.16\,\varepsilon_F$ at $-1/(\kappa_F a) = -0.9$. The pulse duration ($t_p = 0.06$ ms) and the intensity are set to correspond to a π-pulse in the noninteracting system. The second pulse removes the remaining non-transferred atoms by transferring them to a third spin state. In contrast to the decay measurement presented in the main text, we here use much more rf power for the third pulse to be able to efficiently dissociate molecules. For this purpose, we set $t_p = 0.3$ ms and the pulse area corresponds to a 3π-pulse in the noninteracting system. By varying the rf detuning, we record spectra for zero hold time (black squares) and for a hold time of 2 ms (red dots), see Fig. 7.8a. The peak at small positive detuning shows the back-transfer of repulsive polarons. The corresponding signal decreases with hold time, signalling the decay of the repulsive polaron. In addition, a wide continuum in a range of negative detunings rises with increasing hold time. Such a wide continuum involves coupling to high momentum states, signaling a short distance between ^{40}K and ^{6}Li. To confirm that this continuum stems from molecules, we compare it to a reference spectrum of the dissociation of molecules (blue diamonds). We find a perfect match. To take such a reference spectrum, only the detuning of the first rf pulse is changed to directly associate molecules in the MHC instead of populating the repulsive polaron branch. We achieve a good association efficiency with $\Delta = -0.54\,\varepsilon_F$ and $t_p = 0.5$ ms.

To study the evolution of the molecule population, which is fed by the decay of the repulsive polarons, we set the detuning of the third pulse to the peak of the molecule signal at $\Delta = -1.3\,\varepsilon_F$ and record the signal as a function of the hold time, see Fig. 7.8b. A simple exponential fit yields a rate of about $1\,\mathrm{ms}^{-1}{=}\,0.0043\,\varepsilon_F/\hbar$, which is in good agreement with the measured decay rate of the repulsive polaron at $-1/(\kappa_F a) = -0.9$. The finite signal at zero hold time may have two origins. One contribution is some decay during the finite pulse durations of the three pulses, which are not included in the hold time. Another contribution may be the high momentum tail of the repulsive polarons as discussed in Ref. [Sch09b].

Note that we do not find any second sharp peak at negative detuning, which would indicate the population of the attractive polaron branch. In case the repulsive polaron decays to the attractive polaron, the absence of the attractive polaron peak implies a very rapid subsequent decay of the attractive polaron to the MHC. Such a fast decay of the attractive polaron to the MHC is consistent with the very small signal of the attractive polaron peak throughout the regime of strong interaction as discussed in Sec. 2.

Let us briefly discuss the possible role of inelastic two-body relaxation in the ^{6}Li -^{40}K mixture, which is energetically possible as ^{40}K is not in the lowest spin state. This process was identified in Ref. [Nai11] as a source of losses. However, this relaxation is about an order of magnitude slower than the measured decay rate of the repulsive polaron and thus does not affect our measurements.

7.3.6 Rabi oscillations and polaron quasiparticle residue

For high rf power, the signal is well beyond linear response and the ^{40}K atoms exhibit coherent Rabi oscillations between the spin states $|0\rangle$ and $|1\rangle$. In this regime the oscillations are so fast, that the polaron decay plays a minor role and can be ignored to a first approximation. The Rabi frequency depends on the matrix element of the rf probe between the initial state $|0\rangle$ and the final state $|1\rangle$. Since the probe is homogenous in space, it does not change the spatial part of the atomic wavefunction and it can be described by the operator [Mas08a] $\hat{R} \propto \Omega_0 \sum_{\mathbf{q}} (\hat{a}^\dagger_{1\mathbf{q}} \hat{a}_{0\mathbf{q}} + h.c.)$ where $\hat{a}^\dagger_{i\mathbf{q}}$ ($\hat{a}_{i\mathbf{q}}$) creates (annihilates) a ^{40}K atom with momentum $\mathbf{q}$ in spin state i and Ω_0 is the unperturbed Rabi frequency of the $|0\rangle$ to $|1\rangle$ transition in the non-interacting case. Considering for simplicity an impurity at rest, the initial non-interacting state is given by $|I\rangle = \hat{a}^\dagger_{0\mathbf{q}=0}|\mathrm{FS}\rangle$ where $|\mathrm{FS}\rangle$ is the ^{6}Li Fermi sea. The final polaronic state at zero momentum can be written as [Che06]

$$|F\rangle = \sqrt{Z}\hat{a}^\dagger_{1\mathbf{q}=0}|\mathrm{FS}\rangle + \sum_{q<\hbar\kappa_F<p} \phi_{\mathbf{p},\mathbf{q}} \hat{a}^\dagger_{1\mathbf{q}-\mathbf{p}} \hat{b}^\dagger_{\mathbf{p}} \hat{b}_{\mathbf{q}} |\mathrm{FS}\rangle + \dots \tag{7.5}$$

where $\hat{b}^\dagger_{\mathbf{q}}$ ($\hat{b}_{\mathbf{q}}$) creates (annihilates) a ^{6}Li atom with momentum $\mathbf{q}$. The second term contains a Fermi sea with at least one particle-hole excitation and thus is orthogonal to an unperturbed Fermi sea. Therefore the matrix element reduces to $\langle F|\hat{R}|I\rangle = \sqrt{Z}\,\Omega_0$ and we obtain the Rabi frequency

$$\Omega = \sqrt{Z}\,\Omega_0. \tag{7.6}$$

We neglect the momentum dependence of the quasiparticle residue and do not perform a thermal average over the initial states, which we expect to be a good approximation since $T \ll \epsilon_F/k_B$.

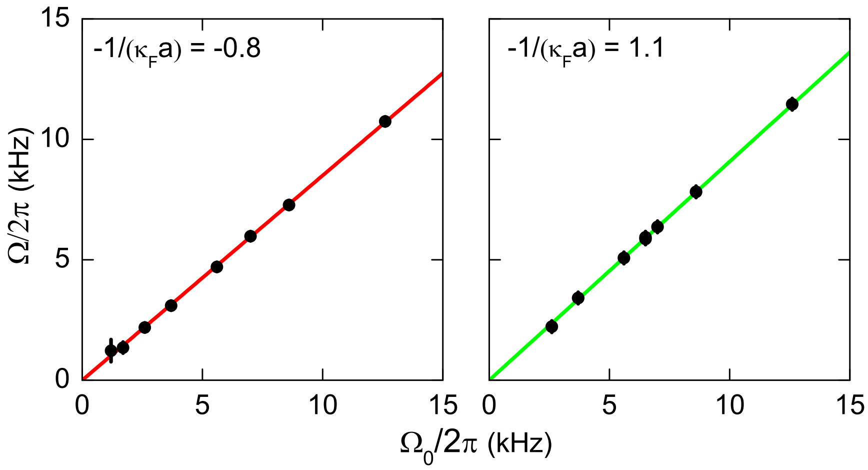

Figure 7.9: Linear increase of the Rabi frequency Ω with the unperturbed Rabi frequency Ω_0. The left (right) panel shows the driving to the repulsive (attractive) polaron. The solid lines are linear fits without offset and demonstrate the proportionality $\Omega \propto \Omega_0$.

In Fig. 7.9 we plot the observed Rabi frequency Ω as a function of the unperturbed Rabi frequency Ω_0. We find that the proportionality $\Omega \propto \Omega_0$ holds over a wide range of rf power. The measurements presented in the main text, taken at $\Omega_0 = 2\pi \times 6.5\,\text{kHz}$ and $12.6\,\text{kHz}$, are safely within this range.

CHAPTER 8

ADDITIONAL PUBLICATIONS

Precision Measurements of Collective Oscillations in the BEC-BCS Crossover
A. Altmeyer, S. Riedl, C. Kohstall, M. J. Wright, R. Geursen, M. Bartenstein, C. Chin, J. Hecker Denschlag, and R. Grimm
Phys. Rev. Lett. **98**, 040401 (2007).

We report on precision measurements of the frequency of the radial compression mode in a strongly interacting, optically trapped Fermi gas of ^{6}Li atoms. Our results allow for a test of theoretical predictions for the equation of state in the BEC-BCS crossover. We confirm recent quantum Monte Carlo results and rule out simple mean-field BCS theory. Our results show the long-sought beyond-mean-field effects in the strongly interacting Bose-Einstein condensation (BEC) regime.

Dynamics of a strongly interacting Fermi gas: The radial quadrupole mode
A. Altmeyer, S. Riedl, M. J. Wright, C. Kohstall, J. Hecker Denschlag, and R. Grimm
Phys. Rev. A **76**, 033610 (2007).

We report on measurements of an elementary surface mode in an ultracold, strongly interacting Fermi gas of ^{6}Li atoms. The radial quadrupole mode allows us to probe hydrodynamic behavior in the crossover from Bose-Einstein condensation (BEC) to the Bardeen-Cooper-Schrieffer (BCS) regime without being influenced by changes in the equation of state. We examine the frequency and damping of this mode, along with its expansion dynamics. In the unitarity limit and on the BEC side of the resonance, the observed frequencies agree with standard hydrodynamic theory. However, on the BCS side of the crossover, a striking downshift of the oscillation frequency is observed in the hydrodynamic regime as a precursor to an abrupt transition to collisionless behavior; this indicates coupling of the oscillation to fermionic pairs.

Finite-temperature collective dynamics of a Fermi gas in the BEC-BCS crossover
M. J. Wright, S. Riedl, A. Altmeyer, C. Kohstall, E. R. Sánchez Guajardo, J. Hecker Denschlag, and R. Grimm
Phys. Rev. Lett. **99**, 150403 (2007).

We report on experimental studies on the collective behavior of a strongly interacting Fermi gas with tunable interactions and variable temperature. A scissors mode excitation in an elliptical trap is used to characterize the dynamics of the quantum gas in terms of hydrodynamic or near-collisionless behavior. We obtain a crossover phase diagram for collisional properties, showing a large region where a nonsuperfluid strongly interacting gas shows hydrodynamic behavior. In a narrow interaction regime on the BCS side of the crossover, we find a novel temperature-dependent damping peak, suggesting a relation to the superfluid phase transition.

Collective oscillations of a Fermi gas in the unitarity limit: Temperature effects and the role of pair correlations
S. Riedl, E. R. Sánchez Guajardo, C. Kohstall, A. Altmeyer, M. J. Wright, J. Hecker Denschlag, R. Grimm, G. M. Bruun, and H. Smith
Phys. Rev. A **78**, 053609 (2008).

We present detailed measurements of the frequency and damping of three different collective modes in an ultracold trapped Fermi gas of ^{6}Li atoms with resonantly tuned interactions. The measurements are carried out over a wide range of temperatures. We focus on the unitarity limit, where the scattering length is much greater than all other relevant length scales. The results are compared to theoretical calculations that take into account Pauli blocking and pair correlations in the normal state above the critical temperature for superfluidity. We show that these two effects nearly compensate each other and the behavior of the gas is close to that of a classical gas.

Pairing-gap, pseudogap, and no-gap phases in the radio-frequency spectra of a trapped unitary ^{6}Li gas
P. Pieri, A. Perali, G. C. Strinati, S. Riedl, M. J. Wright, A. Altmeyer, C. Kohstall, E. R. Sánchez Guajardo, J. Hecker Denschlag, and R. Grimm
Phys. Rev. A **84**, 011608 (2011).

Radio frequency spectra of a trapped unitary ^{6}Li gas are reported and analyzed in terms of a theoretical approach that includes both final-state and trap effects. The different strength of the final-state interaction across the trap is crucial for evidencing two main peaks associated with two distinct phases residing in different trap regions. These are the pairing-gap and pseudo-gap phases below the critical temperature T_c, which evolve into the pseudo-gap and no-gap phases above T_c. In this way, a long standing puzzle about the interpretation of rf spectra for ^{6}Li in a trap is solved.

BIBLIOGRAPHY

[Ada94] C. S. Adams, M. Sigel, and J. Mlynek, *Atom optics*, Phys. Rep. **240**, 143 (1994).

[Alt07a] A. Altmeyer, S. Riedl, C. Kohstall, M. J. Wright, R. Geursen, M. Bartenstein, C. Chin, J. Hecker Denschlag, and R. Grimm, *Precision Measurements of Collective Oscillations in the BEC-BCS Crossover*, Phys. Rev. Lett. **98**, 040401 (2007).

[Alt07b] A. Altmeyer, S. Riedl, M. J. Wright, C. Kohstall, J. Hecker Denschlag, and R. Grimm, *Dynamics of a strongly interacting Fermi gas: The radial quadrupole mode*, Phys. Rev. A **76**, 033610 (2007).

[And95] M. H. Anderson, J. R. Ensher, M. R. Matthews, C. E. Wieman, and E. A. Cornell, *Observation of Bose-Einstein condensation in dilute atomic vapor*, Science **269**, 198 (1995).

[And97] M. R. Andrews, C. G. Townsend, H.-J. Miesner, D. S. Durfee, D. M. Kurn, and W. Ketterle, *Observation of Interference Between Two Bose Condensates*, Science **275**, 637 (1997).

[Arn99] M. Arndt, O. Nairz, J. Vos-Andreae, C. Keller, G. van der Zouw, and A. Zeilinger, *Wave-particle duality of C-60 molecules*, Nature **401**, 680 (1999).

[AS02] J. R. Abo-Shaeer, C. Raman, and W. Ketterle, *Formation and Decay of Vortex Lattices in Bose-Einstein Condensates at Finite Temperatures*, Phys. Rev. Lett. **88**, 070409 (2002).

[Baa10] J. E. Baarsma, K. B. Gubbels, and H. T. C. Stoof, *Population and mass imbalance in atomic Fermi gases*, Phys. Rev. A **82**, 013624 (2010).

[Ban00] Y. B. Band, M. Trippenbach, J. P. Burke, and P. S. Julienne, *Elastic Scattering Loss of Atoms from Colliding Bose-Einstein Condensate Wave Packets*, Phys. Rev. Lett. **84**, 5462 (2000).

[Ban01] Y. B. Band, J. P. Burke, A. Simoni, and P. S. Julienne, *Suppression of elastic scattering loss for slowly colliding Bose-Einstein condensates*, Phys. Rev. A **64**, 023607 (2001).

[Bar57] J. Bardeen, L. N. Cooper, and J. R. Schrieffer, *Theory of Superconductivity*, Phys. Rev. **108**, 1175 (1957).

[Bar04a] M. Bartenstein, A. Altmeyer, S. Riedl, S. Jochim, C. Chin, J. Hecker Denschlag, and R. Grimm, *Collective Excitations of a Degenerate Gas at the BEC-BCS Crossover*, Phys. Rev. Lett. **92**, 203201 (2004).

[Bar04b] M. Bartenstein, A. Altmeyer, S. Riedl, S. Jochim, C. Chin, J. Hecker Denschlag, and R. Grimm, *Crossover from a Molecular Bose-Einstein Condensate to a Degenerate Fermi Gas*, Phys. Rev. Lett. **92**, 120401 (2004).

[Bar05] M. Bartenstein, A. Altmeyer, S. Riedl, R. Geursen, S. Jochim, C. Chin, J. Hecker Denschlag, R. Grimm, A. Simoni, E. Tiesinga, C. J. Williams, and P. S. Julienne, *Precise determination of ^{6}Li cold collision parameters by radio-frequency spectroscopy on weakly bound molecules*, Phys. Rev. Lett. **94**, 103201 (2005).

[Bar08] M. A. Baranov, C. Lobo, and G. V. Shlyapnikov, *Superfluid pairing between fermions with unequal masses*, Phys. Rev. A **78**, 033620 (2008).

[Bau09] I. Bausmerth, A. Recati, and S. Stringari, *Chandrasekhar-Clogston limit and phase separation in Fermi mixtures at unitarity*, Phys. Rev. A **79**, 043622 (2009).

[Bea97] I. G. Bearden *et al.*, *Collective expansion in high energy heavy ion collisions*, Phys. Rev. Lett. **78**, 2080 (1997).

[Ber03] T. Bergeman, M. Moore, and M. Olshanii, *Atom-atom scattering under cylindrical harmonic confinement: Numerical and analytic studies of the confinement induced resonance*, Physical Review Letters **91**, 163201 (2003).

[Bil08] J. Billy, V. Josse, Z. Zuo, A. Bernard, B. Hambrecht, P. Lugan, D. Clment, L. Sanchez-Palencia, P. Bouyer, and A. Aspect, *Direct observation of Anderson localization of matter waves in a controlled disorder*, Nature **453**, 891 (2008).

[Blo08a] I. Bloch, J. Dalibard, and W. Zwerger, *Many-body physics with ultracold gases*, Reviews of Modern Physics **80**, 885 (2008).

[Blo08b] I. Bloch, J. Dalibard, and W. Zwerger, *Many-body physics with ultracold gases*, Rev. Mod. Phys. **80**, 885 (2008).

[Boh99] J. L. Bohn and P. S. Julienne, *Semianalytic theory of laser-assisted resonant cold collisions*, Phys. Rev. A **60**, 414 (1999).

[Bon04] K. Bongs and K. Sengstock, *Physics with coherent matter waves*, Reports on Progress in Physics **67**, 907 (2004).

[Bou03] T. Bourdel, J. Cubizolles, L. Khaykovich, K. M. F. Magalhães, S. J. J. M. F. Kokkelmans, G. V. Shlyapnikov, and C. Salomon, *Measurement of the Interaction Energy near a Feshbach Resonance in a ^{6}Li Fermi Gas*, Phys. Rev. Lett. **91**, 020402 (2003).

[Bra95] C. C. Bradley, C. A. Sackett, J. J. Tollett, and R. G. Hulet, *Evidence of Bose-Einstein condensation in an atomic gas with attractive interactions*, Phys. Rev. Lett. **75**, 1687 (1995).

[Bra07] P. Braun-Munzinger and J. Stachel, *The quest for the quark-gluon plasma*, Nature **448**, 302 (2007).

[Bre03] V. Bretin, P. Rosenbusch, F. Chevy, G. V. Shlyapnikov, and J. Dalibard, *Quadrupole Oscillation of a Single-Vortex Bose-Einstein Condensate: Evidence for Kelvin Modes*, Phys. Rev. Lett. **90**, 100403 (2003).

[Bro23] L. de Broglie, *Waves and quanta*, Nature **112**, 540 (1923).

[Bru05] G. M. Bruun, A. D. Jackson, and E. E. Kolomeitsev, *Multichannel scattering and Feshbach resonances: Effective theory, phenomenology, and many-body effects*, Phys. Rev. A **71**, 052713 (2005).

[Bru10] G. M. Bruun and P. Massignan, *Decay of polarons and molecules in a strongly polarized Fermi gas*, Phys. Rev. Lett. **105**, 020403 (2010).

[Bug04] C. Buggle, J. Léonard, W. von Klitzing, and J. T. M. Walraven, *Interferometric Determination of the s and d-Wave Scattering Amplitudes in ^{87}Rb*, Phys. Rev. Lett. **93**, 173202 (2004).

[Cao11] C. Cao, E. Elliott, J. Joseph, H. Wu, J. Petricka, T. Schäfer, and J. E. Thomas, *Universal Quantum Viscosity in a Unitary Fermi Gas*, Science **331**, 58 (2011).

[Cas97] Y. Castin and J. Dalibard, *Relative phase of two Bose-Einstein condensates*, Phys. Rev. A **55**, 4330 (1997).

[Ced07] L. S. Cederbaum, A. I. Streltsov, Y. B. Band, and O. E. Alon, *Interferences in the Density of Two Bose-Einstein Condensates Consisting of Identical or Different Atoms*, Phys. Rev. Lett. **98**, 110405 (2007).

[Cha11] S.-Y. Chang, M. Randeria, and N. Trivedi, *Ferromagnetism in the upper branch of the Feshbach resonance and the hard-sphere Fermi gas*, PNAS **108**, 51 (2011).

[Che00] F. Chevy, K. M. Madison, and J. Dalibard, *Measurement of the Angular Momentum of a Rotating Bose-Einstein Condensate*, Phys. Rev. Lett. **85**, 2223 (2000).

[Che03] F. Chevy and S. Stringari, *Kelvin modes of a fast rotating Bose-Einstein condensate*, Phys. Rev. A **68**, 053601 (2003).

[Che05a] Q. Chen, J. Stajic, and K. Levin, *Thermodynamics of Interacting Fermions in Atomic Traps*, Phys. Rev. Lett. **95**, 260405 (2005).

[Che05b] Q. Chen, J. Stajic, S. Tan, and K. Levin, *BCS-BEC Crossover: From High Temperature Superconductors to Ultracold Superfluids*, Phys. Rep. **412**, 1 (2005).

[Che06] F. Chevy, *Universal phase diagram of a strongly interacting Fermi gas with unbalanced spin populations*, Phys. Rev. A **74**, 063628 (2006).

[Che10] F. Chevy and C. Mora, *Ultra-cold polarized Fermi gases*, Rep. Prog. Phys. **73**, 112401 (2010).

[Chi00] A. P. Chikkatur, A. Görlitz, D. M. Stamper-Kurn, S. Inouye, S. Gupta, and W. Ketterle, *Suppression and Enhancement of Impurity Scattering in a Bose-Einstein Condensate*, Phys. Rev. Lett. **85**, 483 (2000).

[Chi04] C. Chin, M. Bartenstein, A. Altmeyer, S. Riedl, S. Jochim, J. Hecker Denschlag, and R. Grimm, *Observation of the Pairing Gap in a Strongly Interacting Fermi Gas*, Science **305**, 1128 (2004).

[Chi05] C. Chin and P. S. Julienne, *Radio-frequency transitions on weakly bound ultracold molecules*, Phys. Rev. A **71**, 012713 (2005).

[Chi06] J. K. Chin, D. Miller, Y. Liu, C. Stan, W. Setiawan, C. Sanner, K. Xu, and W. Ketterle, *Evidence for Superfluidity of Ultracold Fermions in an Optical Lattice*, Nature **443**, 961 (2006).

[Chi10] C. Chin, R. Grimm, P. S. Julienne, and E. Tiesinga, *Feshbach resonances in ultracold gases*, Rev. Mod. Phys. **82**, 1225 (2010).

[Cla07] B. Clancy, L. Luo, and J. E. Thomas, *Observation of Nearly Perfect Irrotational Flow in Normal and Superfluid Strongly Interacting Fermi Gases*, Phys. Rev. Lett. **99**, 140401 (2007).

[Com07] R. Combescot, A. Recati, C. Lobo, and F. Chevy, *Normal state of highly polarized Fermi gases: Simple many-body approaches*, Phys. Rev. Lett. **98**, 180402 (2007).

[Com09] R. Combescot, S. Giraud, and X. Leyronas, *Analytical theory of the dressed bound state in highly polarized Fermi gases*, Europhys. Lett. **88**, 60007 (2009).

[Con09] G. J. Conduit, A. G. Green, and B. D. Simons, *Inhomogeneous phase formation on the border of itinerant ferromagnetism*, Phys. Rev. Lett. **103**, 207201 (2009).

[Cos10] L. Costa, J. Brachmann, A.-C. Voigt, C. Hahn, M. Taglieber, T. W. Hänsch, and K. Dieckmann, *s-wave interaction in a two-species Fermi-Fermi mixture at a narrow Feshbach resonance*, Phys. Rev. Lett. **105**, 123201 (2010).

[Cro09] A. D. Cronin, J. Schmiedmayer, and D. E. Pritchard, *Optics and interferometry with atoms and molecules*, Rev. Mod. Phys. **81**, 1051 (2009).

[Cub03] J. Cubizolles, T. Bourdel, S. J. J. M. F. Kokkelmans, G. V. Shlyapnikov, and C. Salomon, *Production of Long-Lived Ultracold Li_2 Molecules from a Fermi Gas*, Phys. Rev. Lett. **91**, 240401 (2003).

[Dal99] F. Dalfovo, S. Giorgini, L. P. Pitaevskii, and S. Stringari, *Theory of Bose-Einstein condensation in trapped gases*, Rev. Mod. Phys. **71**, 463 (1999).

[Dan10] J. G. Danzl, M. J. Mark, E. Haller, M. Gustavsson, R. Hart, J. Aldegunde, J. M. Hutson, and H.-C. Nägerl, *An ultracold high-density sample of rovibronic ground-state molecules in an optical lattice*, Nature Phys. **6**, 265 (2010).

[Dav27] C. J. Davisson and L. H. Germer, *The scattering of electrons by a single crystal of nickel*, Nature **119**, 558560 (1927).

[Dav95] K. B. Davis, M. O. Mewes, M. R. Andrews, N. J. van Druten, D. S. Durfee, D. M. Kurn, and W. Ketterle, *Bose-Einstein condensation in a gas of sodium atoms*, Phys. Rev. Lett. **75**, 3969 (1995).

[DeM99] B. DeMarco and D. S. Jin, *Onset of Fermi Degeneracy in a Trapped Atomic Gas*, Science **285**, 1703 (1999).

[D'I05] J. P. D'Incao and B. D. Esry, *Scattering length scaling laws for ultracold three-body collisions*, Phys. Rev. Lett. **94**, 213201 (2005).

[Die10] R. B. Diener and M. Randeria, *BCS-BEC crossover with unequal-mass fermions*, Phys. Rev. A **81**, 033608 (2010).

[Din01] H. Ding, J. R. Engelbrecht, Z. Wang, J. C. Campuzano, S.-C. Wang, H.-B. Yang, R. Rogan, T. Takahashi, K. Kadowaki, and D. G. Hinks, *Coherent Quasiparticle Weight and Its Connection to High- T_c Superconductivity from Angle-Resolved Photoemission*, Phys. Rev. Lett. **87**, 227001 (2001).

[Dod97] R. J. Dodd, K. Burnett, M. Edwards, and C. Clark, *Excitation spectroscopy of vortex states in dilute Bose-Einstein condensed gases*, Phys. Rev. A **56**, 587 (1997).

[Dui05] R. A. Duine and A. H. MacDonald, *Itinerant ferromagnetism in an ultracold atom Fermi gas*, Phys. Rev. Lett. **95**, 230403 (2005).

[Est30] I. Estermann and O. Stern, *Beugung von Molekularstrahlen*, Z. Phys. **61**, 95 (1930).

[Far00] M. Farine, P. Schuck, and X. Viñas, *Moment of inertia of a trapped superfluid gas of atomic fermions*, Phys. Rev. A **62**, 013608 (2000).

[Fed96] P. O. Fedichev, Y. Kagan, G. V. Shlyapnikov, and J. T. M. Walraven, *Influence of nearly resonant light on the scattering length in low-temperature atomic gases*, Phys. Rev. Lett. **77**, 2913 (1996).

[Fei09] A. E. Feiguin and M. P. A. Fisher, *Exotic paired states with anisotropic spin-dependent Fermi surfaces*, Phys. Rev. Lett. **103**, 025303 (2009).

[Fer02] G. Ferrari, M. Inguscio, W. Jastrzebski, G. Modugno, G. Roati, and A. Simoni, *Collisional properties of ultracold K-Rb mixtures*, Phys. Rev. Lett. **89**, 053202 (2002).

[Fer03] F. Ferlaino, R. J. Brecha, P. Hannaford, F. Riboli, G. Roati, G. Modugno, and M. Inguscio, *Bipolar oscillations in a quantum degenerate Fermi-Bose atomic mixture*, J. Opt. B: Quantum Semiclassical Opt. **5**, S3 (2003).

[Fer08] F. Ferlaino, S. Knoop, M. Mark, M. Berninger, H. Schöbel, H.-C. Nägerl, and R. Grimm, *Collisions between tunable halo dimers: Exploring an elementary four-body process with identical bosons*, Phys. Rev. Lett. **101**, 023201 (2008).

[Fer09] F. Ferlaino, S. Knoop, and R. Grimm, *Ultracold Feshbach molecules*, in R. V. Krems, B. Friedrich, and W. C. Stwalley (Eds.), *Cold Molecules: Theory, Experiment, Applications*, arXiv:0809.3920 (2009).

[For05] M. M. Forbes, E. Gubankova, W. V. Liu, and F. Wilczek, *Stability criteria for breached-pair superfluidity*, Phys. Rev. Lett. **94**, 017001 (2005).

[Gae10] J. P. Gaebler, J. T. Stewart, T. E. Drake, D. S. Jin, A. Perali, P. Pieri, and G. C. Strinati, *Observation of pseudogap behaviour in a strongly interacting Fermi gas*, Nature Phys. **6**, 569 (2010).

[Gen01] S. D. Gensemer and D. S. Jin, *Transition from collisionless to hydrodynamic behavior in an ultracold Fermi gas*, Phys. Rev. Lett. **87**, 173201 (2001).

[Ger11] S. Gerlich, S. Eibenberger, M. Tomandl, S. Nimmrichter, K. Hornberger, P. J. Fagan, J. Tüxen, M. Mayor, and M. Arndt, *Quantum interference of large organic molecules*, Nat. Commun. **2**, 263 (2011).

[Gez09] A. Gezerlis, S. Gandolfi, K. E. Schmidt, and J. Carlson, *Heavy-light fermion mixtures at unitarity*, Phys. Rev. Lett. **103**, 060403 (2009).

[Gio08] S. Giorgini, L. P. Pitaevskii, and S. Stringari, *Theory of ultracold atomic Fermi gases*, Rev. Mod. Phys. **80**, 1215 (2008).

[GO00] D. Guéry-Odelin, *Spinning up and down a Boltzmann gas*, Phys. Rev. A **62**, 033607 (2000).

[Gre03] M. Greiner, C. A. Regal, and D. S. Jin, *Emergence of a Molecular Bose-Einstein Condensate from a Fermi Gas*, Nature **426**, 537 (2003).

[Gre05] M. Greiner, C. A. Regal, J. T. Stewart, and D. S. Jin, *Probing Pair-Correlated Fermionic Atoms through Correlations in Atom Shot Noise*, Phys. Rev. Lett. **94**, 110401 (2005).

[Gri93] G. F. Gribakin and V. V. Flambaum, *Calculation of the scattering length in atomic collisions using the semiclassical approximation*, Phys. Rev. A **48**, 546 (1993).

[Gri00] R. Grimm, M. Weidemüller, and Y. B. Ovchinnikov, *Optical dipole traps for neutral atoms*, Adv. At. Mol. Opt. Phys. **42**, 95 (2000).

[Gri08] R. Grimm, *Ultracold Fermi gases in the BEC-BCS crossover: A review from the Innsbruck perspective*, in Inguscio *et al.* [Ing08b], 413–462.

[Had06] Z. Hadzibabic, P. Krger, M. Cheneau, B. Battelier, and J. Dalibard, *Berezinskii-Kosterlitz-Thouless crossover in a trapped atomic gas*, Nature **441**, 1118 (2006).

[Hal01a] P. C. Haljan, B. P. Anderson, I. Coddington, and E. A. Cornell, *Use of Surface-Wave Spectroscopy to Characterize Tilt Modes of a Vortex in a Bose-Einstein Condensate*, Phys. Rev. Lett. **86**, 2922 (2001).

[Hal01b] P. C. Haljan, I. Coddington, P. Engels, and E. A. Cornell, *Driving Bose-Einstein-Condensate Vorticity with a Rotating Normal Cloud*, Phys. Rev. Lett. **87**, 210403 (2001).

[Hal10] E. Haller, M. J. Mark, R. Hart, J. G. Danzl, L. Reichsöllner, V. Melezhik, P. Schmelcher, and H.-C. Nägerl, *Confinement-Induced Resonances in Low-Dimensional Quantum Systems*, Phys. Rev. Lett. **104** (2010).

[Han09] T. M. Hanna, E. Tiesinga, and P. S. Julienne, *Prediction of Feshbach resonances from three input parameters*, Phys. Rev. A **79**, 040701 (2009).

[Hau08] R. Haussmann and W. Zwerger, *Thermodynamics of a trapped unitary Fermi gas*, Phys. Rev. A **78**, 063602 (2008).

[Hes67] G. B. Hess and W. M. Fairbank, *Measurements of Angular Momentum in Superfluid Helium*, Phys. Rev. Lett. **19**, 216 (1967).

[Ho11] T.-L. Ho and X. Cui, *Alternative Route to Strong Interaction: Narrow Feshbach Resonance*, arXiv:1105.4627v2 (2011).

[Hod02] E. Hodby, G. Hechenblaikner, S. A. Hopkins, O. M. Maragò, and C. J. Foot, *Vortex Nucleation in Bose-Einstein Condensates in an Oblate, Purely Magnetic Potential*, Phys. Rev. Lett. **88**, 010405 (2002).

[Hof07] S. Hofferberth, I. Lesanovsky, B. Fischer, T. Schumm, and J. Schmiedmayer, *Non-equilibrium coherence dynamics in one-dimensional Bose gases*, Nature **449**, 324 (2007).

[Hor10] M. Horikoshi, S. Nakajima, M. Ueda, and T. Mukaiyama, *Measurement of universal thermodynamic functions for a unitary Fermi gas*, Science **327**, 442 (2010).

[Hua87] K. Huang (Ed.), *Statistical Mechanics*, John Wiley & Sons, New York (1987), page 104.

[Hut07] J. M. Hutson, *Feshbach resonances in the presence of inelastic scattering: threshold behavior and suppression of poles in scattering lengths*, New J. Phys. **9**, 152 (2007).

[Ina08] Y. Inada, M. Horikoshi, S. Nakajima, M. Kuwata-Gonokami, M. Ueda, and T. Mukaiyama, *Critical Temperature and Condensate Fraction of a Fermion Pair Condensate*, Phys. Rev. Lett. **101**, 180406 (2008).

[Ing08a] M. Inguscio, W. Ketterle, and C. Salomon (Eds.), *Ultra-cold Fermi Gases*, IOS Press, Amsterdam (2008), Proceedings of the International School of Physics "Enrico Fermi", Course CLXIV, Varenna, 20-30 June 2006.

[Ing08b] M. Inguscio, W. Ketterle, and C. Salomon (Eds.), *Ultracold Fermi gases, Proceedings of the international school of physics "Enrico Fermi", Course CLXIV, Varenna, June 2006*, IOS Press, Amsterdam (2008).

[Ino98] S. Inouye, M. R. Andrews, J. Stenger, H.-J. Miesner, D. M. Stamper-Kurn, and W. Ketterle, *Observation of Feshbach resonances in a Bose-Einstein condensate*, Nature **392**, 151 (1998).

[Ino01] S. Inouye, S. Gupta, T. Rosenband, A. P. Chikkatur, A. Görlitz, T. L. Gustavson, A. E. Leanhardt, D. E. Pritchard, and W. Ketterle, *Observation of Vortex Phase Singularities in Bose-Einstein Condensates*, Phys. Rev. Lett. **87**, 080402 (2001).

[Isk06] M. Iskin and C. A. R. Sá de Melo, *Two-Species Fermion Mixtures with Population Imbalance*, Phys. Rev. Lett. **97**, 100404 (2006).

[Isk07] M. Iskin and C. A. R. Sá de Melo, *Superfluid and Insulating Phases of Fermion Mixtures in Optical Lattices*, Phys. Rev. Lett. **99**, 080403 (2007).

[Isk08] M. Iskin and C. J. Williams, *Trap-imbalanced fermion mixtures*, Phys. Rev. A **77**, 013605 (2008).

[Jac10] B. Jacak and P. Steinberg, *Creating the perfect liquid in heavy-ion collisions*, Phys. Today **63**, no. 5, 39 (2010).

[Jo09] G.-B. Jo, Y.-R. Lee, J.-H. Choi, C. A. Christensen, T. H. Kim, J. H. Thywissen, D. E. Pritchard, and W. Ketterle, *Itinerant Ferromagnetism in a Fermi Gas of Ultracold Atoms*, Science **325**, 1521 (2009).

[Joc03a] S. Jochim, M. Bartenstein, A. Altmeyer, G. Hendl, C. Chin, J. Hecker Denschlag, and R. Grimm, *Pure Gas of Optically Trapped Molecules Created from Fermionic Atoms*, Phys. Rev. Lett **91**, 240402 (2003).

[Joc03b] S. Jochim, M. Bartenstein, A. Altmeyer, G. Hendl, S. Riedl, C. Chin, J. Hecker Denschlag, and R. Grimm, *Bose-Einstein Condensation of Molecules*, Science **302**, 2101 (2003).

[Joc04] S. Jochim, *Bose-Einstein Condensation of Molecules*, Ph.D. thesis, Innsbruck University (2004).

[Jos11] J. A. Joseph, J. E. Thomas, M. Kulkarni, and A. G. Abanov, *Observation of Shock Waves in a Strongly Interacting Fermi Gas*, Phys. Rev. Lett. **106**, 150401 (2011).

[Kas92] M. Kasevich and S. Chu, *Laser-cooling below a photon recoil with three-level atoms*, Phys. Rev. Lett. **69**, 1741 (1992).

[Ket96] W. Ketterle, S. Durfee, M. Stamper, and E. Fermi, *Making, probing and understanding Bose-Einstein condensates*, arXiv:cond-mat/9904034 (1996).

[Ket08] W. Ketterle and M. W. Zwierlein, *Making, probing and understanding ultracold Fermi gases*, in Inguscio *et al.* [Ing08b], 95–287.

[Kim04] E. Kim and M. H. W. Chan, *Observation of superflow in solid helium*, Science **305**, 1941 (2004).

[Kin04a] J. Kinast, S. L. Hemmer, M. E. Gehm, A. Turlapov, and J. E. Thomas, *Evidence for Superfluidity in a Resonantly Interacting Fermi Gas*, Phys. Rev. Lett. **92**, 150402 (2004).

[Kin04b] J. Kinast, A. Turlapov, and J. E. Thomas, *Breakdown of Hydrodynamics in the Radial Breathing Mode of a Strongly Interacting Fermi Gas*, Phys. Rev. A **70**, 051401(R) (2004).

[Kin05a] J. Kinast, A. Turlapov, and J. E. Thomas, *Damping of a Unitary Fermi Gas*, Phys. Rev. Lett. **94**, 170404 (2005).

[Kin05b] J. Kinast, A. Turlapov, J. E. Thomas, Q. Chen, J. Stajic, and K. Levin, *Heat Capacity of a Strongly Interacting Fermi Gas*, Science **307**, 1296 (2005).

[Köh05] T. Köhler, E. Tiesinga, and P. S. Julienne, *Spontaneous Dissociation of Long-Range Feshbach Molecules*, Phys. Rev. Lett. **94**, 020402 (2005).

[Koh07] C. Kohstall, *A New Toolbox for Experiments with Ultracold Li6*, Diploma thesis, Innsbruck University (2007).

[Koh11] C. Kohstall, M. Zaccanti, M. Jag, A. Trenkwalder, P. Massignan, G. M. Bruun, F. Schreck, and R. Grimm, *Metastability and Coherence of Repulsive Polarons in a Strongly Interacting Fermi Mixture* (2011), arXiv:1112.0020v1.

[Lam10] G. Lamporesi, J. Catani, G. Barontini, Y. Nishida, M. Inguscio, and F. Minardi, *Scattering in Mixed Dimensions with Ultracold Gases*, Phys. Rev. Lett. **104**, 5 (2010).

[Lan57] L. D. Landau, *The theory of a Fermi liquid*, Sov. Phys. JETP **3**, 920 (1957).

[Lan80] L. Landau, E. Lifshitz, and L. Pitaevskii, *Statistical physics Part 2*, Statistical Physics, Butterworth-Heinemann (1980).

[Lan08] F. Lang, K. Winkler, C. Strauss, R. Grimm, and J. Hecker Denschlag, *Ultracold Triplet Molecules in the Rovibrational Ground State*, Phys. Rev. Lett. **101**, 133005 (2008).

[Lea02] A. E. Leanhardt, A. Görlitz, A. P. Chikkatur, D. Kielpinski, Y. Shin, D. E. Pritchard, and W. Ketterle, *Imprinting Vortices in a Bose-Einstein Condensate using Topological Phases*, Phys. Rev. Lett. **89**, 190403 (2002).

[LeB09] L. J. LeBlanc, J. H. Thywissen, A. A. Burkov, and A. Paramekanti, *Repulsive Fermi gas in a harmonic trap: Ferromagnetism and spin textures*, Phys. Rev. A **80**, 013607 (2009).

[Ler11] A. Lercher, T. Takekoshi, M. Debatin, B. Schuster, R. Rameshan, F. Ferlaino, R. Grimm, and H.-C. Nägerl, *Production of a dual-species Bose-Einstein condensate of Rb and Cs atoms*, Eur. Phys. J. D **65**, 3 (2011).

[Lev09] J. Levinsen, T. G. Tiecke, J. T. M. Walraven, and D. S. Petrov, *Atom-dimer scattering and long-lived trimers in fermionic mixtures*, Phys. Rev. Lett. **103**, 153202 (2009).

[Lev11] J. Levinsen and D. S. Petrov, *Atom-dimer and dimer-dimer scattering in fermionic mixtures near a narrow Feshbach resonance*, Eur. Phys. J. D **65**, 67 (2011).

[Liu03] W. V. Liu and F. Wilczek, *Interior Gap Superfluidity*, Phys. Rev. Lett. **90**, 047002 (2003).

[Lob06] C. Lobo, A. Recati, S. Giorgini, and S. Stringari, *Normal state of a polarized Fermi gas at unitarity*, Phys. Rev. Lett. **97**, 200403 (2006).

[Luo07] L. Luo, B. Clancy, J. Joseph, J. Kinast, and J. E. Thomas, *Measurement of the Entropy and Critical Temperature of a Strongly Interacting Fermi Gas*, Phys. Rev. Lett. **98**, 080402 (2007).

[Luo09] L. Luo and J. E. Thomas, *Thermodynamic Measurements in a Strongly Interacting Fermi Gas*, J. Low Temp. Phys. **154**, 1 (2009).

[Mad00a] P. Maddaloni, M. Modugno, C. Fort, F. Minardi, and M. Inguscio, *Collective oscillations of two colliding Bose-Einstein condensates*, Phys. Rev. Lett. **85**, 2413 (2000).

[Mad00b] K. W. Madison, F. Chevy, W. Wohlleben, and J. Dalibard, *Vortex Formation in a Stirred Bose-Einstein Condensate*, Phys. Rev. Lett. **84**, 806 (2000).

[Mad01] K. W. Madison, F. Chevy, V. Bretin, and J. Dalibard, *Stationary States of a Rotating Bose-Einstein Condensate: Routes to Vortex Nucleation*, Phys. Rev. Lett. **86**, 4443 (2001).

[Mas] P. Massignan, in preparation.

[Mas08a] P. Massignan, G. M. Bruun, and H. T. C. Stoof, *Twin peaks in rf spectra of Fermi gases at unitarity*, Phys. Rev. A **77**, 031601 (2008).

[Mas08b] P. Massignan and H. T. C. Stoof, *Efimov states near a Feshbach resonance*, Phys. Rev. A **78**, 030701 (2008).

[Mas11] P. Massignan and G. M. Bruun, *Repulsive polarons and itinerant ferromagnetism in strongly polarized Fermi gases*, Eur. Phys. J D **65**, 83 (2011).

[Mat92] R. Mattuck, *A guide to Feynman diagrams in the many-body problem*, Dover books on physics and chemistry, Dover Publications (1992).

[Men02] C. Menotti, P. Pedri, and S. Stringari, *Expansion of an Interacting Fermi Gas*, Phys. Rev. Lett. **89**, 250402 (2002).

[Mie96] F. H. Mies, C. J. Williams, P. S. Julienne, and M. Krauss, *Estimating bounds on collisional relaxation rates of spin-polarized Rb-87 atoms at ultracold temperatures*, J. Res. Natl. Inst. Stand. Technol. **101**, 521 (1996).

[Mil05] D. E. Miller, J. R. Anglin, J. R. Abo-Shaeer, K. Xu, J. K. Chin, and W. Ketterle, *High-contrast interference in a thermal cloud of atoms*, Phys. Rev. A **71**, 043615 (2005).

[Mor05] H. Moritz, T. Stöferle, K. Günter, M. Köhl, and T. Esslinger, *Confinement Induced Molecules in a 1D Fermi Gas*, Phys. Rev. Lett. **94**, 210401 (2005).

[Mor09] C. Mora and F. Chevy, *Ground state of a tightly bound composite dimer immersed in a Fermi sea*, Phys. Rev. A **80**, 033607 (2009).

[Mot65] N. F. Mott and H. Massey, *The Theory of Atomic Collisions*, Oxford (1965).

[Nai11] D. Naik, A. Trenkwalder, C. Kohstall, F. M. Spiegelhalder, M. Zaccanti, G. Hendl, F. Schreck, R. Grimm, T. Hanna, and P. Julienne, *Feshbach resonances in the ^{6}Li-^{40}K Fermi-Fermi mixture: Elastic versus inelastic interactions*, Eur. Phys. J. D **65**, 55 (2011).

[Nak11] S. Nakajima, M. Horikoshi, T. Mukaiyama, P. Naidon, and M. Ueda, *Measurement of an Efimov Trimer Binding Energy in a Three-Component Mixture of* ^{6}Li, Phys. Rev. Lett. **106**, 143201 (2011).

[Nas09a] S. Nascimbène, N. Navon, K. J. Jiang, L. Tarruell, M. Teichmann, J. McKeever, F. Chevy, and C. Salomon, *Collective Oscillations of an Imbalanced Fermi Gas: Axial Compression Modes and Polaron Effective Mass*, Phys. Rev. Lett. **103**, 170402 (2009).

[Nas09b] S. Nascimbène, N. Navon, K. J. Jiang, L. Tarruell, M. Teichmann, J. McKeever, F. Chevy, and C. Salomon, *Collective oscillations of an imbalanced Fermi gas: Axial compression modes and polaron effective mass*, Phys. Rev. Lett. **103**, 170402 (2009).

[Nas10] S. Nascimbène, N. Navon, K. J. Jiang, F. Chevy, and C. Salomon, *Exploring the thermodynamics of a universal Fermi gas*, Nature **463**, 1057 (2010).

[Nas11] S. Nascimbène, N. Navon, S. Pilati, F. Chevy, S. Giorgini, A. Georges, and C. Salomon, *Fermi-liquid behavior of the normal phase of a strongly interacting gas of cold atoms*, Phys. Rev. Lett. **106**, 215303 (2011).

[Nav10] N. Navon, S. Nascimbène, F. Chevy, and C. Salomon, *The Equation of State of a Low-Temperature Fermi Gas with Tunable Interactions*, Science **328**, 729 (2010).

[Ni08] K.-K. Ni, S. Ospelkaus, M. H. G. de Miranda, A. Pe'er, B. Neyenhuis, J. J. Zirbel, S. Kotochigova, P. S. Julienne, D. S. Jin, and J. Ye, *A High Phase-Space-Density Gas of Polar Molecules*, Science **322**, 231 (2008).

[Nis08] Y. Nishida and S. Tan, *Universal Fermi gases in mixed dimensions*, Phys. Rev. Lett. **101**, 170401 (2008).

[Nis09a] Y. Nishida, *Induced p-wave superfluidity in two dimensions: Brane world in cold atoms and nonrelativistic defect CFTs*, Ann. Phys. **324**, 897 (2009).

[Nis09b] Y. Nishida and S. Tan, *Confinement-induced Efimov resonances in Fermi-Fermi mixtures*, Phys. Rev. A **79**, 060701(R) (2009).

[Nis10] Y. Nishida, *Phases of a bilayer Fermi gas*, Phys. Rev. A **82**, 011605 (2010).

[O'H02] K. M. O'Hara, S. L. Hemmer, M. E. Gehm, S. R. Granade, and J. E. Thomas, *Observation of a Strongly Interacting Degenerate Fermi Gas*, Science **298**, 2179 (2002).

[Ols98] M. Olshanii, *Atomic scattering in the presence of an external confinement and a gas of impenetrable bosons*, Phys. Rev. Lett. **81**, 938 (1998).

[Ono04] R. Onofrio and C. Presilla, *Ultracold Atomic FermiBose Mixtures in Bichromatic Optical Dipole Traps: A Novel Route to Study Fermion Superfluidity*, J. Stat. Phys. **115**, 57 (2004).

[Ors08] G. Orso, L. P. Pitaevskii, and S. Stringari, *Equilibrium and dynamics of a trapped superfluid Fermi gas with unequal masses*, Phys. Rev. A **77**, 033611 (2008).

[Ott08] T. B. Ottenstein, T. Lompe, M. Kohnen, A. N. Wenz, and S. Jochim, *Collisional stability of a three-component degenerate Fermi gas*, Phys. Rev. Lett. **101**, 203202 (2008).

[Paa06] T. Paananen, J.-P. Martikainen, and P. Törmä, *Pairing in a three-component Fermi gas*, Phys. Rev. A **73**, 053606 (2006).

[Par06] G. B. Partridge, W. Li, R. I. Kamar, Y. Liao, and R. G. Hulet, *Pairing and Phase Separation in a Polarized Fermi Gas*, Science **311**, 503 (2006).

[Pek11a] D. Pekker, M. Babadi, R. Sensarma, N. Zinner, L. Pollet, M. W. Zwierlein, and E. Demler, *Competition between Pairing and Ferromagnetic Instabilities in Ultracold Fermi Gases near Feshbach Resonances*, Phys. Rev. Lett. **106**, 050402 (2011).

[Pek11b] D. Pekker and E. Demler, *Competing instabilities in quench experiments with ultracold Fermi gases near a Feshbach resonance*, arXiv:1107.3930v1 (2011).

[Per04] A. Perali, P. Pieri, L. Pisani, and G. C. Strinati, *BCS-BEC Crossover at Finite Temperature for Superfluid Trapped Fermi Atoms*, Phys. Rev. Lett. **92**, 220404 (2004).

[Pet02] C. J. Pethick and H. Smith, *Bose-Einstein condensation in dilute gases*, Cambridge University Press (2002).

[Pet03] D. S. Petrov, *Three-body problem in Fermi gases with short-range interparticle interaction*, Phys. Rev. A **67**, 010703 (2003).

[Pet04a] D. S. Petrov, *Three-boson problem near a narrow Feshbach resonance*, Phys. Rev. Lett. **93**, 143201 (2004).

[Pet04b] D. S. Petrov, C. Salomon, and G. V. Shlyapnikov, *Weakly Bound Dimers of Fermionic Atoms*, Phys. Rev. Lett. **93**, 090404 (2004).

[Pet05a] D. S. Petrov, C. Salomon, and G. V. Shlyapnikov, *Diatomic molecules in ultracold Fermi gases-novel composite bosons*, J. Phys. B: At. Mol. Opt. Phys. **38**, S645 (2005).

[Pet05b] D. S. Petrov, C. Salomon, and G. V. Shlyapnikov, *Scattering properties of weakly bound dimers of fermionic atoms*, Phys. Rev. A **71**, 012708 (2005).

[Pet07] D. S. Petrov, G. E. Astrakharchik, D. J. Papoular, C. Salomon, and G. V. Shlyapnikov, *Crystalline Phase of Strongly Interacting Fermi Mixtures*, Phys. Rev. Lett. **99**, 130407 (2007).

[Pil10] S. Pilati, G. Bertaina, S. Giorgini, and M. Troyer, *Itinerant ferromagnetism of a repulsive atomic Fermi gas: A quantum Monte Carlo study*, Phys. Rev. Lett. **105**, 030405 (2010).

[Pri04] L. Pricoupenko and Y. Castin, *One particle in a box: The simplest model for a Fermi gas in the unitary limit*, Phys. Rev. A **69**, 051601 (2004).

[Pro08] N. Prokof'ev and B. Svistunov, *Fermi-polaron problem: Diagrammatic Monte Carlo method for divergent sign-alternating series*, Phys. Rev. B **77**, 020408 (2008).

[Pun09] M. Punk, P. T. Dumitrescu, and W. Zwerger, *Polaron-to-molecule transition in a strongly imbalanced Fermi gas*, Phys. Rev. A **80**, 053605 (2009).

[Rad10] L. Radzihovsky and D. E. Sheehy, *Imbalanced Feshbach-resonant Fermi gases*, Rep. Prog. Phys. **73**, 076501 (2010).

[Reg04] C. A. Regal, M. Greiner, and D. S. Jin, *Observation of Resonance Condensation of Fermionic Atom Pairs*, Phys. Rev. Lett. **92**, 040403 (2004).

[Rid11] A. Ridinger, S. Chaudhuri, T. Salez, U. Eismann, D. R. Fernandes, K. Magalhães, D. Wilkowski, C. Salomon, and F. Chevy, *Large atom number dual-species magneto-optical trap for fermionic* ^6Li *and* ^{40}K *atoms*, Eur. Phys. J. D (2011).

[Rie08] S. Riedl, E. R. Sánchez Guajardo, C. Kohstall, A. Altmeyer, M. J. Wright, J. Hecker Denschlag, R. Grimm, G. M. Bruun, and H. Smith, *Collective oscillations of a Fermi gas in the unitarity limit: Temperature effects and the role of pair correlations*, Phys. Rev. A **78**, 053609 (2008).

[Rie09] S. Riedl, E. R. Sánchez Guajardo, C. Kohstall, J. Hecker Denschlag, and R. Grimm, *Lifetime of angular momentum in a rotating strongly interacting Fermi gas*, Phys. Rev. A **79**, 053628 (2009).

[Rie11] S. Riedl, E. R. S. Guajardo, C. Kohstall, J. Hecker Denschlag, and R. Grimm, *Superfluid quenching of the moment of inertia in a strongly interacting Fermi gas*, New J. Phys. **13**, 035003 (2011).

[Rin80] P. Ring and P. Schuck, *The Nuclear Many Body Problem*, Springer, Berlin (1980).

[Roa08] G. Roati, C. D'Errico, L. Fallani, M. Fattori, C. Fort, M. Zaccanti, G. Modugno, M. Modugno, and M. Inguscio, *Anderson localization of a non-interacting Bose-Einstein condensate.*, Nature **453**, 895 (2008).

[Rob98] J. L. Roberts, N. R. Claussen, J. J. P. Burke, C. H. Greene, E. A. Cornell, and C. E. Wieman, *Resonant magnetic field control of elastic scattering in cold* ^{85}Rb, Phys. Rev. Lett. **81**, 5109 (1998).

[Sad11] K. Sadeghzadeh, G. M. Bruun, C. Lobo, P. Massignan, and A. Recati, *Metastability in spin-polarized Fermi gases and quasiparticle decays*, New J. Phys. **13**, 055011 (2011).

[San11] C. Sanner, E. J. Su, W. Huang, A. Keshet, J. Gillen, and W. Ketterle, *Correlations and Pair Formation in a Repulsively Interacting Fermi Gas* (2011), arxiv:1108.2017.

[Sav97] T. A. Savard, K. M. O'Hara, and J. E. Thomas, *Laser-noise-induced heating in far-off resonance optical traps*, Phys. Rev. A **56**, R1095 (1997).

[Sch94] W. Schöllkopf and J. P. Toennies, *Nondestructive Mass Selection of Small van der Waals Clusters*, Science **266**, 1345 (1994).

[Sch07] C. H. Schunck, M. W. Zwierlein, A. Schirotzek, and W. Ketterle, *Superfluid Expansion of a Rotating Fermi Gas*, Phys. Rev. Lett. **98**, 050404 (2007).

[Sch08] A. Schirotzek, Y. Shin, C. H. Schunck, and W. Ketterle, *Determination of the Superfluid Gap in Atomic Fermi Gases by Quasiparticle Spectroscopy*, Phys. Rev. Lett. **101**, 140403 (2008).

[Sch09a] T. Schäfer and D. Teaney, *Nearly perfect fluidity: from cold atomic gases to hot quark gluon plasmas*, Rep. Prog. Phys. **72**, 126001 (2009).

[Sch09b] A. Schirotzek, C.-H. Wu, A. Sommer, and M. W. Zwierlein, *Observation of Fermi polarons in a tunable Fermi liquid of ultracold atoms*, Phys. Rev. Lett. **102**, 230402 (2009).

[Sch11] R. Schmidt and T. Enss, *Excitation spectra and rf response near the polaron-to-molecule transition from the functional renormalization group*, Phys. Rev. A **83**, 063620 (2011).

[Shi04] Y. Shin, M. Saba, T. A. Pasquini, W. Ketterle, D. E. Pritchard, and A. E. Leanhardt, *Atom Interferometry with Bose-Einstein Condensates in a Double-Well Potential*, Phys. Rev. Lett. **92**, 050405 (2004).

[Shi07] Y. Shin, C. H. Schunck, A. Schirotzek, and W. Ketterle, *Tomographic rf spectroscopy of a trapped Fermi gas at unitarity*, Phys. Rev. Lett. **99**, 090403 (2007).

[Sim00] J. E. Simsarian, J. Denschlag, M. Edwards, C. W. Clark, L. Deng, E. W. Hagley, K. Helmerson, S. L. Rolston, and W. D. Phillips, *Imaging the Phase of an Evolving Bose-Einstein Condensate Wave Function*, Phys. Rev. Lett. **85**, 2040 (2000).

[Sin97] S. Sinha, *Semiclassical analysis of collective excitations in Bose-Einstein condensate*, Phys. Rev. A **55**, 4325 (1997).

[Spi09] F. M. Spiegelhalder, A. Trenkwalder, D. Naik, G. Hendl, F. Schreck, and R. Grimm, *Collisional stability of ^{40}K immersed in a strongly interacting Fermi Gas of ^{6}Li*, Phys. Rev. Lett. **103**, 223203 (2009).

[Spi10a] F. M. Spiegelhalder, A. Trenkwalder, D. Naik, G. Kerner, E. Wille, G. Hendl, F. Schreck, and R. Grimm, *All-optical production of a degenerate mixture of ^{6}Li and ^{40}K and creation of heteronuclear molecules*, Phys. Rev. A **81**, 043637 (2010).

[Spi10b] F. M. Spiegelhalder, A. Trenkwalder, D. Naik, G. Kerner, E. Wille, G. Hendl, F. Schreck, and R. Grimm, *All-optical production of a degenerate mixture of ^{6}Li and ^{40}K and creation of heteronuclear molecules*, Phys. Rev. A **81**, 043637 (2010), because of a calibration error the magnetic field values in the vicinity of the 168 G resonance in the *aa* channel need to be corrected by -47 mG.

[Sta05] J. Stajic, Q. Chen, and K. Levin, *Density Profiles of Strongly Interacting Trapped Fermi Gases*, Phys. Rev. Lett. **94**, 060401 (2005).

[Ste08] J. T. Stewart, J. P. Gaebler, and D. S. Jin, *Using photoemission spectroscopy to probe a strongly interacting Fermi gas*, Nature **454**, 744 (2008).

[Str96] S. Stringari, *Moment of Inertia and Superfluidity of a Trapped Bose Gas*, Phys. Rev. Lett. **76**, 1405 (1996).

[Svi98] A. A. Svidzinsky and A. L. Fetter, *Normal modes of a vortex in a trapped Bose-Einstein condensate*, Phys. Rev. A **58**, 3168 (1998).

[Tag08] M. Taglieber, A.-C. Voigt, T. Aoki, T. W. Hänsch, and K. Dieckmann, *Quantum Degenerate Two-Species Fermi-Fermi Mixture Coexisting with a Bose-Einstein Condensate*, Phys. Rev. Lett. **100**, 010401 (2008).

[Tho05] S. T. Thompson, E. Hodby, and C. E. Wieman, *Spontaneous dissociation of ^{85}Rb Feshbach molecules*, Phys. Rev. Lett. **94**, 020401 (2005).

[Tho10] J. E. Thomas, *The nearly perfect Fermi gas*, Phys. Today **63**, no. 5, 34 (2010).

[Tie09] E. Tiemann, H. Knöckel, P. Kowalczyk, W. Jastrzebski, A. Pashov, H. Salami, and A. J. Ross, *Coupled system aΣ3+ and XΣ1+ of KLi: Feshbach resonances and corrections to the Born-Oppenheimer approximation*, Phys. Rev. A **79**, 042716 (2009).

[Tie10] T. G. Tiecke, M. R. Goosen, A. Ludewig, S. D. Gensemer, S. Kraft, S. J. J. M. F. Kokkelmans, and J. T. M. Walraven, *Broad Feshbach resonance in the ^6Li-^{40}K mixture*, Phys. Rev. Lett. **104**, 053202 (2010).

[Tre11a] A. Trenkwalder, *Creation of a Strongly Interacting Fermi-Fermi Mixture of ^6Li and ^{40}K*, Ph.D. thesis, Innsbruck University (2011).

[Tre11b] A. Trenkwalder, C. Kohstall, M. Zaccanti, D. Naik, A. I. Sidorov, F. Schreck, and R. Grimm, *Hydrodynamic expansion of a strongly tnteracting Fermi-Fermi mixture*, Phys. Rev. Lett. **106**, 115304 (2011).

[Urb03] M. Urban and P. Schuck, *Slow rotation of a superfluid trapped Fermi gas*, Phys. Rev. A **67**, 033611 (2003).

[Urb05] M. Urban, *Two-fluid model for a rotating trapped Fermi gas in the BCS phase*, Phys. Rev. A **71**, 033611 (2005).

[Vee08] G. Veeravalli, E. Kuhnle, P. Dyke, and C. J. Vale, *Bragg Spectroscopy of a Strongly Interacting Fermi Gas*, Phys. Rev. Lett. **101**, 250403 (2008).

[Vic00] L. Vichi, *Collisional Damping of the Collective Oscillations of a Trapped Fermi Gas*, J. Low. Temp. Phys. **121**, 177 (2000).

[Voi09] A.-C. Voigt, M. Taglieber, L. Costa, T. Aoki, W. Wieser, T. W. Hänsch, and K. Dieckmann, *Ultracold heteronuclear Fermi-Fermi molecules*, Phys. Rev. Lett. **102**, 020405 (2009), *ibid.* **105**, 269904(E) (2010).

[Wan09] B. Wang, H.-D. Chen, and S. Das Sarma, *Quantum phase diagram of fermionic mixtures with population imbalance in one-dimensional optical lattices*, Phys. Rev. A **79**, 051604(R) (2009).

[Wei99] J. Weiner, V. S. Bagnato, S. Zilio, and P. S. Julienne, *Experiments and theory in cold and ultracold collisions*, Rev. Mod. Phys. **71**, 1 (1999).

[Wil02] J. E. Williams, E. Zaremba, B. Jackson, T. Nikuni, and A. Griffin, *Dynamical Instability of a Condensate Induced by a Rotating Thermal Gas*, Phys. Rev. Lett. **88**, 070401 (2002).

[Wil08] E. Wille, F. M. Spiegelhalder, G. Kerner, D. Naik, A. Trenkwalder, G. Hendl, F. Schreck, R. Grimm, T. G. Tiecke, J. T. M. Walraven, S. J. J. M. F. Kokkelmans, E. Tiesinga, and P. S. Julienne, *Exploring an ultracold Fermi-Fermi mixture: Interspecies Feshbach resonances and scattering properties of* ^{6}*Li and* ^{40}*K*, Phys. Rev. Lett. **100**, 053201 (2008).

[Wil09] E. Wille, *Preparation of an Optically Trapped Fermi-Fermi Mixture of* ^{6}*Li and* ^{40}*K Atoms and Characterization of the Interspecies Interactions by Feshbach Spectroscopy*, Ph.D. thesis, Innsbruck University (2009).

[Wri07] M. J. Wright, S. Riedl, A. Altmeyer, C. Kohstall, E. R. Sánchez Guajardo, J. Hecker Denschlag, and R. Grimm, *Finite-temperature collective dynamics of a Fermi gas in the BEC-BCS crossover*, Phys. Rev. Lett. **99**, 150403 (2007).

[Wu11] C.-H. Wu, I. Santiago, J. W. Park, P. Ahmadi, and M. W. Zwierlein, *Strongly Interacting Isotopic Bose-Fermi Mixture Immersed in a Fermi Sea*, arXiv:1103.4630v1 [cond-mat.quant-gas] (2011).

[Xio06] H. Xiong, S. Liu, and M. Zhan, *Interaction-induced interference for two independent BoseEinstein condensates*, New J. Phys. **8**, 245 (2006).

[Yag05] K. Yagi, T. Hatsuda, and Y. Miake, *Quark-Gluon Plasma: From Big Bang to Little Bang*, Cambridge University Press (2005).

[Zam98] F. Zambelli and S. Stringari, *Quantized Vortices and Collective Oscillations of a Trapped Bose-Einstein Condensate*, Phys. Rev. Lett. **81**, 1754 (1998).

[Zaw10] M. E. Zawadzki, P. F. Griffin, E. Riis, and A. S. Arnold, *Spatial interference from well-separated split condensates*, Phys. Rev. A **81**, 043608 (2010).

[Zha07] W. Zhang and C. A. R. Sá de Melo, *Matter-wave interference in s -wave and p -wave Fermi condensates*, Phys. Rev. A **76**, 013627 (2007).

[Zhu01] O. N. Zhuravlev, A. E. Muryshev, and P. O. Fedichev, *Dissipative dynamics of vortex arrays in anisotropic traps*, Phys. Rev. A **64**, 053601 (2001).

[Zwe09] W. Zwerger, *Itinerant Ferromagnetism with Ultracold Atoms*, Scince **325**, 1507 (2009).

[Zwi03a] M. W. Zwierlein, C. A. Stan, C. H. Schunck, S. M. F. Raupach, S. Gupta, Z. Hadzibabic, and W. Ketterle, *Observation of Bose-Einstein Condensation of Molecules*, Phys. Rev. Lett. **91**, 250401 (2003).

[Zwi03b] M. W. Zwierlein, C. A. Stan, C. H. Schunck, S. M. F. Raupach, S. Gupta, Z. Hadzibabic, and W. Ketterle, *Observation of Bose-Einstein Condensation of Molecules*, Phys. Rev. Lett. **91**, 250401 (2003).

[Zwi04] M. W. Zwierlein, C. A. Stan, C. H. Schunck, S. M. F. Raupach, A. J. Kerman, and W. Ketterle, *Condensation of Pairs of Fermionic Atoms near a Feshbach Resonance*, Phys. Rev. Lett. **92**, 120403 (2004).

[Zwi05a] M. W. Zwierlein, J. R. Abo-Shaeer, A. Schirotzek, C. H. Schunck, and W. Ketterle, *Vortices and superfluidity in a strongly interacting Fermi gas*, Nature **435**, 1047 (2005).

[Zwi05b] M. W. Zwierlein, J. R. Abo-Shaeer, A. Schirotzek, C. H. Schunck, and W. Ketterle, *Vortices and Superfluidity in a Strongly Interacting Fermi Gas*, Nature **435**, 1047 (2005).

[Zwi06a] M. W. Zwierlein, A. Schirotzek, C. H. Schunck, and W. Ketterle, *Direct observation of the superfluid phase transition in ultracold Fermi gases*, Nature **442**, 54 (2006).

[Zwi06b] M. W. Zwierlein, A. Schirotzek, C. H. Schunck, and W. Ketterle, *Fermionic Superfluidity with Imbalanced Spin Populations*, Science **311**, 492 (2006).